CHALMERS
UNIVERSITY OF TECHNOLOGY

Investigation of Heavy Vehicle Dynamics Behaviour Under the Wind and Bridge Motion Excitations

Master's thesis in Automotive Engineering

Ajit Kumar MADHAVA PRAKASH
Pramod SIVARAMAKRISHNAN

Department of Automotive Engineering
CHALMERS UNIVERSITY OF TECHNOLOGY
Gothenburg, Sweden 2021

Master's thesis in Automotive engineering

Investigation of Heavy Vehicle Dynamics Behaviour Under the Wind and Bridge Motion Excitations

Ajit Kumar MADHAVA PRAKASH
Pramod SIVARAMAKRISHNAN

CHALMERS
UNIVERSITY OF TECHNOLOGY

Department of Mechanics and Maritime Sciences
Division of Vehicle Engineering and Autonomous Systems
Chalmers University of Technology
Gothenburg, Sweden 2021

Investigation of Heavy Vehicle Dynamics Behaviour Under the Wind and Bridge Motion Excitations.
Master's thesis in Automotive Engineering

Supervisor: Dragan Sekulic, Vehicle Engineering and Autonomous Systems
Supervisor: Alexey Vdovin, Vehicle Engineering and Autonomous Systems
Supervisor: Stian Moe Johannesen, Norwegian Public Roads Administration
Examiner: Bengt J H Jacobson, Vehicle Engineering and Autonomous Systems

Master's Thesis 2021:26
Department of Automotive Engineering
Division of Vehicle Engineering and Autonomous Systems
Chalmers University of Technology
SE-412 96 Gothenburg
Telephone +46 31 772 1000

Cover: An Aerial shot of the Bjørnafjorden floating bridge on E39.
Illustration: Norwegian Public Roads Administration

Typeset in LaTeX
Printed by Chalmers Reproservice
Gothenburg, Sweden 2021

Investigation of Heavy Vehicle Dynamics Behaviour Under the Wind and Bridge Motion Excitations
Master's thesis in Automotive Engineering
AJIT KUMAR MADHAVA PRAKASH
PRAMOD SIVARAMAKRISHNAN
Department of Mechanics and Maritime Sciences
Division of Vehicle Engineering and Autonomous Systems
Chalmers University of Technology

Abstract

The floating bridge solution at Bjørnafjorden on the soon-to-be upgraded E39, pushes the envelope of engineering development. The route will be used extensively to transport commercial goods, in addition to personal commute. The vehicular traffic on this bridge will be exposed to gusty wind and oceanic currents of a 1-year storm condition. This induces stochastic motion to the bridge. This master thesis investigates the dynamic behavior of a tractor-semitrailer vehicle on the Bjørnafjorden bridge, exposed to such conditions.

The driver-vehicle-bridge system is developed on MSC.ADAMS Car/Truck, which runs on a co-simulation with MATLAB/Simulink as master. A method to simultaneously induce wind gusts and motion of the bridge is established. Bridge motion is induced as displacements, via x-Post test rig on MSC.ADAMS. Crosswinds dynamically excite the tractor-semitrailer units through computed forces and moments. ADAMS PID control, which is an advanced steering controller compared to the Snider driver model, is used to steer the vehicle to maintain the desired path.

The tractor-semitrailer is be evaluated for stability in crosswind and moving ground conditions at different test speeds. Based on vehicle dynamic responses, lane violation, risk of roll-over, driver steering effort and lateral sideslip limits are assessed for the laden and unladen vehicle on road surfaces of friction $\mu = 0.7$ and $\mu = 0.3$. Operating speed limits for the tractor semitrailer on the Bjørnafjorden floating bridge is suggested to the Norwegian Public Road Administration under the influence of 1-year storm conditions.

Keywords: E39, Bjørnafjorden floating bridge, tractor semitrailer vehicle dynamics, crosswind stability, moving ground, ADAMS Car/Truck, co-simulation, PPC, Snider

Preface

The Master's thesis titled, "Investigation of heavy vehicle dynamics behavior under the wind and bridge motion excitations", is an extension to the ongoing research at Chalmers University of Technology for the Norwegian Public Road Administration (NPRA). This thesis has been performed in partial fulfillment of the requirements for the Master's degree in Automotive engineering at Chalmers University of Technology. The research question was formulated in conjunction with the supervisors and examiners. This research was conducted between January and June 2021.

The aerodynamics part of the Master's thesis was performed by Ajit Kumar Madhava Prakash while the bridge motion and driver model sections were carried out by Pramod Sivaramakrishnan. Both team members actively engaged in technical discussion and contributed to each other's work throughout the master thesis. The outcome of the research is targeted for use by the NPRA. However, the developments in methodology and evaluation parameters are open to the scientific community in vehicle dynamics and aerodynamics field.

Acknowledgements

This thesis necessitated a tremendous amount of work and it would not have been possible without the invaluable contributions of incredibly thoughtful and supporting people. We would like to express our gratitude to the following key people:

To *Bengt*, for providing us with an opportunity to work with a novel topic. Your insightful comments at the very early stages of the thesis served as a guidance to steer us in the right direction. Given your tightly packed schedule, you never diluted our weekly meeting but ensured we benefit from every minute of your presence. As someone with exhaustive knowledge in vehicle dynamics, it amazes us how you descend yourself down to our level. We admit that it was sometimes difficult to cling on to your hopping forethought but learned of its essence when we encountered it. You allowed us the freedom to explore our own solutions. Your support in many administrative and critical situations will always be remembered by us. You have truly demonstrated a leadership that is second to none, to place the needs of your students above everything else.

To *Dragan*, who has been a constant source of inspiration. It has been a privilege to be associated with you and we want to express a Brobdingnagian proportion of thank you for acting as our mentor. Your fervour, passion and meticulousness at every stage of our thesis has left an indelible impression on us. From frustratingly silly questions to annoying you over weekends, you were always available and willing to answer any queries that we may have had. Having closely worked with you for the last six months, we can swear by your human qualities, affable nature, and your frequent concern for our welfare during stressful instances of the thesis. To *Alexey*, for your prework on the CFD simulations of the vehicle. Your timely inputs in respect to aerodynamics have guided us towards a better understanding of the topic. To *Stian*, who has provided us with constant encouragement throughout the course of this thesis.

To *Cihan Selvi* from MSC Software, your resourcefulness has helped us navigate all hurdles in respect to ADAMS. Your engagement coupled with enthusiasm only motivated us to work tirelessly. Your support is truly appreciated by us and the accomplishments from this master thesis is testament to that. Many a times, we had the chance to observe your creative approach to technical difficulties and troubleshooting techniques, a quality that we will strive to demonstrate in our future endeavours.

To *Håkan Johansson* and *Björn Pålsson*, Professors at Dynamics/Mechanics and Maritime Sciences, Chalmers University of Technology, the course on Rigid Body Dynamics certainly provided a good primer to the ADAMS ecosystem. Finally, to family and friends, for, without your direct or indirect involvement, love and encouragement, we would not have accomplished this.

Abbreviations

Abbreviation	**Description**
ABS	Anti-lock Braking System
ADAMS	Automatic Dynamic Analysis of Mechanical Systems (MSC Software)
ADAS	Advanced Driver Assist Systems
AEP	Automotive Engineering Project
AKISPL	Akima Spline
AP	Aim Point
BDF	Backward Difference Formulae
CASTER	Chalmers Automotive Simulator Technology Education Research
CFD	Computational Fluid Dynamics
CoG	Center of Gravity
CoP	Center of Pressure
DLC	Dynamic Load Coefficient
DoF	Degrees of Freedom
ECS	Earth Coordinate System
GUI	Graphical User Interface
GVW	Gross Vehicle Weight
HOV	High Occupancy Vehicle
HSA	Handwheel Steering Angle
I3	Index-3
ISO	International Organization for Standardization
LAD	Look Ahead Distance
LAT	Look Ahead Time
LCS	Local Coordinate System
LDW	Lane Departure Warning
LSL	Lateral Slip Limit
LTR	Load Transfer Ratio
MBD	Multi-Body Dynamics
MF	Magic Formula
MPC	Model Predictive Controller
NPRA	Norwegian Public Road Administration
ODE	Ordinary Differential Equations
PAC	Pacejka
PID	Proportional, Integral and Derivative
PPC	Pure Pursuit Controller
PSD	Power Spectral Density
RMS	Root Mean Square
RPM	Revolutions Per Minute
SI2	Stabilized-Index 2
VEAS	Vehicle Engineering and Autonomous Systems
WSDOT	Washington State Department of Transportation

List of Figures

List of Tables

Contents

1 INTRODUCTION

This chapter briefly presents the scope of the master thesis. It describes the background to the E39 upgradation project, the technical problems in focus to the master thesis, envisioned solution, the area of research and expected outcome of the master thesis.

1.1 Background

The Norwegian Public Road Administration (NPRA) is planning to improve the country's largest export region by connecting the western parts of the nation with an upgraded highway E39 [50]. The current route between the cities of Kristiansand (southern coast, Norway) and Trondheim (northern coast, Norway) is 1100km long, comprising of seven ferry connections and takes about 21 hours to travel. NPRA intends to upgrade the E39 into a ferry-free coastal highway by constructing fixed connections across the fjords, while reducing the distance by 50km with a considerable reduction in travel time. The estimated cost of travel (distance- and time-based costs, including toll fare), shall be lesser or on par with the current costs. The sections will consist of a number of tunnels and bridges subject to extreme environmental conditions. The floating bridge over Bjørnafjorden is one such structure. This bridge will be experience heave, sway and roll motions due to waves and wind gusts.

The ambition is to achieve efficient transportation over the Bjørnafjorden floating bridge, whilst maintaining the safety of vehicles and infrastructure. NPRA intends to set-up appropriate driving speeds for various vehicles in different storm conditions. In extreme weather conditions, the bridge usage should be restricted to certain vehicle types or closed entirely for traffic. In that aspect, it is important to investigate the driver-vehicle interactions in such weather conditions to determine the standards for safe operation.

The bridge-driver-vehicle system on the Bjørnafjorden floating bridge is currently being investigated through the project. Driving simulator tests in addition to numerical simulations have also been conducted in two parallel cases (passenger car [26] and coach [9] [17] [27]) and safety measures have been proposed in prior researches. Since the bridge will be used for commercial transportation of goods, it is important to investigate the behaviour of a multi-unit heavy vehicle (Truck-Semitrailer) on the Bjørnafjorden floating bridge in extreme weather conditions.

1.1.1 Bridge design concept

The Bjørnafjorden crossing is to the south of Bergen, Norway. The fjord has a basin of 600m depth and is separated from the open sea by islands. The areas close to the shores is made of thin sediment layers with soft deposits, while deep seabed is made of soft clay. This zone is also subjected to dense maritime traffic. Therefore the bridge should safely accommodate the crossing of marine vessels. Different bridge concepts were explored in phases 1 and 2 of the project [51].

The bridge is approximated to be 5km long and constructed of steel box bridge girders supported by columns over pontoons spaced 125m apart, according to phase 3 developments in the project (as illustrated in figure 1.1). A high cable stayed bridge (64 m above sea level) is constructed at the south end to allow marine traffic crossing. The pontoons are stabilized for longitudinal and lateral displacements with the help of mooring lines. Four pontoons, approximately 1km apart, are anchored with 8 mooring lines. The abutment at the north end consists of sliding bearings and expansion joint to facilitate longitudinal motion of the bridge. The pontoons are boat shaped and hence optimized to suit for 100-year storm conditions [52].

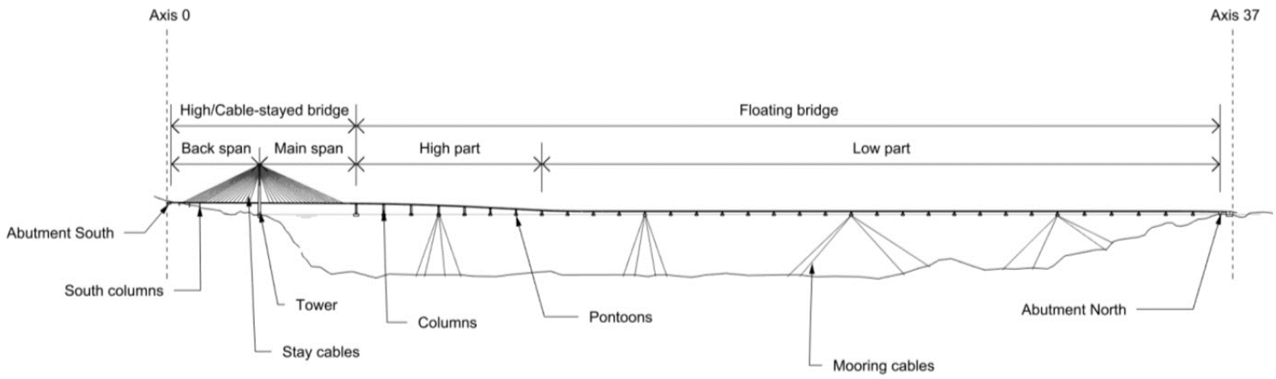

Figure 1.1: *Bjørnafjorden floating bridge*

1.1.2 E39 for vehicles

The upgraded E39 highway will experience extreme weather conditions. NPRA therefore intends to impose the following restrictions to vehicles:

- Passenger cars: speed limit varying between 80-100km/h [54]
- Heavy vehicles (17-19m in length, weighing over 3.5 tons): speed limit 80km/h [53]

NPRA estimates that the cost for operation for passenger cars (including the toll fare) on the upgraded E39 highway will be on par with the current costs. However, when the toll period expires, the cost of travel will reduce significantly. The toll fare for heavy vehicle is approximated to be twice that of passenger cars. However, the overall operation costs of heavy vehicles will be lesser than existing costs.

1.2 Problem description

Driving over a moving road is an unusual driving condition. The influence of a moving road along with aerodynamic loads on the driver-vehicle behaviour is an area that lacks good understanding and thereby the need for research. In the backdrop of limited field data available (Bjørnafjorden floating bridge currently being in its design phase), the simulation of such driving conditions and the analysis of the results would aid in better understanding of the driver-vehicle behaviour. Simulation results from high fidelity advanced vehicle models would be useful in developing and validating simpler vehicle models which could be used for investigation of similar problems.

Furthermore, the lateral dynamics of multi-unit heavy vehicles in crosswind conditions is not well known. The articulation between units has to be considered while studying the effects of aerodynamic loads. This makes the research complex.

1.3 Objectives

The primary goal of this master's thesis is to understand the effects of environmental loads from bridge motions and crosswinds on driver-vehicle behaviour. The results will thereby support NPRA to build necessary guidelines and recommend measures for the Bjørnafjorden floating bridge management. The results will also be used to validate the vehicle model previously built in MATLAB/Simulink tool.

In that view, the following research questions are attempted to be answered:

- How does driver-vehicle responses depend on vehicle speed?
- What are the safe speeds for the vehicle running over the floating bridge under the specific storm condition (1-year)?

1.4 Envisioned solution

The proposed solution in Fig. 1.2 will address the aforementioned research questions. Simulation results from the high fidelity Multi-Body Dynamics (MBD) software MSC.ADAMS will be regarded to set up recommendation/measures to support bridge management in addition to validating previously built vehicle models in MATLAB/Simulink.

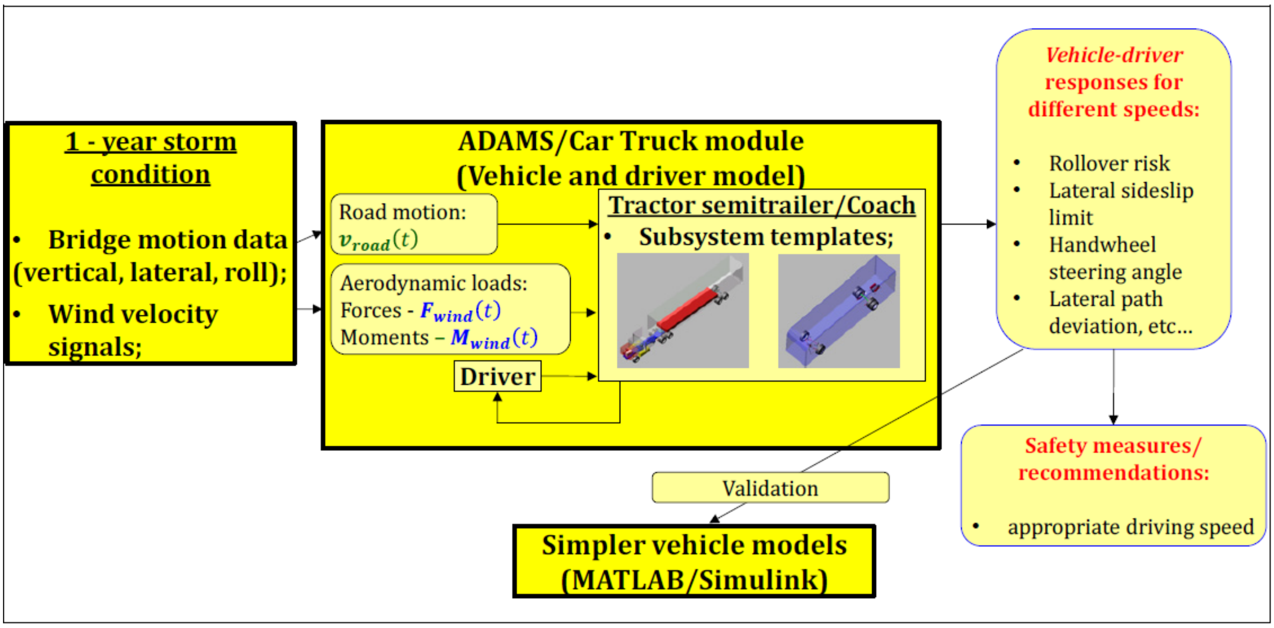

Figure 1.2: *Flowchart of investigation*

The available wind velocity signals and bridge motion data will fundamentally define the framework in defining aerodynamic loads and moving ground excitation. Furthermore, MSC.ADAMS/Car-Truck module provides the user with a slew of customization possibilities to define the vehicle model using the template builder interface. The template builder allows for the creation and/or modification of vehicle subsystem templates (e.g rigid axle, suspension system, etc) to enable tailoring to suit a specific vehicle. Besides, existing driver models (e.g. PID control, preview control etc.) could be adapted for the tractor semitrailer model.

1.5 Deliverables

- Vehicle model in ADAMS/Car-Truck module tailored to a specific tractor semitrailer
- Methods to introduce environmental excitation (moving road and aerodynamic loads) and incorporate driver model in ADAMS/Car-Truck interface

1.6 Limitations

The following are considered to be the limitations of research in this master's thesis:

- Vehicle model parameters (e.g. mass/geometric/oscillatory parameters) will be taken from default Tractor-Semitrailer model in ADAMS/Car-Truck.
- Driver model parameters (e.g. PID coefficients; preview time,...) will be adopted from available literature.
- Aerodynamic coefficients are simulated without considering articulation angle between the tractor-semitrailer.

1.7 Stakeholders

- Norwegian Public Roads Administration, Oslo, Norway
- Division of Vehicle Engineering and Autonomous systems, Chalmers University of Technology, Gothenburg, Sweden

1.8 Social and ethical aspects

The E39 ferry-free coastal highway project aims at safe and sustainable transportation in western Norway. A superior understanding of the driver-vehicle behaviour on moving ground in extreme weather conditions is crucial to guarantee user and infrastructure safety. The results from this research will be acknowledged by NPRA and aid in creating recommendations for the safe operation of the Bjørnafjorden floating bridge. This report does not discuss the ethical dilemmas of building the bridge, its impact on ecology and sociopolitical agendas behind it.

2 LITERATURE REVIEW

2.1 Floating Bridge

Floating bridges are not a new concept but one that has existed since decades. A pontoon-supported bridge crossing Lake Washington was recognized as the longest floating bridge in the world for over 50 years. The Evergreen floating Bridge along State Route 520, which crosses Lake Washington in Medina, Washington, located to the east of downtown Seattle stole the record in 2016. The depth of the lake Washington's bed at the middle is 200 feet deep with poor soil conditions. Owned and maintained by the Washington State Department of Transportation (WSDOT), this bridge spans around 2.4 km in length and is supported by 77 pontoons [10]. Some of these pontoons are 75 feet wide and 360 feet long. Consisting of two general purpose lanes and a high-occupancy vehicle (HOV) lane in each direction, it is used by an average of 74000 motorists everyday. Credit to the sturdy engineering design, the bridge is resistant to winds up to 89 miles per hour ($\approx$ 40 m/s) and requires closure only during extreme windstorms. Although the Evergreen floating bridge improves transit reliability, investigations surrounding bridge-vehicle interactions subject to aerodynamic loads are not found in the literature [26].

When evaluating bridge-vehicle interactions, there are two common approaches. The first approach regards the bridge and vehicle as a coupled system. The mechanism here is one where the bridge vibration is due to vehicle movement and the vehicle vibration is due to the bridge movement. The second approach refers to the mechanism where bridge motion is used only as an input for vehicle motion and where the effect of vehicle motion on the bridge is considered insignificant [41].

HOU Yu-huai et al [16] established a mathematical model of a twin-hulled boat based floating bridge with elastic base beam in MSC.ADAMS. The floating bridge was reduced to a beam supported by springs to simulate buoyancy of static water. The ends of the bridge that connect to the land were modelled as a spring-damper with high stiffness. The vehicle is modelled similar to a quarter-car model in MSC.ADAMS/View based on the structural characteristics of the vehicle. The dynamic responses of a continuously hinged three dimensional floating bridge under the action of the vehicle was analyzed. It was revealed that the vehicle vibrational characteristics greatly influence the hinged joint and consequently the dynamic responses of the bridge. This investigation primarily focused on the response of the floating bridge. Furthermore, the vehicle model was considered to be a simplified moving mass or force. It does not study the vehicle dynamics due to the influence of bridge motion and aerodynamic effects.

Most current investigations regarding bridge-vehicle interactions on a floating bridge (Bjornafjorden floating bridge) subject to environmental loads are performed by Sekulic et al [9] [37] [38] [39], Bhat et al [17] and Gustaffson et al [26]. Sekulic et al [37] studied the influence of vertical bridge motion on ride comfort and road grip of a 3 DoF bus model. The study concluded that the weighted vertical accelerations of the driver was 'little uncomfortable' for a vehicle speed of 76 km/h. It also revealed that higher the vehicle speeds, higher is the Dynamic Load Coefficient (DLC) indicating greater variations in vertical forces leading to lower road grip. It has been suggested to investigate lateral and vertical dynamics of the vehicle that also include lateral bridge motion along with aerodynamic loads on complex vehicle models.

Gustaffson et al [26] established a method to investigate the driver influence on vehicle trackability on a motion platform. The study was conducted using a motion simulator CRUDEN for a simplified passenger car and a bus model at constant vehicle speeds. Vertical and lateral bridge motion were incorporated along with aerodynamic loads for a 1-year storm and a 100-year storm condition. Overtake maneuvers in both the vehicle models were tested with different drivers. In both the car and the bus, the results conclude greater difficulty in staying within the lane under bridge motion and aerodynamic loads compared to driving on a non-moving road without aerodynamic loads. The driver-vehicle responses also recorded higher and quicker steering efforts for a 100-year storm condition over a 1-year storm condition. Vertical motion was also recorded to be higher for the 100-year storm condition compared to the 1-year storm. Some of the suggested work is to use an improved vehicle model, add roll motion of the bridge and investigate effect of different road friction.

Bhat et al [17] continued the work performed by Gustaffson et al [26] with refined vehicle models along with the addition of roll motion of the bridge. Lane change and overtaking maneuvers along with straight line driving were carried out for less-than-1-year storm condition (W1 weather) up to a 100-year storm condition (W10 weather) with three drivers. Road roughness was not included in this study. Subjective and objective analysis indicate greater driver difficulty for more severe weather conditions compared to lower weather conditions for vehicle speeds between 70km/h and 110km/h. Lane change and the ability to stay within the lane was harder when driving a bus compared to that of the passenger car. Some of the future scope suggested include using MSC.ADAMS to analyse impact of vertical forces on the suspension system, carrying out investigations for articulated vehicles, and include different road surfaces.

Sekulic et al [9] also investigated lateral dynamics of an intercity bus model. In this work, an 8 DoF bus modelled in Matlab/Simulink was subject to all three bridge motions namely vertical, roll and lateral motions along with aerodynamic loads. The pure pursuit path tracking method based driver model [42] was used in this analysis. The results revealed that the mean and RMS value of hand steering wheel angle was higher for increasing vehicle speed that could cause difficulty for the driver to control the vehicle. The lane offset was also noticed to be greater with increase in vehicle speed. The risk of rollover was noticed at a vehicle speed of 108 km/h as the rear wheels on the windward side loses contact with the ground. The study recommends a safe vehicle operational speed of about 90 km/h up to weather 6 (1 year storm conditions). Furthermore, the Snider model does not consider the influence of crosswind load effects on the vehicle offset. Consequently it does not account for the lateral offset of the vehicle from its intended path. A proposal to include *steering compensation* as an improvement to the Snider model has been made.

2.2 Vehicle aerodynamic interactions

In the investigation of controllability and safety of vehicles, the effect of crosswinds on handling is prominent. For a high-sided tractor semitrailer vehicle, moderate and gusty crosswinds have both been found to significantly destabilize the lateral dynamics, since the vehicle has a high CoG, narrow wheelbase and large semitrailer area [9] [2] [47].

Cheli et al [19], investigated the crosswind stability of a typical lorry vehicle for straight line and U-turn maneuvers. Critical wind curves were determined based on the vehicle and wind gust speeds. Aerodynamic coefficients considered were a function of wind yaw angle only. It was determined that precomputing the actual trajectory of the vehicle in the pre-processing phase, was not possible attributing the wind gusts acting on the vehicle. It was also established that the aerodynamic forces must be calculated at each numerical step of the simulation, considering the instantaneous orientation of the vehicle. As a result, it was concluded that the aerodynamic forces are directly interfaced to the multibody vehicle model.

Chen and Cai [21], investigate the accident of non-articulated high-sided vehicle on the bridge under windy conditions. The bridge-vehicle-wind system is coupled, and external excitation is due to wind load and road roughness. Scenario in which the vehicle encroaches into the adjacent lanes or experiences a rollover was considered as an accident. The results indicate the rollover initiation at the rear axle, because of higher load transfer. Appropriate speed limits for driving on bridges and/or highways under wind gusts have often been determined by experienced intuition or subjective assessment of conditions. The research aims at determining scientific methods for traffic management in windy conditions. A comprehensive description of maximum driving speed under a range of wind speeds was provided. The research concludes that for wind speeds greater the 32 m/s, it is unsafe for operation of high-sided vehicles.

Drugge and Juhlin [23], established methods to determine aerodynamic loads on a bus under natural windy conditions. Controlling vehicle lateral position and yaw angle is important in avoiding accidents. Due to the rear biased weight distribution of buses, the center of gravity is often aft of CoP. This results in the aerodynamically unstable and crosswind sensitive characteristics of buses. Juhlin [3], investigates the crosswind sensitivity of buses in order to improve their performance under crosswinds. The high yaw moment transient peak when the rearward weight biased bus enters a gusty zone, resulting in large lateral deviations from desired path is an important conclusion. The research also establishes that crosswinds on low friction road surfaces leads to insufficient lateral forces from the steered wheels to maintain the trajectory of the vehicle. Juhlin and Eriksson [5], extend the research with a sensitivity study of buses subjected to crosswinds. The peak/mean ratio of yaw moment, exposed area to crosswinds and crosswind velocities are some significant aerodynamic parameters that influence directional stability in buses. It is concluded that weight distribution, vehicle weight and vehicle velocity have highest contributions to the yaw sensitive characteristics of buses.

Abdulwahab [2], uses a high-fidelity tractor semitrailer model from MSC ADAMS to investigate roll stability under gusty wind conditions. It was observed that the unsteady aerodynamic forces generating from wind gusts with 90°yaw angle, lead to maximum roll moments and lateral deviation from desired path. The aerodynamic forces were determined and applied at the CoP point. It is necessary to highlight that the author considered a single point of force application for a multi-unit vehicle. The research concludes with a more realistic way of determining vehicle rollover by considering vehicle dynamics and aerodynamics in a coupled simulation to determine LTR. Reduction in roll stability was observed when the vehicle enters or exits a gusty zone. Vehicle speed, mass, locations of CoP and roll centers were factors concluded to have significant effects on the roll stability of the vehicle.

Sekulic et al [9], in describing the effects of crosswind on an intercity bus on the Bjørnafjorden bridge crossing, determine the aerodynamic loads at the CoG bus vehicle model. The aerodynamic coefficients are generated from wind tunnel experiments and CFD simulations at the midpoint of line joining front and rear axle centers (reference point). Both research cases [9] [2], include the effect of wind yaw angle in determining aerodynamic coefficients through CFD simulations and verifying it with scaled wind tunnel experiments. The methods to determine aerodynamic force and moment coefficients were similar. The magnitudes of wind velocity components in both cases were similar to the space-time distribution of the W6 weather condition considered for this research.

2.3 Research gap

In summary, investigations in respect to vehicle dynamics for passenger car and bus on a floating bridge exposed to aerodynamic crosswinds subjected to different weather conditions have been performed. Results suggest greater difficulty in controlling the bus compared to a passenger car under similar conditions. It is imperative to investigate the vehicle dynamics concerning commercial vehicle transport segment particularly because of the characteristic large side area that make these vehicles sensitive and susceptible to aerodynamic crosswinds. Consequently, the operation of commercial vehicle segments exposed to the foreseen storm conditions could affect vehicle stability and threaten the safe operation of the Bjornafjorden floating bridge for traffic. Furthermore, the commercial vehicle segment predominantly consist of multi-unit articulated vehicles that are popular within the Scandinavian region. Studies on vehicle stability of a tractor semitrailer subjected to aerodynamic crosswinds have been performed albeit without environment load of a floating bridge as an additional vehicle input. Furthermore, driver influence on vehicle track-ability on floating bridges have not been performed with the established method on a motion platform simulator.

Having identified the prevailing research gap, the first goal of this master thesis is to establish a bridge-vehicle-wind system and investigate the influence of floating bridge motion and wind loads on vehicle-driver behaviour. In the quest of establishing a bridge-vehicle-wind system in this master's thesis, the bridge-vehicle interaction is considered under the premise where the bridge motion is used only as an input for the vehicle motion since the mass of the floating bridge is much greater than the mass of the considered vehicle. Furthermore, one single vehicle is considered to run on the floating bridge in this investigation (absence of traffic flow on the floating bridge). The second aim is to investigate vehicle stability for one vehicle type and specific storm conditions (the 1-year storm condition case). The final goal of this investigation is to recommend appropriate speeds for safe vehicle driving across the Bjørnafjorden floating bridge (South-North direction). A 627 DoF tractor semitrailer vehicle model from MSC.ADAMS will be used for this study. The investigations will be made with a pure pursuit path tracking method based driver model (Snider,2009) [42] and an advanced driver model that is equipped with lateral path offset compensator along with feedback control. Furthermore, aerodynamic loads will be resolved for the tractor unit and the semitrailer unit separately. The study will be carried out under different constant vehicle speeds for a laden and unladen vehicle on dry/wet road surface with a friction of 0.7 and a road surface with low friction of 0.3.

High speed transient off-tracking for long heavy combination vehicles is the overshoot in the lateral distance between the paths of the centre of the front axle and the centre of the most severely off-tracking axle of any unit in a specified manoeuvre at a certain friction level and a certain constant longitudinal speed [30]. Consequently, the lane deviation semitrailer unit is of particular interest to be analyze lane violation.

Un-tripped transient roll-overs can occur when long combination heavy vehicles are exposed to crosswinds combined with volatile steering corrections. This can trigger roll eigenmodes which can be amplified due to the unlucky timing between the steering corrections in combination with the aerodynamic crosswind gusts [30]. Therefore, Load Transfer Ratio (LTR) and wheel lift-off incidences are of particular interest to study the risk of vehicle roll-over.

These parameters indicate the increased risk for a swing out or rollover of the last unit compared to what the driver is experiencing in the lead unit. Furthermore, driver steering effort is also analyzed from the Handwheel Steering Angle (HSA) signals and its RMS values to indicate driver difficulty under different driving scenarios.

3 THEORY

3.1 Aerodynamics

3.1.1 Equations for force and moments

The equations governing the aerodynamic forces (drag, side force and lift) and moments (roll, pitch and yaw) are expressed in equations 3.1.

$$\begin{aligned}
F_{x,wind} &= \frac{1}{2}\rho A V_{rel}^2 c_d(\beta_w) \\
F_{y,wind} &= \frac{1}{2}\rho A V_{rel}^2 c_s(\beta_w) \\
F_{z,wind} &= \frac{1}{2}\rho A V_{rel}^2 c_l(\beta_w) \\
M_{x,wind} &= \frac{1}{2}\rho A L V_{rel}^2 c_{roll}(\beta_w) \\
M_{y,wind} &= \frac{1}{2}\rho A L V_{rel}^2 c_{pitch}(\beta_w) \\
M_{z,wind} &= \frac{1}{2}\rho A L V_{rel}^2 c_{yaw}(\beta_w)
\end{aligned} \tag{3.1}$$

where,

ρ : density of air $[Kg/m^3]$
A : frontal projected area of the vehicle $[m^2]$
L : Length of the vehicle (wheelbase) $[m]$
V_{rel} : magnitude of relative velocity $[m/s]$
$F_{x,wind}$: drag force due to wind excitations (X-direction) $[N]$
$F_{y,wind}$: side force due to wind excitations (Y-direction) $[N]$
$F_{z,wind}$: lift force due to wind excitations (Z-direction) $[N]$
$M_{x,wind}$: roll moment due to wind excitations (X-direction) $[Nmm]$
$M_{y,wind}$: pitch moment due to wind excitations (Y-direction) $[Nmm]$
$M_{z,wind}$: yaw moment due to wind excitations (Z-direction) $[Nmm]$
c_d : aerodynamic drag coefficient
c_s : aerodynamic side force coefficient
c_l : aerodynamic lift coefficient
c_{roll} : aerodynamic roll moment coefficient
c_{pitch} : aerodynamic pitch moment coefficient
c_{yaw} : aerodynamic yaw moment coefficient

3.2 Driver model

3.2.1 Pure Pursuit Method

A popular class of path tracking methods found in robotics is that of geometric path trackers. A look ahead distance in front of the vehicle to the desired path is used as a measure of error and the control law solutions to these problems is determined through geometric relationships between the vehicle and the path. The Pure Pursuit method and Stanley method are commonly used for these applications [42].

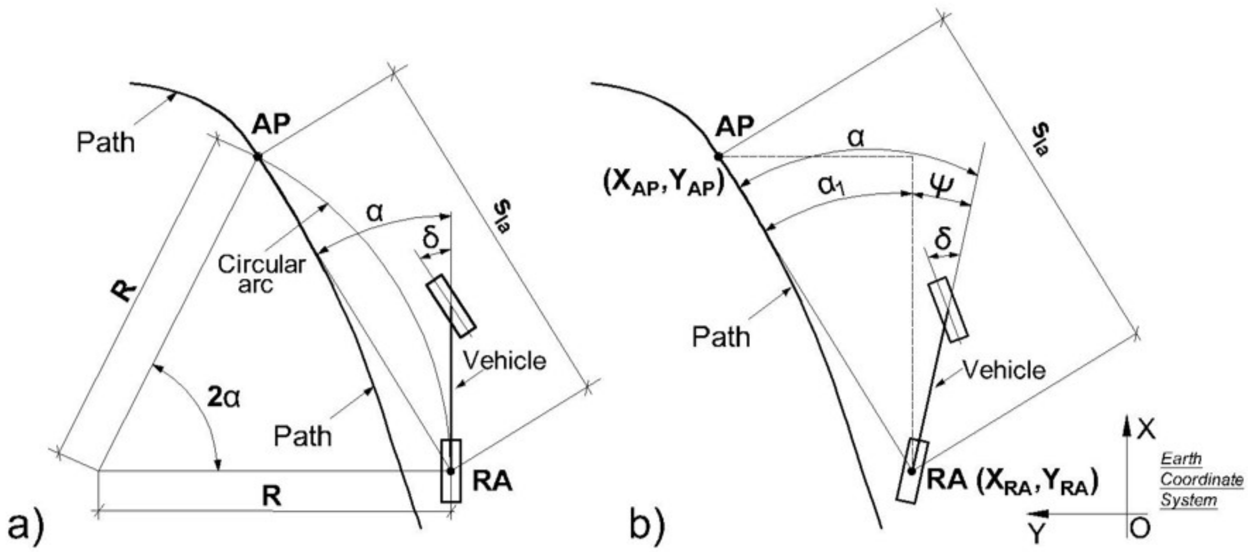

Figure 3.1: *a) Pure Pursuit Geometry; b) positions of the characteristic points and angles [42] [9]*

The vehicle's rear axle position RA (X_{RA}, Y_{RA}) and the location of the aim point or preview point AP (X_{AP}, Y_{AP}) on the path are determined (Figure 3.1). When calculating location of the aim point, a look-ahead distance or preview distance s_{la} has been considered from the current rear axle position. Having worked out the coordinates of the points RA and AP, angle α can be formulated as

$$\alpha = \alpha_1 + \psi = \sin^{-1}\left(\frac{Y_{AP} - Y_{RA}}{s_{la}}\right) + \psi \tag{3.2}$$

where ψ is the yaw angle of the vehicle. The steering angle δ is established using the angle α such that

$$\delta = \left(\frac{2L\alpha}{s_{la}}\right) = \left(\frac{2L\alpha}{t_{la} v_x}\right) \tag{3.3}$$

where α is the angle between the vehicle's heading direction and the look-ahead vector; L is the wheelbase of the vehicle; t_{la} is the look-ahead time (LAT); and v_x is the constant vehicle longitudinal speed. The handwheel steering angle (HSA) is consequently calculated through the steering ratio.

3.2.2 Machine Control - MSC ADAMS

This section is an excerpt from MSC.ADAMS documentation [12] [13] [14]. Machine Control is a vehicle controller that can be used to simulate the control actions of a driver. The actions of a driver are simulated by operating the steering, pedals, and gears of a simulated vehicle.

Machine Control determines control actions such that a simulated vehicle can follow meaningful combinations of a specified path along a 2D or 3D road, a specified curvature, a specified lateral acceleration, a specified longitudinal velocity and a specified longitudinal acceleration. Machine Control's control action combines a reference trajectory planner and a model-predictive controller (MPC), sometimes known as a feed-forward plus feedback controller.

At the trajectory planning stage, targets for the vehicle and driver behavior and some basic parameters describing the characteristics of the simulated vehicle are taken into account, and a realistic trajectory that most closely satisfies the targets is identified (for example, path, speed, and acceleration).

Machine Control uses simple mathematical models of vehicle dynamics, such as a bicycle model, a particle model, and a kinematic drive train model, to estimate the necessary control actions, such as the steering angle and throttle position. Machine Control applies these estimated controls as inputs to the simulated vehicle in a feed-forward manner, such that approximately correct control actions are applied without delay.

Differences between the behavior of the simulated vehicle and the expected behavior (that is, the behavior of the idealized models employed by the controller) are corrected continuously using feedback controllers, which adjust the control actions to minimize the error between the reference trajectory and the actual vehicle behavior.

Feed Forward Lateral control

Consider a vehicle as seen from a bird's eye perspective, with global axes x-y, local axes X-Y, the vehicle path, and the global yaw angle θ as seen in the figure 3.2:

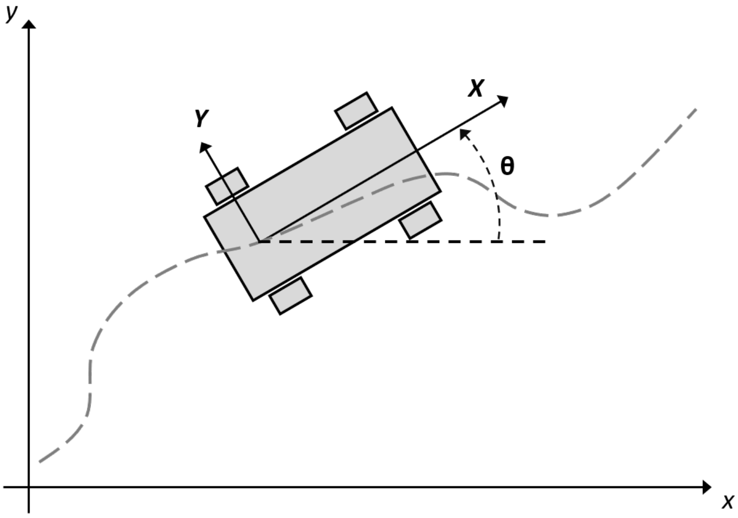

Figure 3.2: *Bird's-eye view of vehicle path*

The projection of the vehicle path onto the ground plane is related to the velocities and global heading as:

$$\begin{aligned} \dot{x} &= V_x cos(\theta) - V_y sin(\theta) \\ \dot{y} &= V_x sin(\theta) - V_y cos(\theta) \end{aligned} \tag{3.4}$$

where (X, Y) is the global position of the vehicle, (V_x, V_y) are the velocities of the vehicle relative to vehicle-fixed axes and θ, the global heading of the vehicle.

The feed-forward component of the lateral control action is computed by assuming that the simulated vehicle responds as a bicycle model. The simplicity of the bicycle model allows the analytical identification of the relationship between the geometry of the path and the necessary control action (steering angle), and vice-versa.

In a bicycle model, the lateral forces from both tires on an axle are assumed to act in the same direction, and the left and right steer angles are assumed to be the same. In other words, Ackerman steering geometry is not considered. With these assumptions, the tires may be lumped together into a single tire representation, and the model is guided by a single steer angle.

This simplified model is used to identify the necessary steer angle required for the vehicle to follow the specified target.

Simplification of the vehicle to the bicycle model

The form of the bicycle model employed by Machine Control assumes pure rolling of the front and rear tires with no kinematic or compliance-steer effects, and therefore, no lateral velocity at the rear axle. Note that this does not imply zero sideslip at the center of mass.

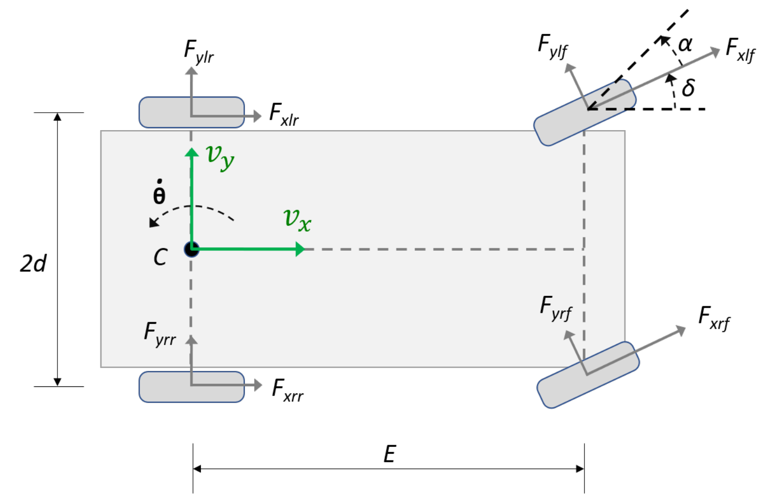

Figure 3.3: *2-track vehicle model*

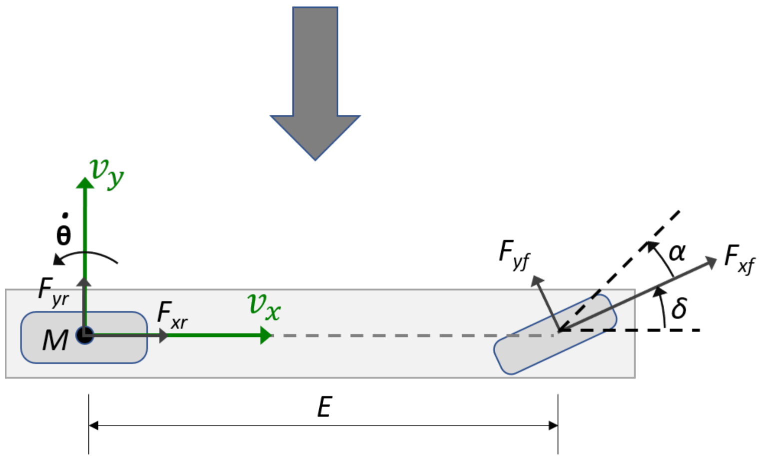

Figure 3.4: *Bicycle model*

If the origin of the vehicle-fixed local axis system shown above is selected to be the center of the rear axle (not the center of mass), then the lateral velocity V_y is now always assumed to be zero, and the assumed path of the vehicle simplifies to:

$$\begin{aligned} \dot{x} &= V_x cos\theta \\ \dot{y} &= V_x sin\theta \end{aligned} \tag{3.5}$$

where

$$\dot{\theta} = \rho V_x \tag{3.6}$$

$\dot{\theta}$ is the rate of change of the direction of the path at the rear axle (note that this is not equal to the yaw rate of the vehicle).

In this case, the center of the turn always lies on a line through the rear axle. The steer angle required to yield a certain path curvature is then always equal to the Ackerman angle, and is independent of the vehicle speed V_x:

$$\delta = \delta_A = tan^{-1}\Big(\frac{E}{R}\Big) = tan^{-1}(E\rho) \tag{3.7}$$

where E represents the wheelbase of the vehicle, R denotes the radius of the curvature at the rear axle and ρ is the curvature of the path of the rear axle ($\rho = \frac{1}{R}$).

Therefore, this single steer angle input to the bicycle model controls the radius of turn and the curvature of the path. A simple inversion of this equation enables an estimate of the necessary steer angle to be calculated and applied to the simulated vehicle in a feed-forward sense.

Trajectory Control - Connecting Contour

For the lateral control of the vehicle with a target path, a simple model of the vehicle (Figure 3.4) is used to compute the control action that should cause the vehicle to follow the intended path. The simulated vehicle, however, may not exactly follow the target path because of differences between the simplified model and the simulated vehicle, or external factors (road roughness and aerodynamic disturbances).

Therefore, the potential for offset between the instantaneous vehicle location and heading, and the location and heading of the path must be considered. In considering the location and heading of the path, Machine Control builds a connecting contour between the current vehicle position (wherever it may be) and some point on the target path, along which the vehicle will be steered to later bring it back to the target path

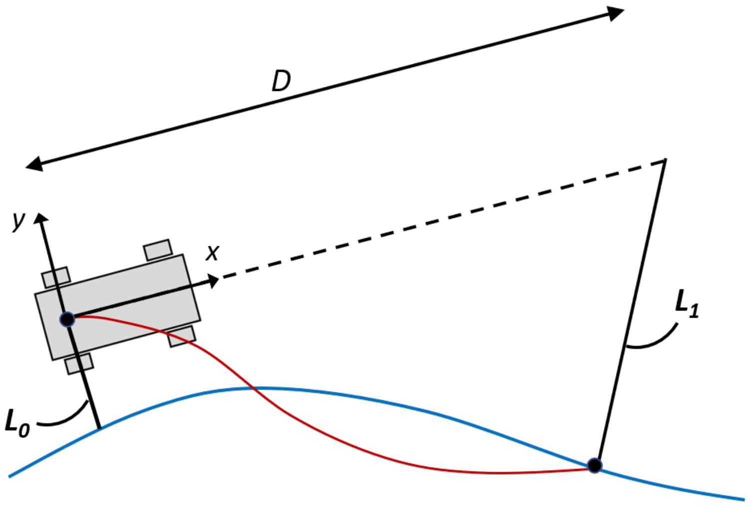

Figure 3.5: *Connecting Contour*

where D: preview distance = max(minimum, preview time * speed) - distance ahead from the current vehicle (gyro point) position to locate preview point.

L_0:- path distance - distance from current vehicle (gyro point) position to the nearest point on the path, projected on the road surface.

L_1: preview point distance - distance from preview point to the nearest point on the path, projected on the road surface.

The function that describes the connecting contour is parameterized such that one end of the connecting contour matches the position and direction of the vehicle (at the vehicle rear axle) and the other end of the connecting contour matches the path (at the preview distance, where the contour connects with the target path), as shown in the Figure 3.5. The most potent (effective) adjustment to the connecting contour is the preview distance, which is typically controlled by changing the preview time. The connecting contour then becomes the reference trajectory (path) for the lateral control of the vehicle, and the vehicle is steered by both feed-forward and feedback controllers, such that it should follow this connecting contour. The connecting contour is updated each time the Machine Control controller is called.

Lateral Displacement Feedback (Path Distance Compensation)

The connecting contour approach does not include any term to correct for steady-state lateral displacement error. This is preferred in most situations, because the resulting control actions tend to be more realistic and robustly stable. Once the vehicle is close to the target path, an additional controller acting on the distance L_0 (path_distance) adjusts the lateral displacement of the vehicle:

$$\delta_{LDC} = K_{LDC} + \int_0^t f_{LDC} L_0 \, dt \tag{3.8}$$

where f_{LDC} is a flag indicating whether the lateral displacement controller is activated, that is whether the lateral displacement error L_0 is small.

Summation of Feed-Forward and Feedback Terms

A simple summation of the feed-forward and feedback terms gives the total demand from the lateral controller for steer angle:

$$\delta = \delta_{FF} + \delta_{FB} + \delta_{LDC} \tag{3.9}$$

3.3 MSC.ADAMS Solver Setting

This section is an excerpt from MSC.ADAMS documentation [12] [13] [14]. One can use the INTEGRATOR statement to select an integrator when choosing to perform a dynamic analysis. The dynamic analysis of a mechanical system consists essentially of numerically integrating the nonlinear differential equations of motion.

Ordinary differential equations (ODEs) can be characterized as being stiff or non-stiff. A set of ODEs is said to be stiff when it has widely separated eigenvalues (low and high frequencies) with the high frequency eigenvalues being overdamped. Therefore, while the system has the ability to vibrate at high frequencies, it usually does not because of the associated high damping, which dissipates this mode of motion.

The stiffness ratio of a set of ODEs is defined as the highest inactive frequency divided by the highest active frequency. Stiff ODEs typically have a stiffness ratio of 200 or higher. In contrast, non-stiff systems have a stiffness ratio less than 20. This basically means that for a non-stiff system of ODEs, the higher frequencies of the system are active. The system can and does vibrate at these frequencies.

An example of a stiff system is a flexible body in which the higher frequencies have been damped out completely, leaving only the lower frequency vibration modes active.

The system above becomes non-stiff if the higher frequencies are excited by an external force. Nonlinear ODEs can be stiff at some points in time and non-stiff at other points.

Stiff and Non-Stiff Integrators

Integrators are classified as stiff or non-stiff. A stiff integrator is one that can handle numerically stiff systems efficiently. For stiff integrators, the integration step is limited by the inverse of the highest active frequency in the system. For non-stiff integrators, the integration step is limited by the inverse of the highest frequency (active or inactive) in the system. Thus, non-stiff integrators are notoriously inefficient for solving stiff problems.

Because many mechanical systems are numerically stiff, the default integrator in MSC.ADAMS Solver (C++) is GSTIFF, a stiff integrator that is based on the DIFSUB integrator developed by C.W. Gear. Gear's DIFSUB integrator is unrelated to the MSC.ADAMS Solver subroutine that is known by the same name. WSTIFF is another stiff integrator available in MSC.ADAMS Solver (C++). Both GSTIFF and WSTIFF integrators are based on Backward-Difference Formulae (BDF) and are multi-step integrators. The solution for these integrators occurs in two phases: a Prediction followed by a Correction.

Prediction

When taking a new step, the integrator fits a polynomial of a given order through the past values of each system state, and then extrapolates them to the current time to perform a prediction. Standard techniques like Taylor's series (GSTIFF) or Newton Divided Differences (WSTIFF) are used to perform the prediction.

Prediction is an explicit process in which only past values are considered, and is based on the premise that past values are a good indicator of the current values being computed. The predicted value does not guarantee that it will satisfy the equations of motion or constraint. It is simply an initial guess for starting the correction, which ensures that the governing equations are satisfied.

The degree of polynomial used for prediction is called the order of the predictor. For example, a predictor of order 3 will fit a cubic polynomial that includes the past 4 values for each state. Clearly, if the governing equations are smooth, the prediction will be quite accurate. On the other hand, if the governing equations are not smooth, the prediction can be quite inaccurate.

Correction

The corrector formulae are an implicit set of difference relationships (BDFs) that relate the derivative of the states at the current time to the values of the states themselves. This relationship transforms the nonlinear differential algebraic equations to a set of nonlinear, algebraic difference equations in the system states. The Backward Euler integrator is an example of a first-order BDF. Given a set of ODEs of the form $dy/dt =$ f (y,t), the Backward Euler uses the difference relationship:

$$y_{n+1} = y_n + h \cdot \dot{y}_{n+1} \tag{3.10}$$

where:

- y_n is the solution calculated at t $= t_n$.
- h is the step size being attempted.
- y_{n+1} is the solution at $= T_{N+1}$, which is being computed.

Notice that the subscript n+1 is on both sides of Equation 3.10. This is an implicit method.

MSC.ADAMS Solver (C++) uses an iterative, quasi-Newton-Raphson algorithm to solve the difference equations and obtain the values of the state variables. This algorithm ensures that the system states satisfy the equations of motion and constraint. The Newton-Raphson iterations require a matrix of the partial derivatives of the equations being solved with respect to the solution variables. This matrix, known as the Jacobian matrix, is used at each iteration to calculate the corrections to the states.

Assume that the equations of motion have the form:

$$F(y, \dot{y}, t) = 0 \tag{3.11}$$

where y represents all the states of the system.

Linearizing Equation 3.11 about an operating point $y = y^k$ and $\dot{y} = \dot{y}^k$ gives

$$F(y, \dot{y}, t) = F(y^k, \dot{y}^k, t) + \left.\frac{\partial F}{\partial y}\right|_{y^k, \dot{y}^k} (y - y^k) + \left.\frac{\partial F}{\partial \dot{y}}\right|_{y^k, \dot{y}^k} (\dot{y} - \dot{y}^k) = 0 \tag{3.12}$$

replacing $(y - y^k)$ with Δy and $(\dot{y} - \dot{y}^k)$ with $\Delta \dot{y}$, we get:

$$F(y, \dot{y}, t) = F(y^k, \dot{y}^k, t) + \left.\frac{\partial F}{\partial y}\right|_{y^k, \dot{y}^k} (\Delta y) + \left.\frac{\partial F}{\partial \dot{y}}\right|_{y^k, \dot{y}^k} (\Delta \dot{y}) = 0 \tag{3.13}$$

From Equation 3.10, which is a first-order BDF, we get the relationship:

$$\Delta \dot{y} = \frac{1}{h} \Delta y \tag{3.14}$$

Substituting Equation 3.14 into 3.13:

$$\left[\left.\frac{\partial F}{\partial y}\right|_{y^k, \dot{y}^k} \quad + \quad \frac{1}{h} \left.\frac{\partial F}{\partial \dot{y}}\right|_{y^k, \dot{y}^k} \right] \Delta y \quad = \quad -F(y^k, \dot{y}^k, t) \tag{3.15}$$

A generalization of equation 3.15 to higher-order BDFs gives:

$$\left[\left.\frac{\partial F}{\partial y}\right|_{y^k,\dot{y}^k} \quad + \quad \frac{1}{h\beta_0}\left.\frac{\partial F}{\partial \dot{y}}\right|_{y^k,\dot{y}^k} \right] \Delta y \quad = \quad -F(y^k,\dot{y}^k,t) \tag{3.16}$$

where:

- β_0 is a scalar that is characteristic to an integration order. This scalar is constant for each integration order.
- The matrix on the left side of Equation 3.16 is the Jacobian matrix of F.
- Δy are the corrections.
- F is the residue of equations (equation imbalances).

The corrector is said to have converged when the residue F and the corrections y have become small.

After the corrector has converged to a solution, the integrator estimates the local integration error in the solution. This is usually a function of the difference between the predicted value and the corrected value, the step size, and the order of the integrator. If the estimated error is greater than the specified integration ERROR, the integrator rejects the solution and takes a smaller time step. If the estimated error is less than the specified local integration ERROR, the integrator accepts the solution and takes a new time step. The integrator repeats the prediction-correction-error estimation process until it reaches the time specified in the SIMULATE command.

GSTIFF

GSTIFF is based on the DIFSUB integrator. GSTIFF is the most widely-used and tested integrator in MSC.ADAMS Solver (C++). It is a variable-order, variable-step, multi-step integrator with a maximum integration order of six. The BDF coefficients it uses are calculated by assuming that the step size of the model is mostly constant. Thus, when the step size changes in this integrator, a small error is introduced in the solution. This formulation offers the benefits of high speed, high accuracy of the system displacements, and is robust in handling a variety of analysis problems. A limitation is that velocities and especially accelerations can have errors. Another limitation of this formulation is that one can also encounter corrector failures at small step sizes. These occur because the Jacobian matrix is a function of the inverse of the step size and becomes ill-conditioned at small steps.

The $I3$ formulation specifies that the Index-3 (I3) formulation be used. The $SI2$ formulation specifies that the Stabilized Index-2 (SI2) formulation in conjunction with the GSTIFF (C.W.Gear stiff), WSTIFF (Wielenga stiff), or HASTIFF (Hiller-Anantharaman stiff) integrators, be used for integrating the equations of motion. The SI2 formulation takes into account constraint derivatives when solving for equations of motion. This process enables the GSTIFF and WSTIFF integrators to monitor the integration error of velocity variables, and, therefore, renders highly accurate simulations. A positive side effect of the SI2 formulation is that the Jacobian matrix remains stable at small step sizes, which in turn increases the stability and robustness of the corrector at small step sizes. One of the limitations however is that the SI2 formulation is typically 25 % to 100 % slower for most problems than regular GSTIFF, when run with the same error.

In this work, the solver settings in MSC.ADAMS/Car Truck were set to the GSTIFF-I3 formulation.

4 MSC ADAMS/Car Truck - Vehicle Model

This chapter is an excerpt from MSC.ADAMS documentation [12] [13] [14].

4.1 Vehicle Model

The vehicle model in the *shared_truck* database in MSC.ADAMS represents an 18-wheel tractor semitrailer assembly with an approximate GVW of 38t distributed over five axles. The tractor and semitrailer have rigid chassis. The tractor unit has a wheel base of approximately 5.7m, while the wheel base of the whole vehicle is around 17.5m with a track width of about 2.55m. The tractor unit alone has a mass of about 10.8t while the default payload is 17t. The multi-body dynamic tractor semitrailer vehicle model has a total of 190 moving parts with 627 degrees of freedom (DoF).

4.1.1 Tractor

The rigid tractor system (Figure 4.1) forms the basic frame of the tractor to which the cab, suspension and other sub-assemblies connect through flexible couplings (bushing). The trailer is hitched to the tractor through the fifth wheel. The cab consists of three boxes representing the engine, driver and sleeping compartments. The cab suspension and bushings mount the cab on a rigid tractor frame. The powertrain template is functional representation based on an internal combustion engine, clutch and a gearbox model. The engine combustion model takes the throttle demand and produces a crankshaft torque as a result of a three dimensional spline interpolation. Independent variables are engine RPM and throttle position. Torque is divided with inter- and intra-axle differentials. Air tanks and other rigid bodies are attached to the mount parts via bushings. All the auxiliary components like exhaust, air tank, fuel tank, etc. are rigidly attached to the cab and tractor frame using fixed or flexible joints.

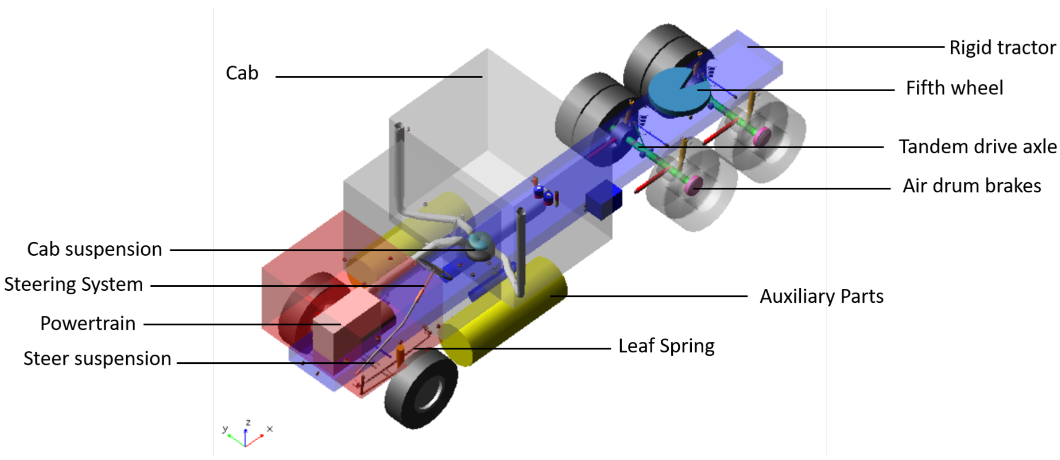

Figure 4.1: *Tractor Unit*

The steering system is a simple re-circulating ball, pitman arm steering system, with power assist. It is commonly used in heavy trucks. It consists of a three-bar mechanism: pitman arm, steering link, and steering input arm. A re-circulating ball steering gear transmits motion from the steering wheel to the pitman arm. The pitman arm rotates to impart motion to the steering link. The steering link pulls and pushes the steering input arm which steers the wheels.

The steerable front suspension seen in Figure 4.2 comprises of the tie rod, steering arm and axle that form a four bar chain with two revolute and two spherical joints. The suspension upright forms the wheel carrier part. The solid axle in turn supports leafspring suspension and dampers. The steering input arm (in steering subsystem) connects to the left suspension upright. The leaf spring template is a representation of the conventional semi-elliptical suspension spring used in a solid axle vehicle. The leaf seat mounts the leaf spring to the axle. The front eye is directly connected to the chassis through a bushing, whereas the rear eye is connected through a shackle with intermediate bushings.

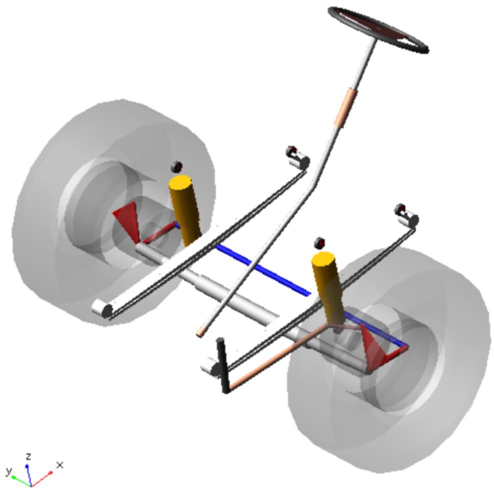

Figure 4.2: *Steerable front suspension*

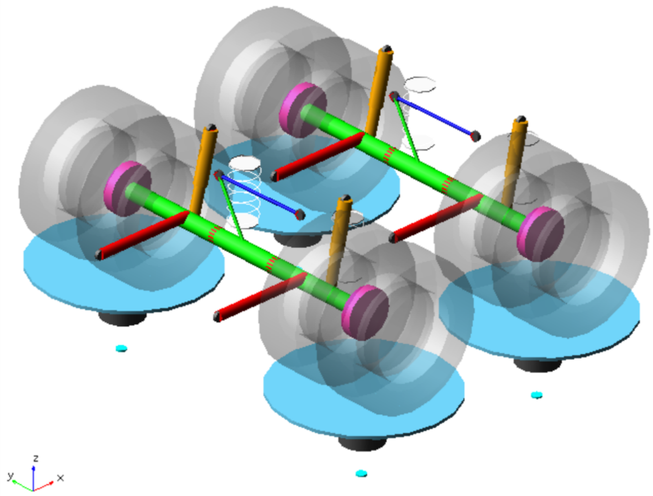

Figure 4.3: *Solid twin axle suspension*

Figure 4.3 represents the solid twin axle suspension typically used on tractors. The template is used in conjunction with the dual tire template in the tractor assembly as the driving solid axle. Longitudinal load is reacted by the rigid hockey sticks and lateral load is reacted by the panhard rod. Drive torque left and right are applied as rotational single component forces between hub parts and the solid axle. A simple model of a limited slip differential is also included in this suspension template. There are no rigid parts or gears in the axle differential unit: a differential torque is transferred from one hub to the other, depending on the difference of the wheel rotational speeds. The rotational speeds of the left and right half shafts are computed in a user defined solver variable and their difference is used as independent variable in the akima interpolation of the limited slip differential spline. An input communicator of type solver variable receives the total axle torque. That value, corrected with the appropriate differential torque, is then referenced in the two joint force actuators. The joint force actuators produce the driving torque between the rotating hub parts and the solid axle.
The drum-brake system template represents an air brake device that applies resistance to the motion of a vehicle. The drum-brake system template represents a model of air brake system. It converts the brake line pressure to brake torque which is applied to the wheels. This template models the brakes at three axles.

4.1.2 Semitrailer

The template (Figure 4.4) represents a trailer frame similar to the tractor frame which carries the payload and is hitched to the tractor through the fifth wheel. The rigid trailer system forms the basic frame of the trailer which is hitched to the tractor through the fifth wheel.

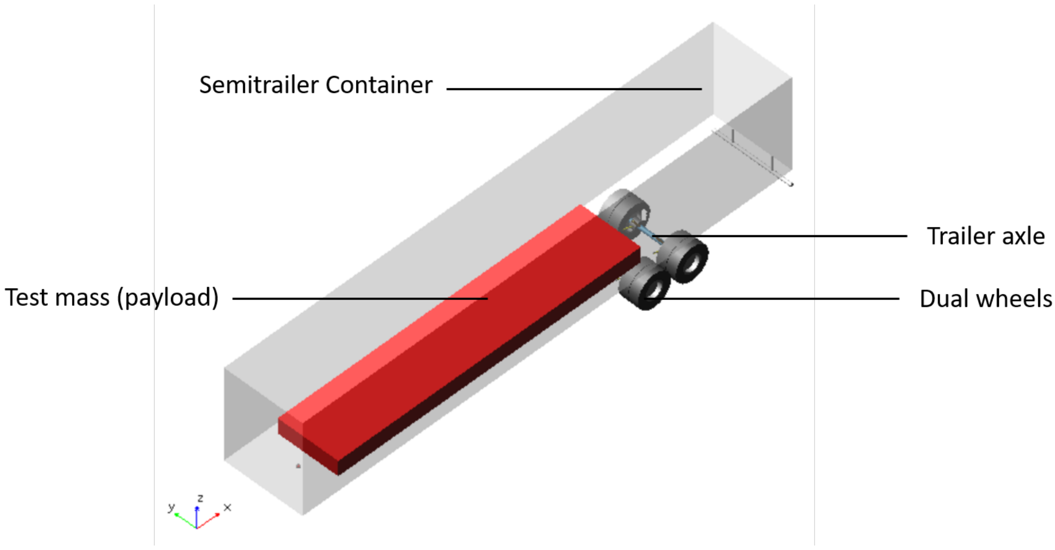

Figure 4.4: *Trailer Unit*

This template represents a solid axle suspension typically used on trailers. The template represents a simple rigid axle trailing-arm suspension with springs and shock absorbers. Dual wheels are mounted on the axle to make the complete suspension system. It also connects to the brake templates. Hub parts are connected to the solid axle via rotational joints. Dual wheel template mounts to the hubs. The suspension is connected to the trailer subsystem via mount parts at the springs and dampers.

The dual wheel template represents a dual wheel arrangement on drive and trailer axles of the truck. It uses the tire property file and supports three basic functions: (i) Supports vertical load (ii) Develops longitudinal forces for acceleration and braking (iii) Develops lateral forces for cornering. The dual wheel system template consists of wheel parts rigidly connected to mount parts. The tire contact patch forces are transformed in forces and torques applied at the hub. The road property file determines the road contact model.

4.1.3 Tire Model

Magic-Formula (MF) tire models are considered the state-of-the-art for modeling tire-road interaction forces in vehicle dynamics applications. Since 1987, Pacejka and others have published several versions of this type of tire model. The PAC2002 contains the latest developments that have been published in Tyre and Vehicle Dynamics by Pacejka [1]. In general, a MF tire model describes the tire behavior for rather smooth roads (road obstacle wavelengths longer than the tire radius) up to frequencies of 8 Hz. For modeling roll-over of a vehicle, you must pay special attention to the overturning moment characteristics of the tire (M_x) and the loaded radius modeling. The PAC2002 model has proven to be applicable for car, truck, and aircraft tires with camber (inclination) angles to the road not exceeding 15 degrees.

Originally, Pacejka models have been developed for handling maneuvers at smooth road, as described above. However the PAC2002 has extended functionality that increases the validity towards short road obstacle wavelengths (with use of the 3D Enveloping Contact) and higher frequencies (up to 70 - 80 Hz) by using the tire belt dynamics modeling. The standard tire from the MSC.ADAMS/Tire library is used in this study with the tire dimension of 315/80 R22.5 without tire belt dynamics modelling.

The Magic Formula is a mathematical formula that is capable of describing the basic tire characteristics for the interaction forces between the tire and the road under several steady-state operating conditions. For pure slip conditions, the lateral force F_y as a function of the lateral slip α, respectively, and the longitudinal force F_x as a function of longitudinal slip κ, have a similar shape (see Figure 4.5).

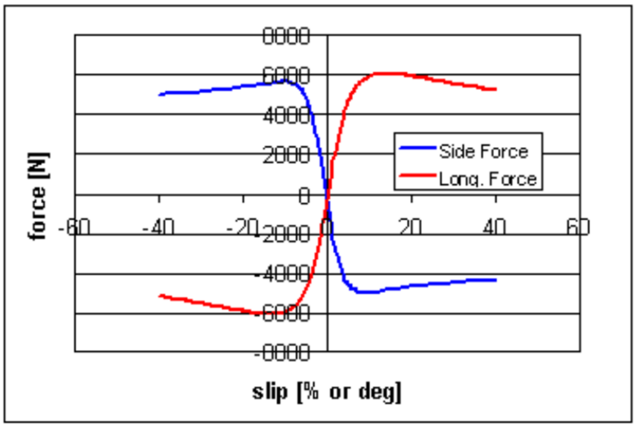

Figure 4.5: *Characteristic Curves for Fx and Fy under pure slip conditions*

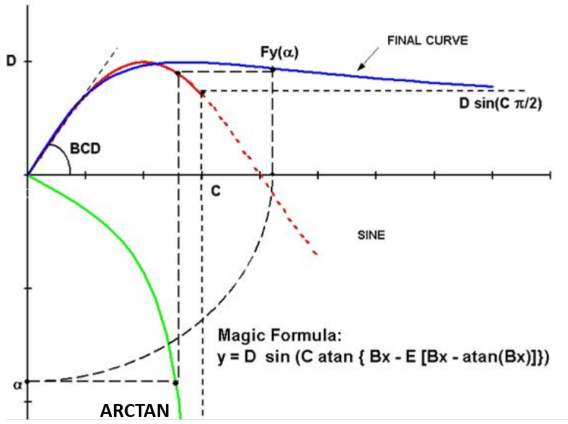

Figure 4.6: *The Magic Formula and the meaning of its parameters*

Because of the sine - arc tangent combination, the basic Magic Formula equation is capable of describing this shape:

$$Y(x) = D \cdot sin[C \cdot arctan\{B \cdot x - E \cdot (B \cdot x - arctan(B \cdot x))\}] \tag{4.1}$$

where Y(x) is either F_x with x the longitudinal slip κ, or F_y and x the lateral slip α.
where:

- D: is called the peak factor, which determines the peak of the characteristic curve.
- C: factor determines the part used within the sine function and, therefore, mainly influences the shape of the curve (shape factor).
- B: factor stretches the curve and is called the stiffness factor.
- E: factor can modify the characteristic around the peak of the curve (curvature factor).

4.2 Aerodynamic coefficients

The aerodynamic coefficients are determined by CFD simulations and experimentally verified through scaled models (Sekulic, 2021) [9]. The wind tunnel setup consists of a turntable platform. The CFD simulations were carried out with the following reference points (yellow stars) as shown in figure 4.7:

- Midpoint of the tractor first axle, projected on the ground
- Midpoint of the semitrailer first axle, projected on the ground

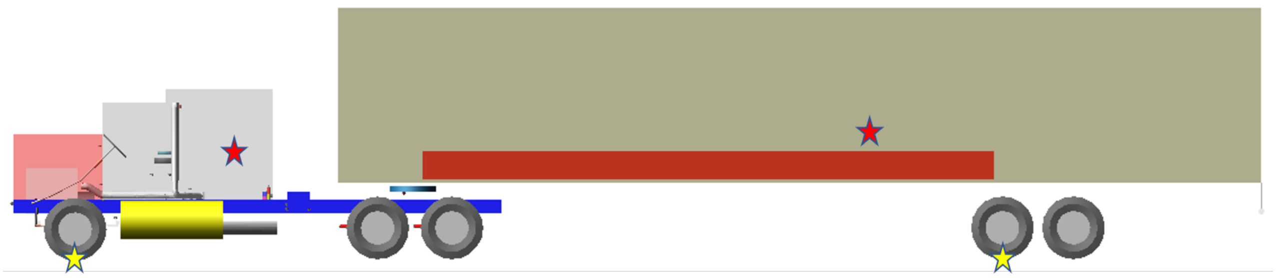

Figure 4.7: *CFD reference points*

The dimensionless aerodynamic coefficients were determined about these reference points for a wind yaw angle sweep from 0°to 90°, at a 3°interval, through the CFD simulations. For this master thesis research, these coefficients were linearly interpolated as required (look-up table interpolation), to calculate the aerodynamic force and moment coefficients for every wind yaw angle between 0°and 90°as shown in figure 4.8. This study does not consider the effect of the articulation between the tractor and semitrailer units while determining the aerodynamic coefficients.

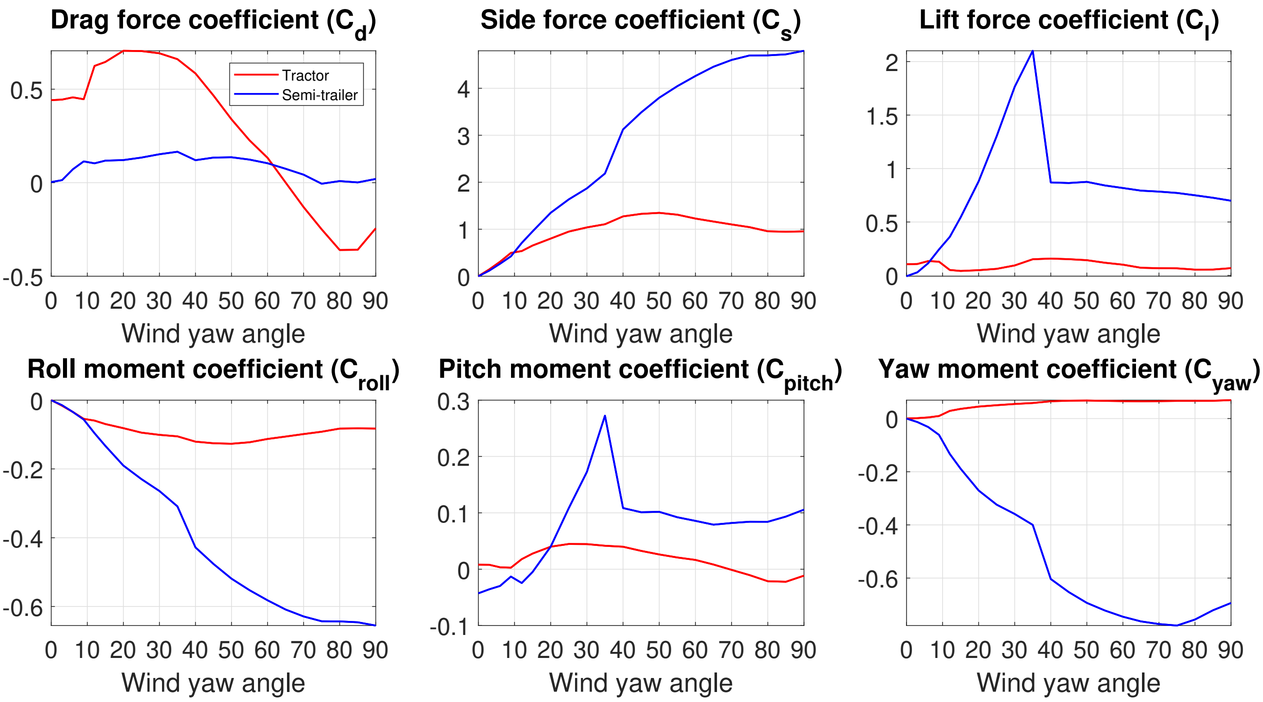

Figure 4.8: *Aerodynamic Coefficients*

5 METHODS

5.1 Input data: W6 Weather condition

5.1.1 Bridge motion

Floating bridges were modelled as finite element models in *Orcaflex* software for dynamic analysis and *Sofistik* for static analyses (Vegvesen, 2017) [9]. The time series data of bridge response to hydrodynamic loads and wind loads were obtained by simulation in Orcaflex software. Bridge motions subjected to environmental loads (wind and waves for 1-year storm conditions) were simulated for a duration of one hour (3600s).

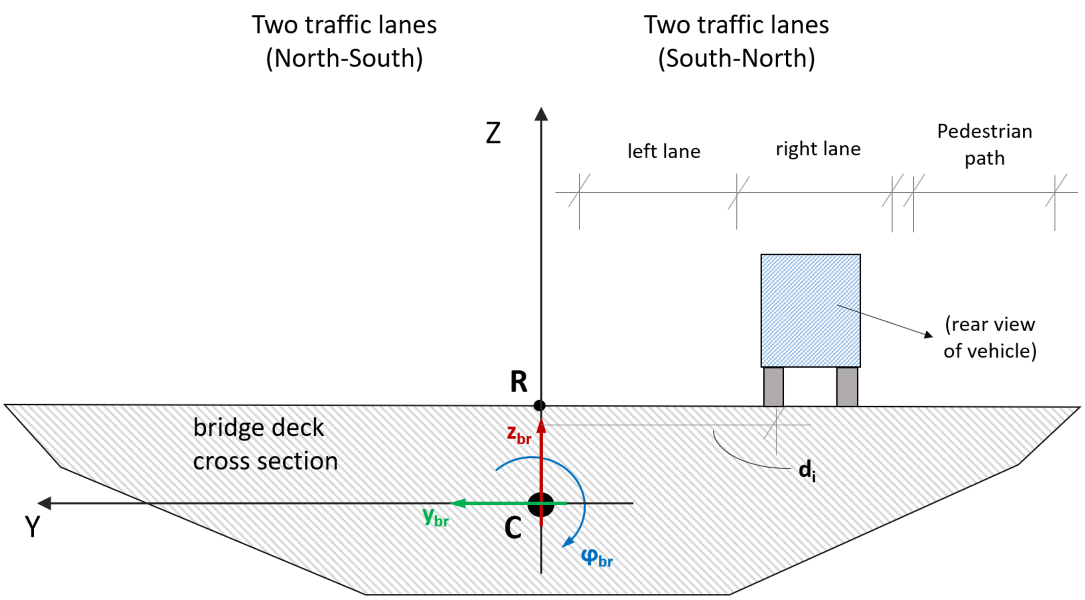

Figure 5.1: *Bridge deck cross-section*

Vertical (z_{br}), lateral (y_{br}) and torsional (φ_{br}) displacements of the bridge deck centre (point C, Figure 5.1) were acquired at specific points along the length of the bridge (at every 5m or 8m depending on the definition of the bridge nodes' in the Orcaflex software). This data was then interpolated to every 1m along the length of the bridge at a sampling rate of 5Hz. Figure 5.2 presents the vertical bridge displacement data at select points (at 0.5 km; 2 km; 5 km) as a function of simulation time along the length of the bridge.

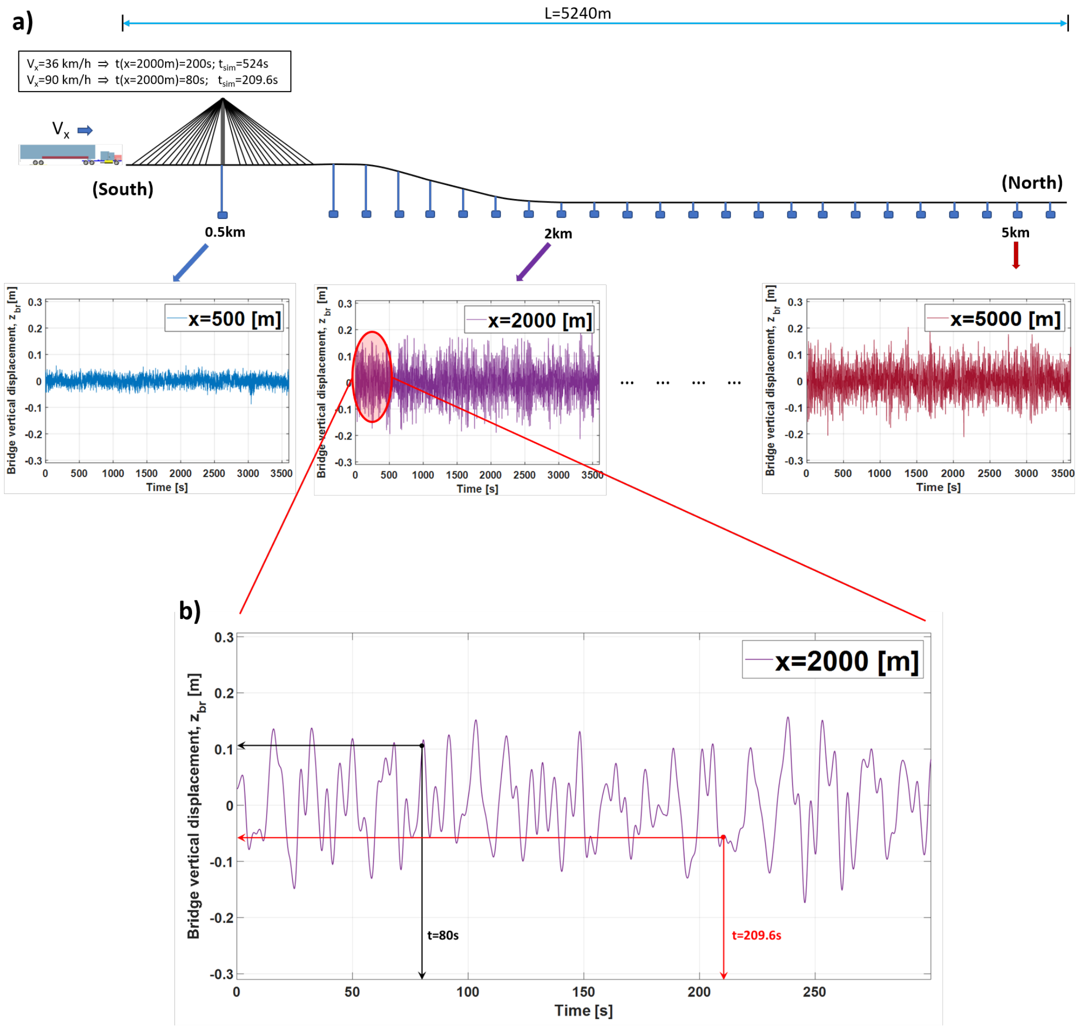

Figure 5.2: *Vertical bridge displacement a) at distance of 0.5km, 2km, 5km; b) close-up view at distance of 2km*

5.1.2 Wind data

The wind gusts on the Bjørnafjorden bridge blows from the west to the east. In this master thesis the tractor semitrailer vehicle is considered to travel from Kristiansand to Trondheim, thereby the wind gusts are imposed on the left of the vehicle.

The wind data is obtained via stochastic simulations on *Windsim* software. For this master thesis, one year storm condition (henceforth referred as W6 weather condition) is considered. The wind data is comprised of wind velocity components ($V_{x,wind}$, $V_{y,wind}$ and $V_{z,wind}$) of NPRA coordinate system as shown in figure 5.3. The data virtually measured for one hour, as described in section 5.1.1. The wind excitation on the tractor semitrailer vehicle starting at a time instance (as mentioned in figure 5.8) and travelling at 36km/h and 90km/h are illustrated in figure 5.4. It is observed from figure 5.4 that the magnitudes of wind excitation in vertical direction ($V_{z,wind}$) is insignificant as compared to the longitudinal ($V_{x,wind}$) and lateral ($V_{y,wind}$) wind excitation components. Therefore, the vertical wind excitation are neglected in this thesis. The longitudinal and lateral wind velocities are higher for the first 1.5km distance as compared to the remainder of the bridge distance. This is due to the higher wind velocities that the vehicle will experience at a higher altitude on the bridge deck at the south end [9]. The PSD of wind excitation for the vehicle travelling at 36km/h and 90km/h is illustrated in figure 5.5. It is observed that these excitation are of frequency around 0.01Hz

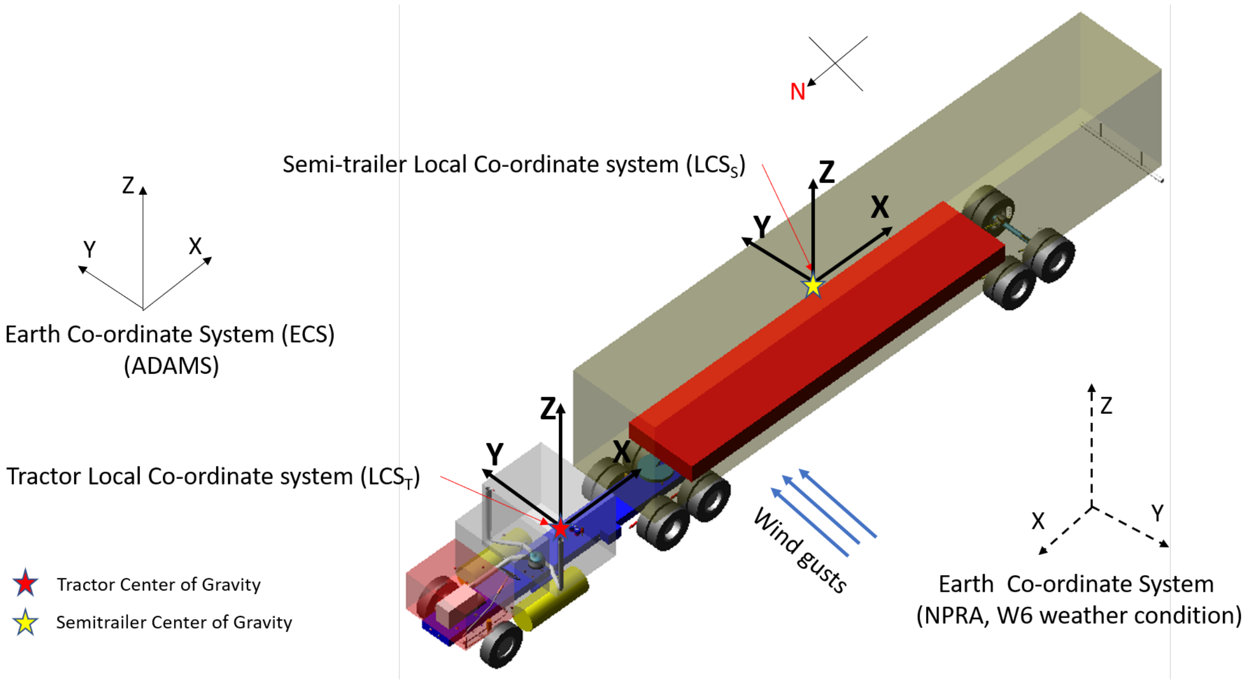

Figure 5.3: *Coordinate system*

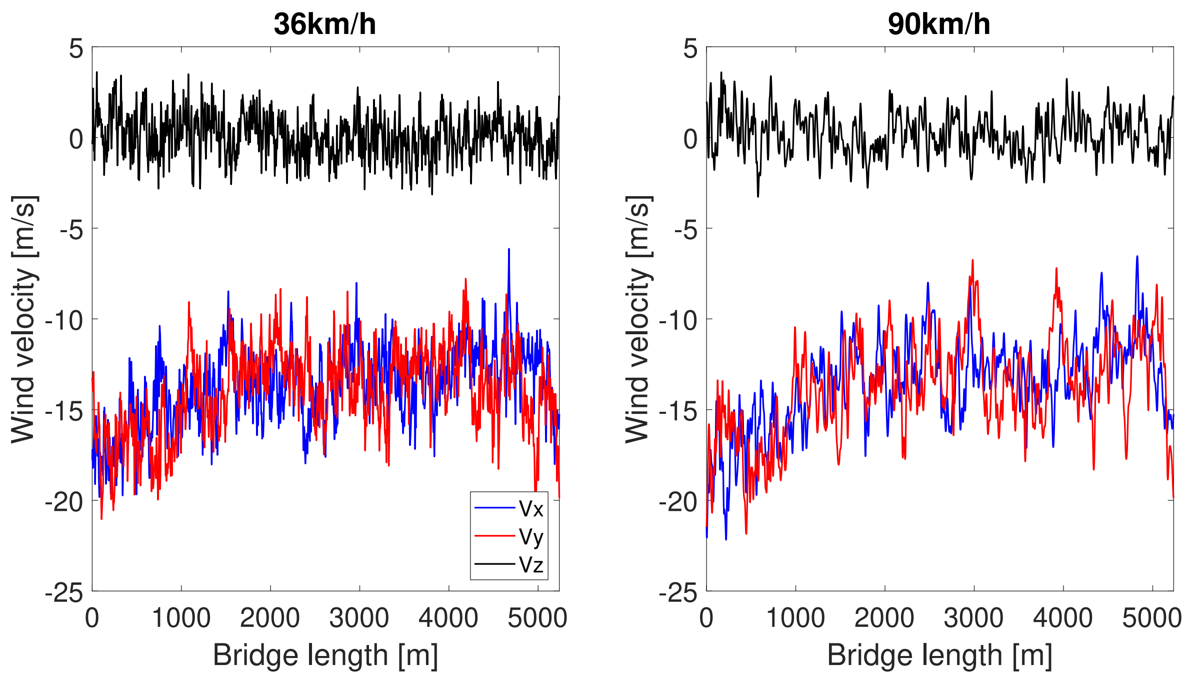

Figure 5.4: *Wind excitation velocity*

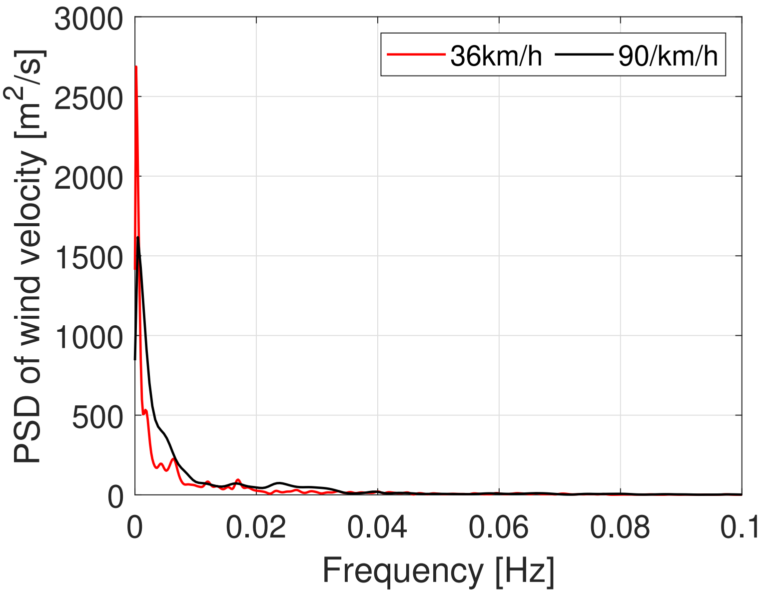

Figure 5.5: *PSD - Wind velocity from Fig.5.4*

5.2 Vehicle input: Data pre-processing

Vehicle input data set were derived and defined from the bridge motion data. Vehicle input signals is a function of time and of the vehicle's location along the length of the bridge. Consequently, vehicle inputs will differ based on vehicle speed as seen in Figure 5.2 (b). It was discovered that the wind velocity components, particularly the cross-wind component, have considerable impact on the lateral deviation of a heavy vehicle from the desired path on the floating bridge [17]. Therefore, from the vehicle input dataset, the input corresponding to the highest RMS value of the cross-wind component $V_{y,wind}$ were extracted.

The description of the vehicle input data set is elaborated further. The simulation time in this investigation refers to the traversal time of the vehicle across the floating bridge which is less than the simulation time of the bridge motion. To illustrate, the simulation time of the bridge motion is 3600s, whereas the simulation time for a vehicle speed of 36km/h is 524s. Bridge motion data simulated in *Orcaflex* was recorded at a sampling interval of 0.2s. For the vehicle speed of 36 km/h, there exists N different vehicle inputs:

$$N = \left(\frac{t_{sim,br} - t_{sim,v}}{\Delta t}\right) = \left(\frac{3600 - 524}{0.2}\right) = 15380 \tag{5.1}$$

where $t_{sim,br}$ is the simulation time of the bridge motion; $t_{sim,v}$ is the simulation time of the vehicle to cross the bridge; Δt is the sampling time for the acquired bridge motion data. This means, there exists 15380 data inputs depending on at what time out of the 3600 s the vehicle commences the journey (Figure 5.6).

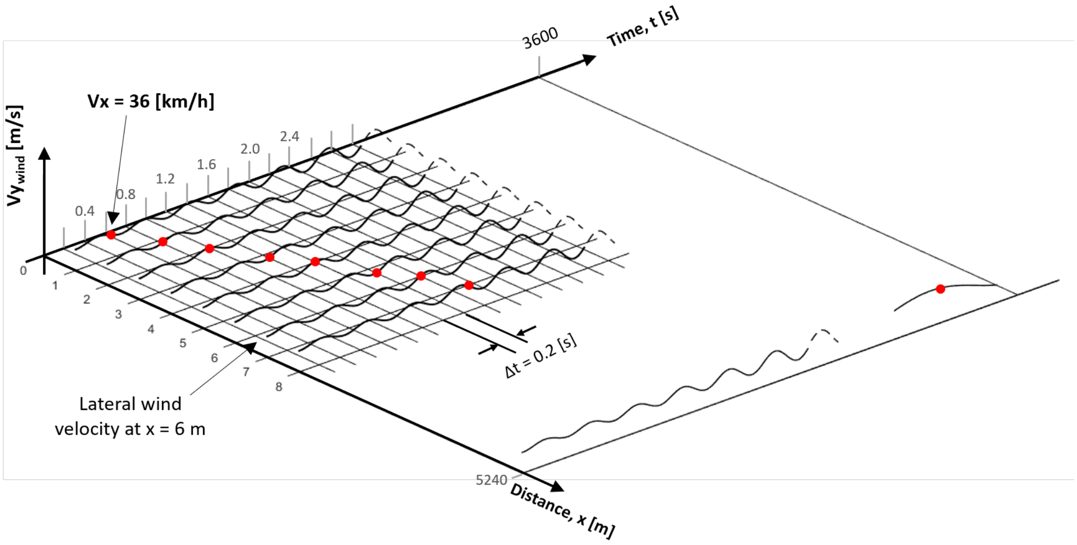

Figure 5.6: *Space-time data representation: Crosswind Vy_{wind} as a function of time and distance; and the vehicle input data set for a vehicle speed of 36 km/h*

Similarly, for a vehicle speed of 54 km/h, the number of vehicle inputs is:

$$N = \left(\frac{t_{sim,br} - t_{sim,v}}{\Delta t}\right) = \left(\frac{3600 - 349.3}{0.2}\right) = 16254 \tag{5.2}$$

The RMS of the cross-wind component Vy_{wind} for the vehicle speed of 36 km/h are computed for all the N=15380 data inputs and the data set with the greatest RMS is identified as illustrated in Figure 5.7. Similarly, the greatest RMS of the data set for different vehicle speeds and their corresponding data inputs are identified as seen in Figure 5.8 and Table 5.1.

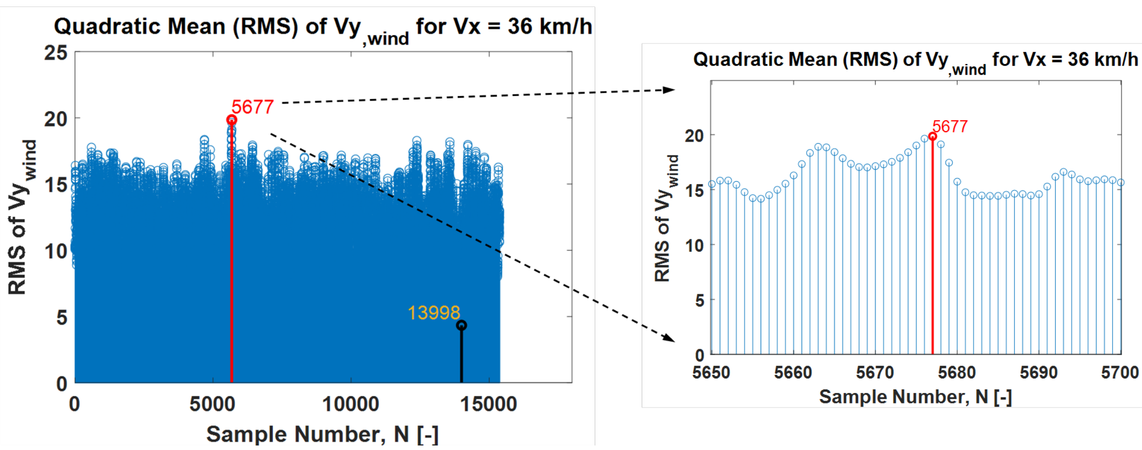

Figure 5.7: *RMS value of crosswind component of all vehicle input data set for a vehicle speed of 36 km/h, and the identified dataset with the highest RMS value*

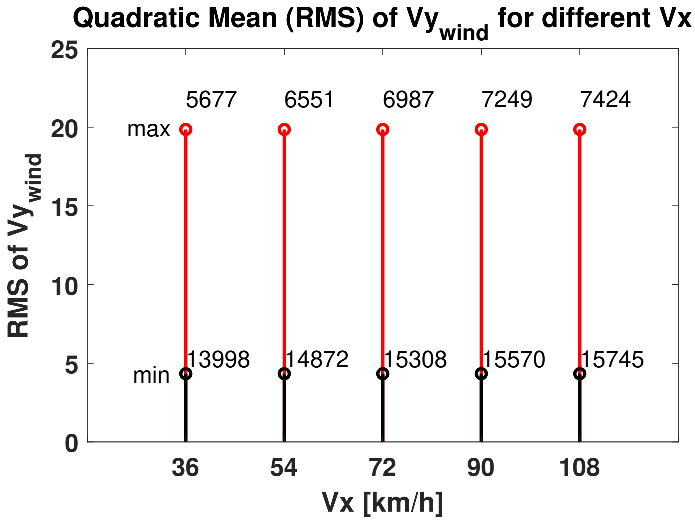

Figure 5.8: *Greatest RMS value of crosswind component identified from all vehicle input data set for different vehicle speeds*

Vehicle velocity [km/h]	Highest RMS value [-]	Time stamp in W6 data [s]
36	5677	1135.2
54	6551	1310.0
72	6987	1397.2
90	7249	1449.6
108	7424	1484.6

Table 5.1: Time stamps in the W6 weather data corresponding to the highest RMS value

5.3 Vehicle model excitation: Bridge Motion

5.3.1 Data Processing: Bridge Motion

The time corresponding to the identified greatest RMS indices are the start of every excitation signal for the first axle of the tractor semitrailer at the 0m mark of the bridge. The subsequent axles will cross the 0m mark with a certain time delay depending on the speed of the vehicle and the corresponding wheelbase. Thus, the excitation for every axle is offset with a certain time delay from that of the first axle.

Figure 5.9 schematically shows bridge vertical displacement in function of time and distance. Here, an example of the bridge vertical displacements as vehicle inputs for the first and second axle for a vehicle speed of 36 km/h have been illustrated. Lateral and roll displacements of the bridge together with the wind components for the vehicle input data set were determined in a similar fashion.

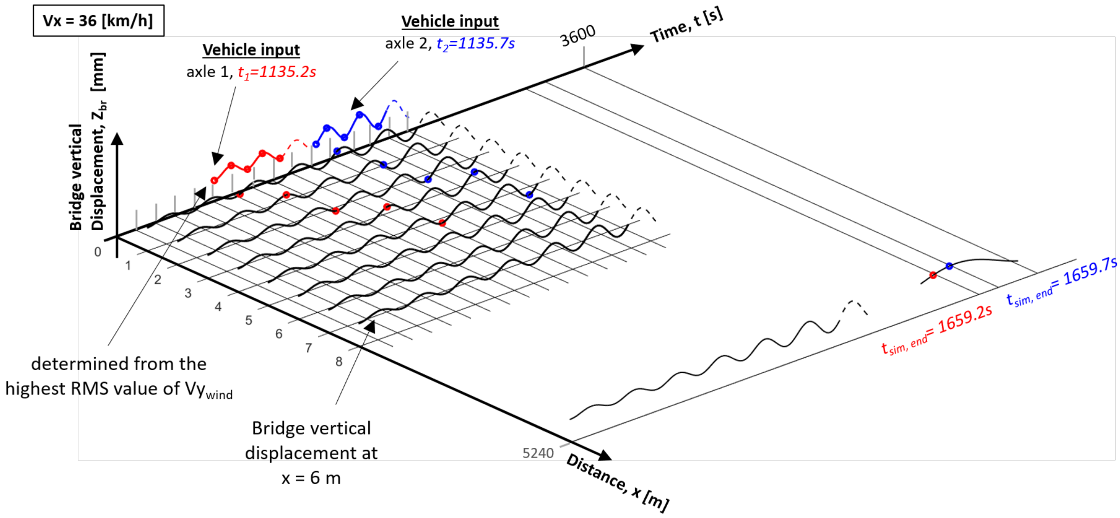

Figure 5.9: *Space-time data representation: Bridge vertical displacement as a function of time and distance, and bridge vertical displacements for the vehicle input data set for a vehicle speed of 36 km/h*

The lateral bridge motion signals at the first axle for different vehicle speeds are depicted in Figure 5.10. The range of lateral bridge motion lies between $\pm 1.0m$. The size of the vehicle input data is clearly noticed to be different for different vehicle speeds.

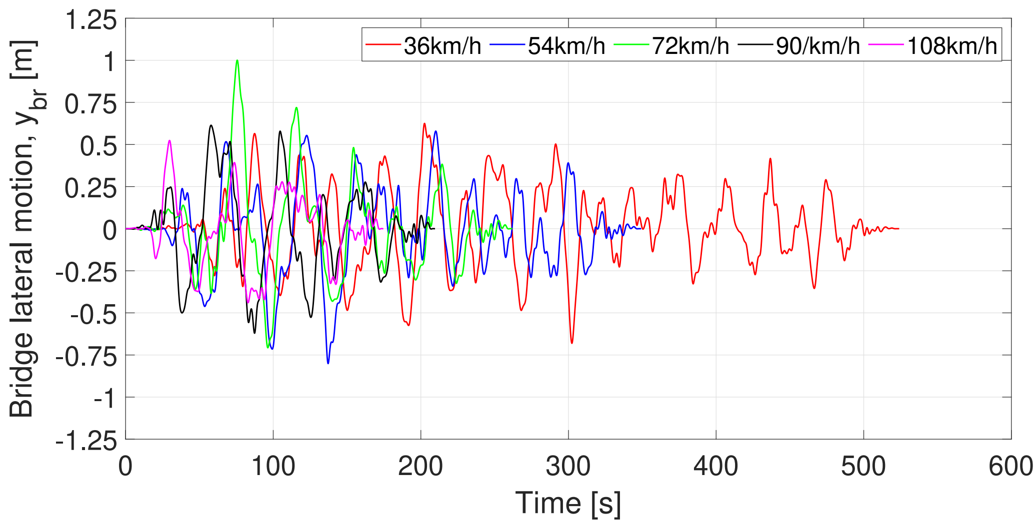

Figure 5.10: *Bridge lateral motion of the first axle of the vehicle as a function of time for different vehicle speeds*

For the vehicle speed of 54 km/h, the bridge lateral motion for all the axles are illustrated in Figure 5.11. It can be seen that the excitation signals for every axle is different and has a time delay.

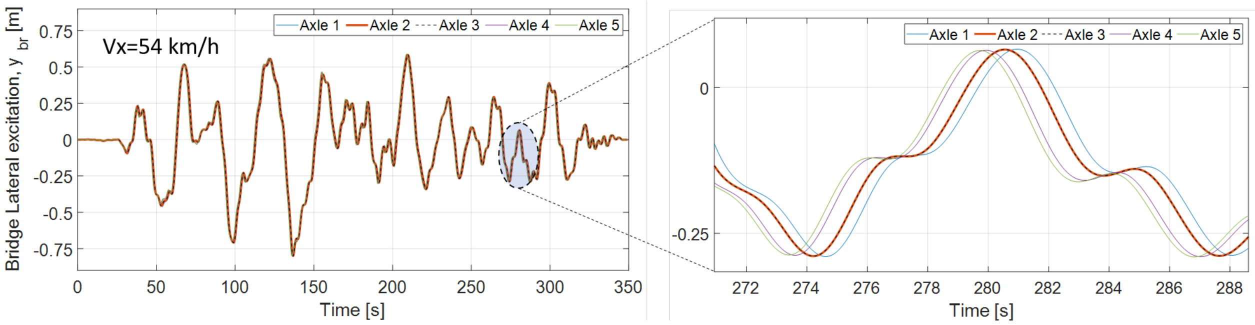

Figure 5.11: *Bridge lateral motion of all axles for the vehicle speed of 54 km/h*

The appropriate lateral bridge motion was also extracted as input to the driver model.

Similarly, the bridge vertical motion (z_{br}) and roll motion (φ_{br}) are depicted in Figure 5.12 and Figure 5.13 respectively. The excitation of the vertical bridge motion (z_{br}) range predominantly between $\pm 0.2m$, while the roll motion (φ_{br}) ranges between $\pm 0.25deg$.

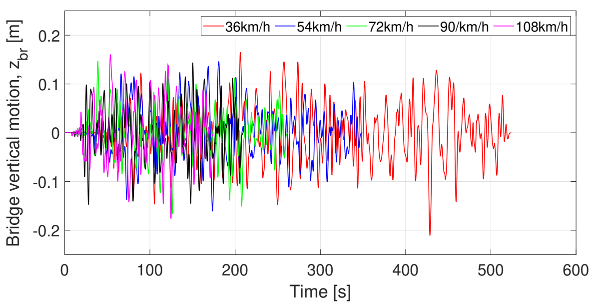

Figure 5.12: *Vertical bridge motion of the first axle of the vehicle for different vehicle speeds*

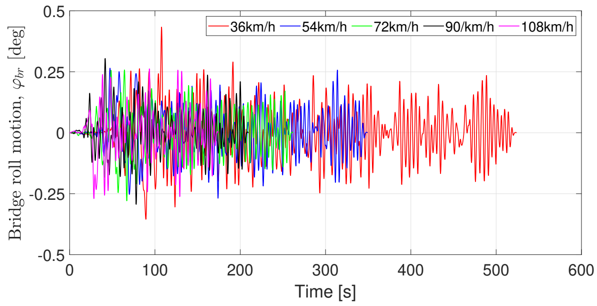

Figure 5.13: *Bridge roll motion of the first axle of the vehicle for different vehicle speeds*

The extracted vertical (z_{br}) and roll (φ_{br}) bridge displacements were used to define vertical excitation (ζ) for the left and right wheel tracks of the tractor semitrailer model for every axle with the following relation:

$$\zeta_{ti} = z_{br} + \zeta_{rr} + d_i \varphi_{br} + h_{br} \quad (i = left, right) \tag{5.3}$$

where d_i is the lateral distance from the rotational centre on the bridge deck (point C, Figure 5.1) and the contact point between the tractor semitrailer's wheel on the road (Figure 5.1); φ_{br} is the roll motion of the bridge deck; z_{br} is the vertical excitation of the bridge deck; ζ_{rr} is the road roughness; h_{br} is the elevation profile of the bridge. The effect of the roll motion is amplified at the location farther away from the rotational centre (point C) and therefore the vehicle running on the right traffic lane is considered.

A road roughness equivalent to *very good* condition for a newly constructed bridge was considered. The power spectral density (PSD) for a road class 'A' defined in ISO8608 standard [28] was used to model road roughness (Figure 5.14). A random road profile can be represented by an infinite sum of harmonic functions of different amplitudes, circular frequencies and phase angles, according to Shinozuka (1972) [40]. Further details regarding road modelling process can be found in (Sekulic, 2018; Sekulic, 2013) [37] [38]. The road roughness is modelled to the length of the Bjørnafjorden floating bridge (5240m). Figure 5.14 presents the modelled road roughness as a function of distance. The magnitude of roughness are dispersed mainly within $\pm 0.01m$. Figure 5.15 depicts the road roughness in the frequency domain considering the ISO8608 standard [28].

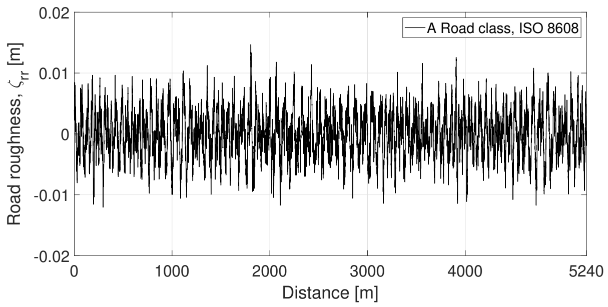

Figure 5.14: *Road roughness of road class 'A' generated from ISO8608 standard*

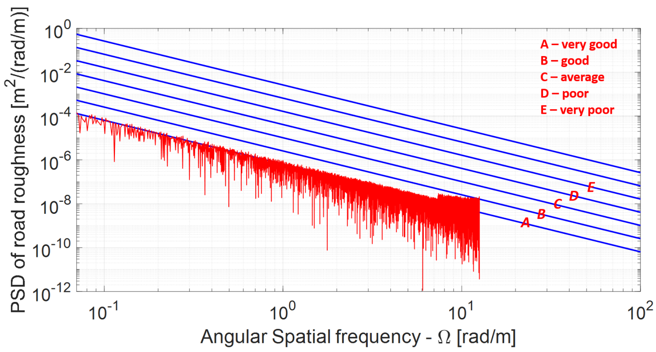

Figure 5.15: *PSD of road roughness for road class A according to the ISO8608 standard*

Furthermore, these bridge excitation are superimposed with the elevation profile of the Bjornafjorden bridge. The height of the bridge at the south end is about 64 m and drops about 48 m to around 16 m above mean sea level within the first 2 km as seen in Figure 5.16.

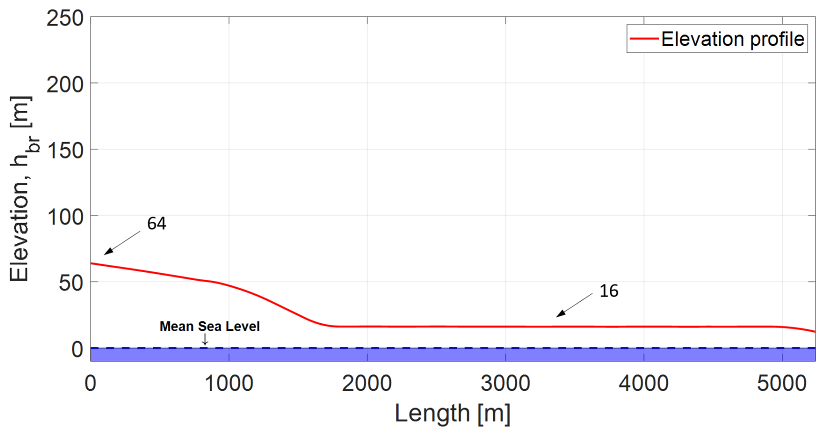

Figure 5.16: *Elevation profile of the Bjornafjorden floating bridge*

The vertical excitation for the right and left wheels of the first axle for the tractor semitrailer with a speed of 90 km/h is depicted in the figure 5.17 (a) along the length of the bridge.

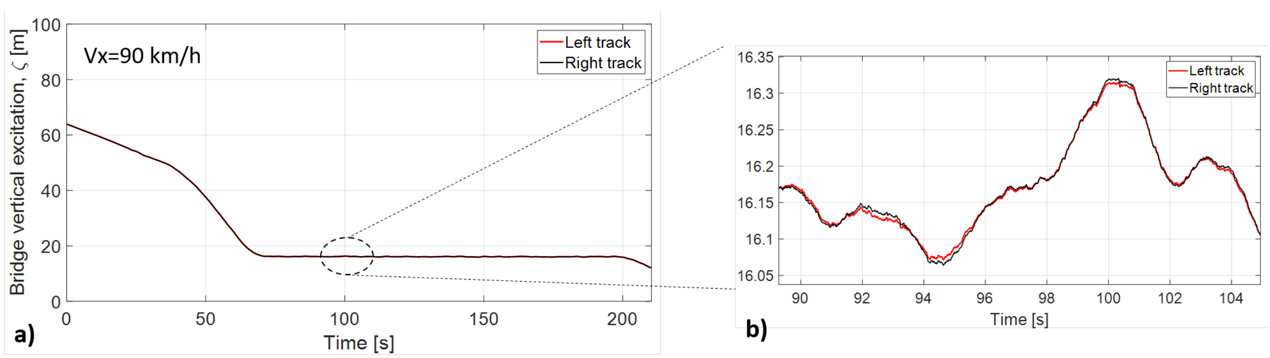

Figure 5.17: *Vehicle input a) vertical excitation for the left/right track on the right lane (Figure 5.1); b) magnified view of the left/right track signals for a vehicle speed of 90km/h*

The larger undulation on the Figure (5.17 (b)) is due to the vertical motion (z_{br}) of the bridge, while the smaller undulations are a result of the road roughness (ζ_{rr}). The difference seen in the two signals are a consequence of the roll motion (φ_{br}) of the bridge.

Note that to account for the simulation time, the bridge excitation starts when the first axle of the tractor semitrailer crosses the 0m mark of the bridge. The remaining axles are subsequently exposed to the excitation with a time delay depending on vehicle speed. Similarly, the simulation stops only when the last axle of the tractor semitrailer crosses the bridge 5240m mark of the bridge. The axle data are consequently prefixed and suffixed with no excitation signals for a given vehicle speed as seen in the Figure 5.18:

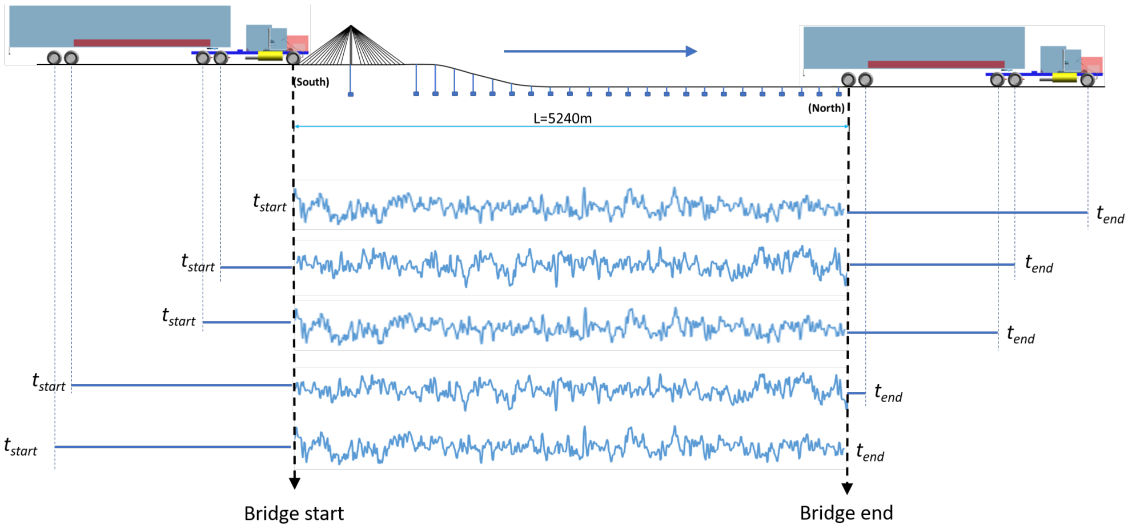

Figure 5.18: *Vehicle input data adjusted to suit simulation time t*

5.3.2 Bridge motion construction

MSC.ADAMS has a road builder option that allows user to build road profiles with desired properties. Besides the road coordinates that can take values of x,y and z to build the road, road properties such as road roughness, curbs, ramp, embankment, road width and road friction, to name a few, can be included to mimic real road properties. It was understood that the abundantly available options apply for a non-moving road; roads that we have been driving on in the real world. It was then decided to explore first attempts in coming up with ideas to construct a 'moving ground' that can accept bridge motion signals. A couple of ideas were explored within the MSC.ADAMS/View module.

Discrete 3-DoF road panes

The first idea to emulate a floating bridge, was to construct the whole bridge with discretized road panes. Each of the discretized road panes was then be suitably supported and constructed with translation and hinge joints. This would enable the bridge motion on which the vehicle can ply on to investigate vehicle dynamics.

Each road pane was built with length of 1 metre (Figure 5.19). The road pane (green) was supported with mass-spring-dampers at every corner, which rested on a base plate (blue). These mass-spring-dampers could then accept vertical excitation signals. The base plate was fixed to an auxiliary part at the center through a hinge joint that would allow the roll motion of the bridge. The auxiliary part was fixed to the ground through a translation joint that can accept lateral bridge motion signals. Thus, a single discretized road pane was able to take in all three primary bridge motions of interest namely the vertical, roll and lateral bridge motion as seen in Figure 5.19. This forms one road pane assembly.

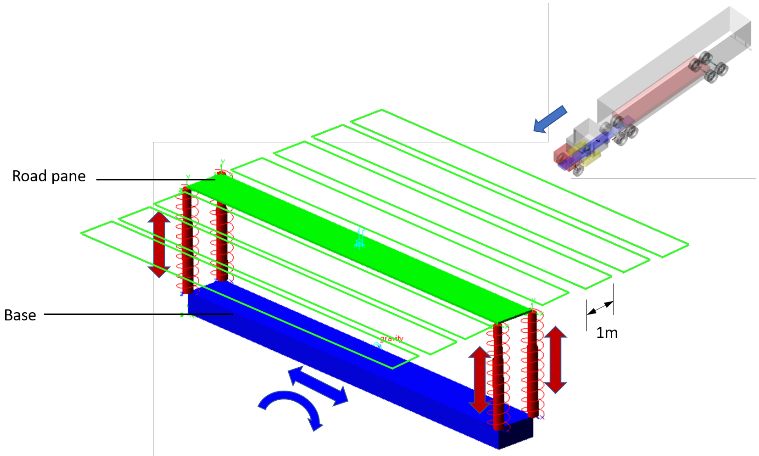

Figure 5.19: *Discrete 3-DoF road panes modelled in MSC.ADAMS/view*

However, the drawbacks of this idea was soon apparent. This approach was effort-intensive with 5240 such road pane assemblies to be built, and to feed in the correct signals into every joint. Furthermore, with different signals fed into each road pane, there will exist discontinuities between every adjacent road panes that will result in the vehicle experiencing a stair-case effect as the tires roll over every transition between two road panes.

Nonetheless, this experience provided a better understanding of handling the bridge motion data.

Chassis dynamometer inspired test rig

Another idea that brew from the limitations of the first approach was inspired from a chassis dynamometer test rig. The test vehicle is parked on a chassis dynamometer with its drive wheels on the rollers (Fig. 5.20, Fig. 5.21). This means that the forces acting on the vehicle such as the vehicle's moment of inertia, rolling resistance and aerodynamic drag must be simulated so that the trip on the test bench reproduces emissions comparable to those obtained during an on-road trip. For this purpose, asynchronous machines or direct-current machines generate a suitable speed-dependent load that acts on the rollers for the vehicle to overcome. More modern machines use electric flywheel simulation to reproduce this inertia. A blower mounted in front of the vehicle provides the necessary engine cooling [11].

Figure 5.20: *Multi-axle chassis dynamometer [49]*

Figure 5.21: *Multi-axle chassis dynamometer wtih vehicle [49]*

Inspired by this test rig, a roller test rig was constructed in MSC.ADAMS/View interface with a spindle. The diameter of the roller was large enough to ensure sufficient flatness at the tire-roller contact area as seen in Figure 5.22. Different joints between the roller, spindle and the ground allowed for all three bridge motion signals of interest to be accepted. The roller itself could rotate about the spindle axis to simulate the vehicle running on the road.

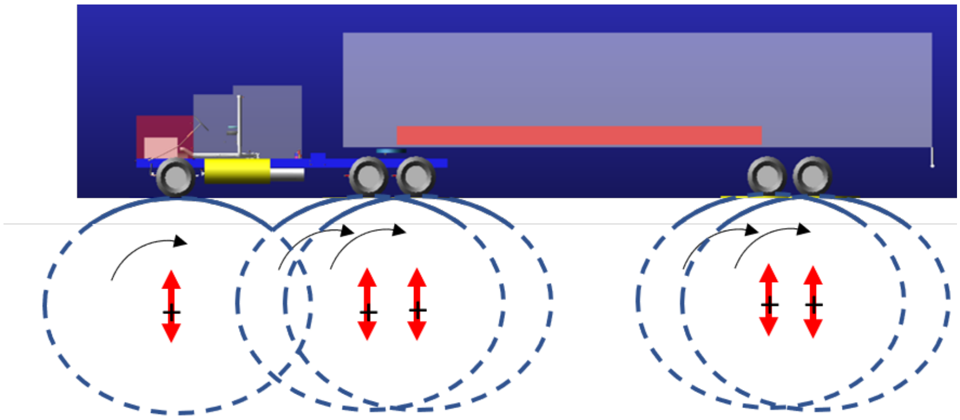

Figure 5.22: *Chassis dynamometer inspired test rig constructed in MSC.ADAMS/view*

The chassis dynamometer inspired test rig proved advantageous over all the drawbacks of the earlier method with discrete road panes. It was later understood that exporting models from MSC.ADAMS/View into MSC.ADAMS/Car would not be efficient. Looking within the MSC.ADAMS/Car interface and making use of the template builder would be the way forward.

xPost rig

The xPost rig is inspired from a 2-post/4-post test rig that is already available in the MSC.ADAMS/Car [12] [13] [14] module. A dynamic analysis in the suspension test rig actuates the suspension at the tire contact patch on the tire pad via user defined runtime function expressions or by referencing existing RPC3 files. The testrig's vertical actuators can be driven with forces, displacements, velocities, or accelerations. One can also specify wheel forces (for example, cornering force, overturning moment and so on) as functions of time using function expressions or by referencing existing RPC3 files.

Different analyses such as parallel and opposite wheel travel, and single wheel travel with the built-in test rig template indicate possibility of incorporating with the vertical excitation for each wheel in an axle.

Learning the details of construction of the built-in suspension test rig in MSC.ADAMS/Car [12] [13] [14], a 'moving ground' test rig was built in the template builder within the MSC.ADAMS/Car interface as illustrated in the figure 5.23. The moving ground test rig consists of a tire piston and cylinder assembly with a translation joint (red, Fig. 5.24) for either wheels of an axle according to the track width of the vehicle. A tire pad (yellow) atop the piston serves to allow the vehicle's wheel to rest on the test rig. The tire pad and the piston are locked through a fixed joint. Additionally, the entire piston-cylinder-tirepad assembly is assembled with a base through two translation joints (green, Fig. 5.24). This base is locked to the ground via a fixed joint and does not move.

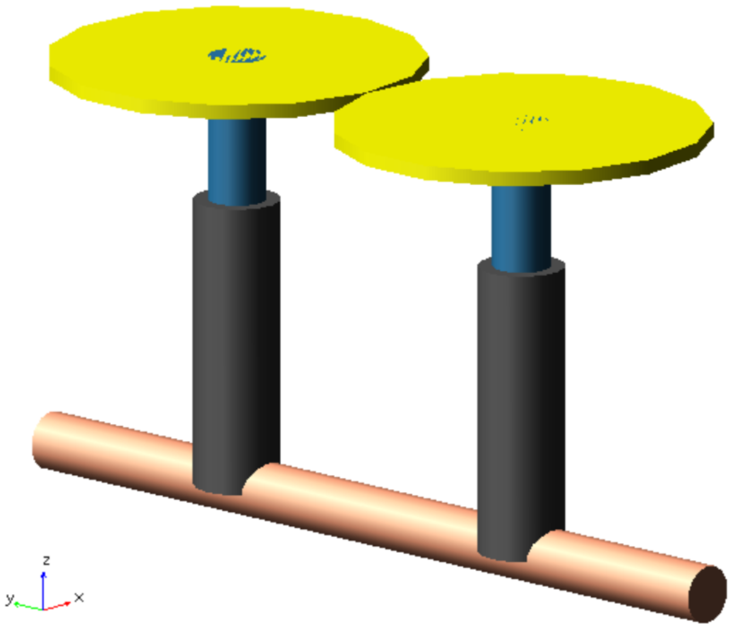

Figure 5.23: *Moving ground test rig*

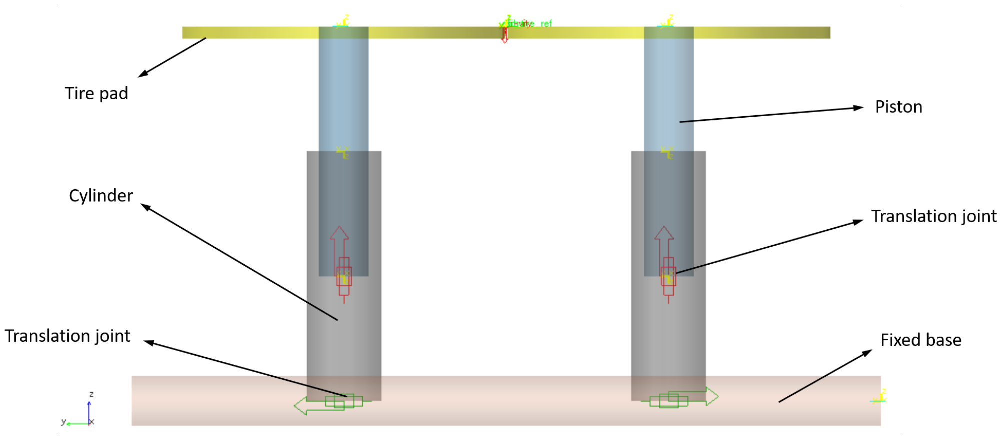

Figure 5.24: *Moving ground test rig - translation joints*

The effective bridge vertical excitation signals (ζ) (bridge motion containing the heave and roll, road roughness, and bridge elevation) are fed through the translation joint (red, figure 5.24) between the piston and cylinder for each wheel track, while the lateral bridge motion (y_{br}) are fed to the translation joint between the piston-cylinder-tirepad assembly and the fixed base (green, Figure 5.24).

It must be noted that the template builder in MSC.ADAMS/Car by default creates symmetrically mirrored bodies along the X-Z plane during modelling. As a result, the imposed motion to translation joints (green, in Figure 5.24) between the cylinder and the fixed base are modelled in opposite directions by default. Care must taken to flip the sign (Figure 5.25) of the lateral bridge motion signal for the left translation joint to suit MSC.ADAMS coordinate system so that both these translation joints move in tandem relative to the fixed base.

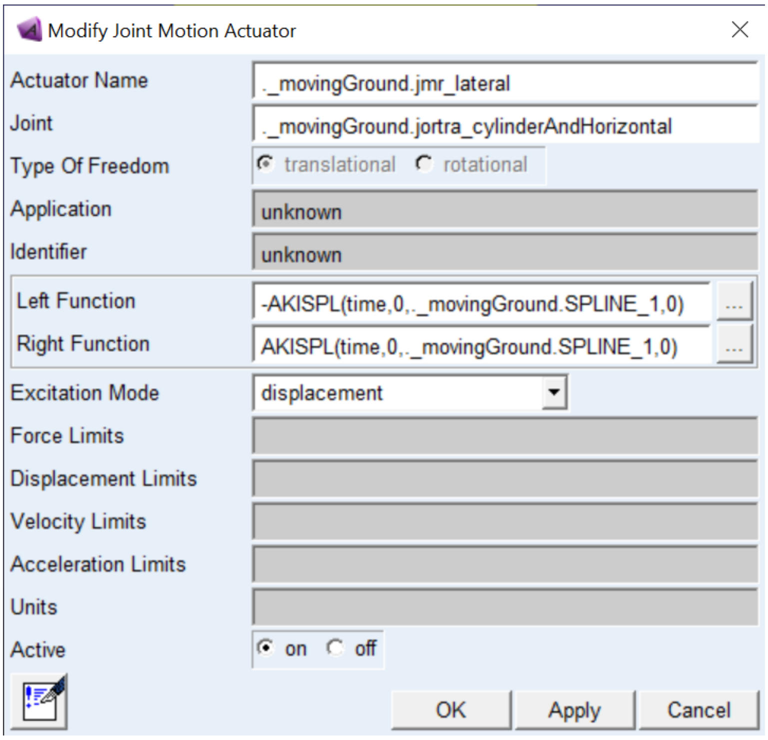

Figure 5.25: *Bridge lateral motion for the translation joints (green, Figure 5.24)*

Copies of this moving ground test rig to suit the number of axles in a vehicle allows for creation of a test rig for each axle, thus the term xPost rig. The excitation signals that exist as a function of time are carefully loaded to each translation joint in the template builder as shown in Figure 5.26 through the AKISPL built-in function (Figure 5.25) before every test rig template is finally saved.

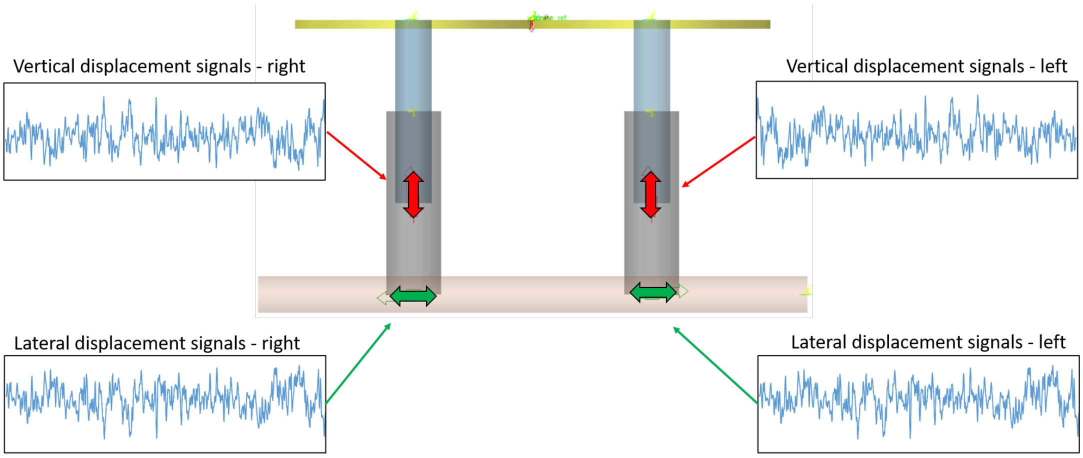

Figure 5.26: *Vehicle input signals from the bridge motion imposed at translation joints*

Subsequently, a sub-system for each of the moving ground templates are built under the environment category. The test rigs are suitably offset in the longitudinal and vertical direction to match the wheel base of every axle. This ensures that every test rig is correctly assembled with each axle positioned exactly at the contact path on either tracks during assembly with the vehicle model. Five moving ground test-rig sub-systems are saved. These sub-systems are then assembled to the tractor semitrailer vehicle model as seen in figures 5.27, 5.28 and 5.29.

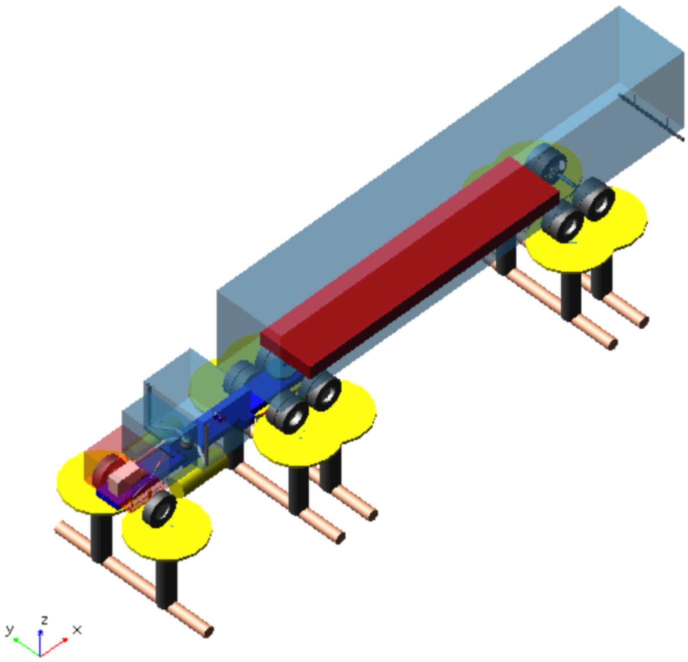

Figure 5.27: *xPostrig assembly with the tractor semitrailer*

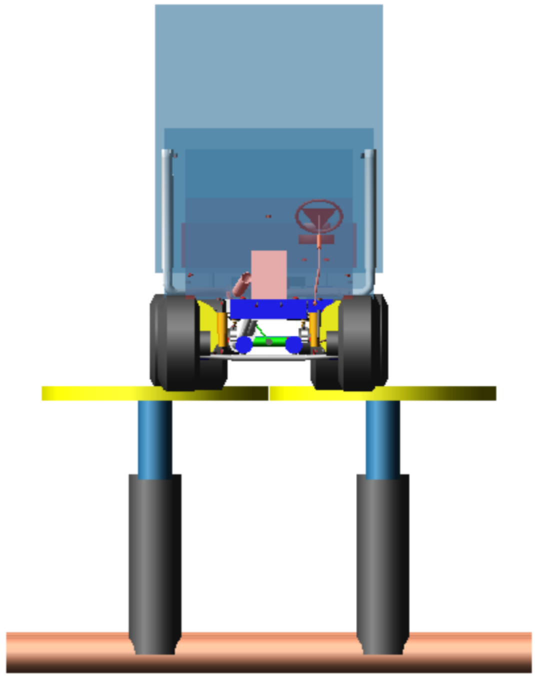

Figure 5.28: *xPostrig assembly - front view*

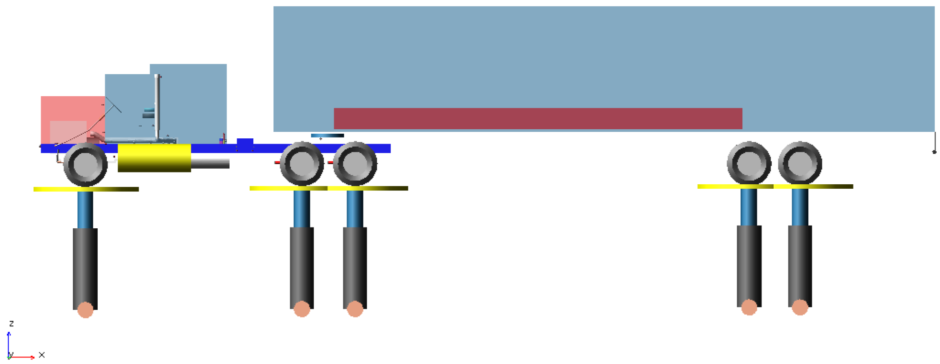

Figure 5.29: *xPostrig Assembly - right view*

While the suspension analysis test rig is typically used for sub-system tests and dynamics analyses where the vehicle is not in motion ($v_x = 0$), the investigation in this master thesis requires the vehicle to be in motion on a road so that aerodynamic forces may be induced, thus allowing us to analyze aspects related to the vehicle dynamics.

There exists a relation between the tire contact patch marker on the vehicle and a corresponding reference marker on the ground part (road surface), which allows the vehicle to transfer forces on to the ground (reaction part). In order to simulate moving ground, the definition of this relation is to be changed. This is enabled through a macro file read in MSC.ADAMS/Car Truck that transfers the relation between the ground reference marker and the tire pad reference marker on the xPost test rig. Consequently, the bridge motion can be induced to emulate the motion of a floating bridge while the vehicle is in motion.

Thus, a method has been established to accommodate and simulate a moving ground for applications involving a floating bridge. The construction of the xPost rig template can be tailored to suit conventional single unit vehicles with two axles such as a passenger car, bus, and trucks, to multi-unit and long combination vehicles such as a tractor semitrailer, A-double, B-double and Nordic combination. Furthermore, the method presented here could be used for different type of the bridges such as suspension bridge, etc for future work.

5.4 Vehicle model excitation: Aerodynamic loads

The wind as per the W6 weather condition, blows from west to east (left of vehicle). The wind excitation (NPRA Co-ordinate system) can be decomposed into 3 forces and 3 moments along the local coordinate system (MSC.ADAMS/Car) of each unit as illustrated in figure 5.30. These excitation are imposed on to one point each on the tractor and semitrailer unit, since the vehicle is articulated. This section deals with the details of dynamically computing these components.

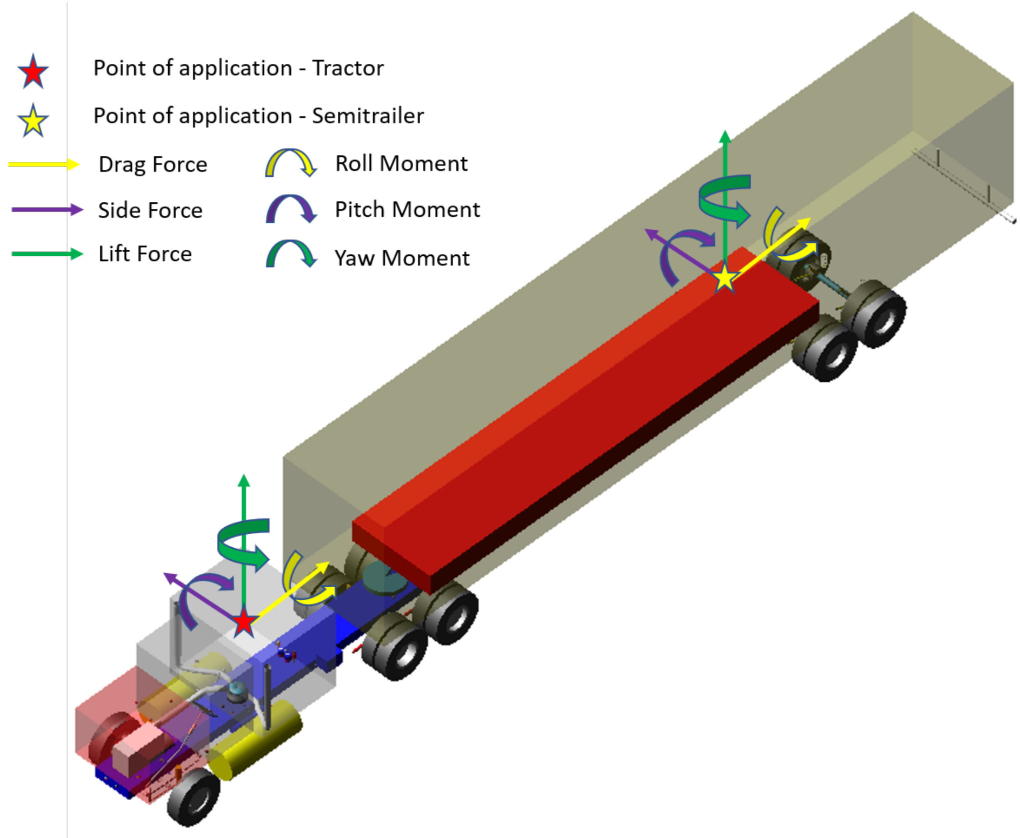

Figure 5.30: *Aerodynamic loads on the Tractor Semitrailer*

5.4.1 GFORCE

GFORCE is an ADAMS function which enables the application of forces ($F_{x,wind}$, $F_{y,wind}$ and $F_{z,wind}$) and moments ($M_{x,wind}$, $M_{y,wind}$ and $M_{z,wind}$) along the X, Y and Z direction of a coordinate system, at a desired location. The GUI shown in the figure 5.31 is an example of GFORCE applied on the semitrailer. ADAMS variables are created for each of the forces and moments. A reference location for the application of the 3 forces and 3 moments also needs to be considered, details of which is further described in section 5.4.2. The orientation of these forces is considered to be the same as that of the reference coordinate system. The action part is the body on which the GFORCE will be acted upon, in this case, the trailer body. Reaction part is where the effects of the applied GFORCE is perceived, the ground. Similarly, the GFORCE is constructed for the tractor unit.

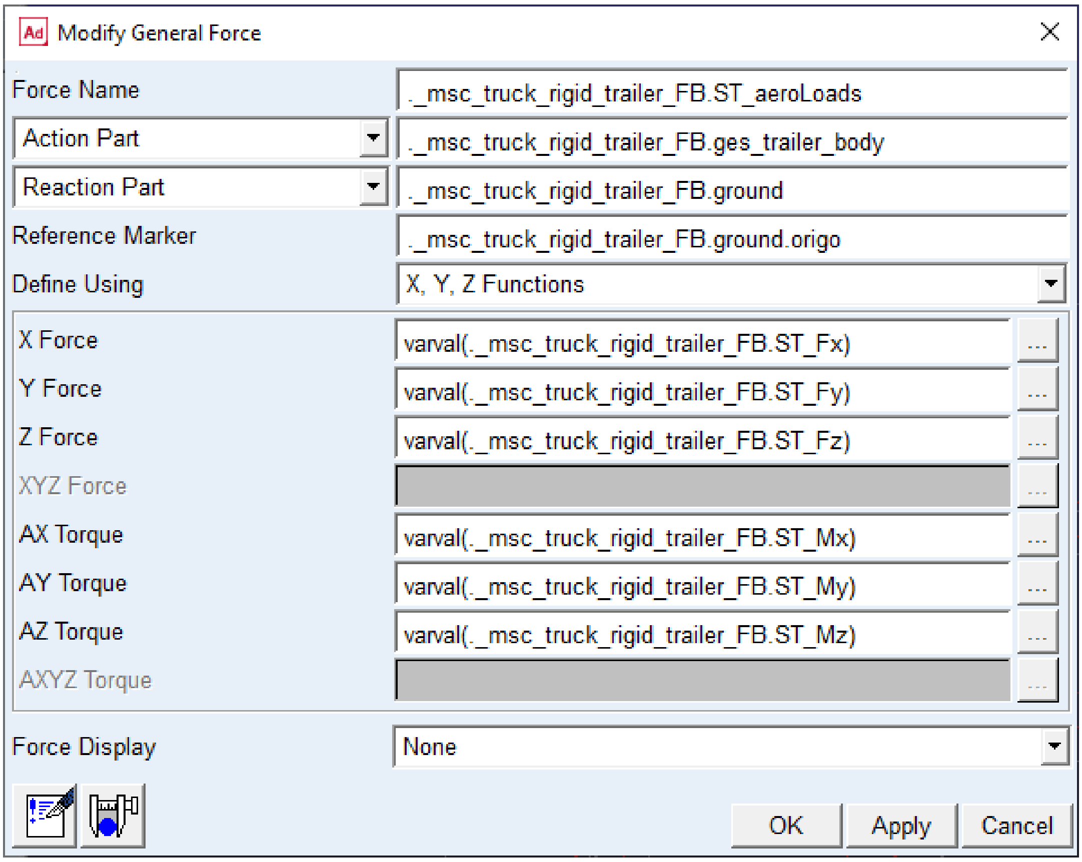

Figure 5.31: *GFORCE GUI*

5.4.2 Locations of application

Method 1

The literature review concluded that the research done so far uses the position of CoP for application of aerodynamic loads on the high-fidelity ADAMS Car/Truck model (Abdulwahab, 2018) [2]. This approach of aerodynamic load applied the CoP of each unit was initially followed in this master thesis. It was discovered that this method has the following drawbacks:

- ADAMS specific wind file needed to be created
- The change in aerodynamic force and moment coefficients as a result of varying wind yaw angle would have to be neglected
- Instantaneous yaw of the vehicle unit would be neglected

In addition to this, the position of CoP would change dynamically based on the wind yaw angle and the vehicle orientations. The approach as described by Sekulic et al (2021) [9], would overcome these drawbacks.

Method 2

The aerodynamic loads will be applied to each unit at its respective CoG as shown in figure 5.32. The CoG position of the vehicle units varies slightly with dynamic changes to the vehicle and can be neglected. The advantage of this approach being, the aerodynamic loads can be dynamically computed, considering the vehicle orientation [9]. This approach is relative simple and robust.

As a result, the aerodynamic force and moment coefficients are transformed (described in detail in section 5.4.4) from the aerodynamic reference points (yellow stars) to the CoG of each vehicle unit (red stars) as illustrated in figure 5.32. The (X,Y,Z) co-ordinates of the CoG of indisivual vehicle units can be found in the appendix section B. The co-ordinates are measured with respect to the ADAMS co-ordinate system. This approach was used for all investigations in this master thesis.

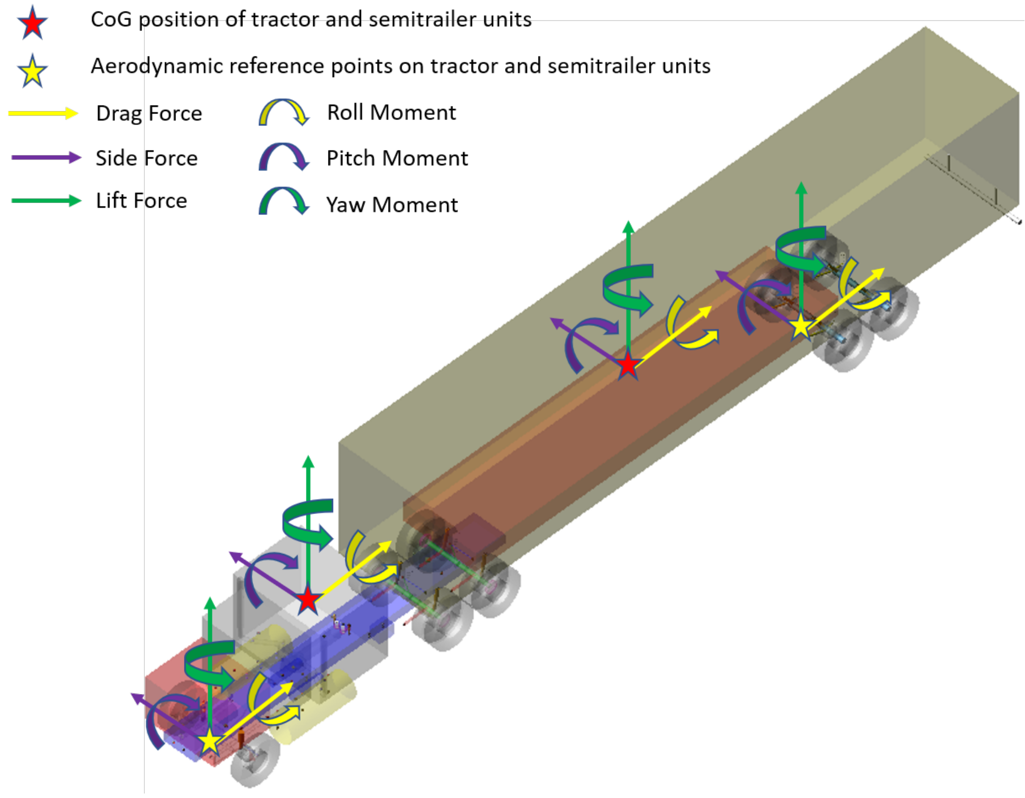

Figure 5.32: *Locations of aerodynamic load application*

5.4.3 Equations for transformed moments

The equations governing the aerodynamic forces (drag, side force and lift) and moments (roll, pitch and yaw) are expressed in equation 3.1. Since the aerodynamic loads will be applied at CoG as opposed to CoP (as mentioned in section 5.4.2), the moment equations are modified. These equations are individually applicable to either of the vehicle units, as described in equation 5.4.

$$\begin{aligned} M_{x,wind} &= \frac{1}{2}\rho ALV_{rel}^2 c^*_{roll}(\beta_w) \\ M_{y,wind} &= \frac{1}{2}\rho ALV_{rel}^2 c^*_{pitch}(\beta_w) \\ M_{z,wind} &= \frac{1}{2}\rho ALV_{rel}^2 c^*_{yaw}(\beta_w) \end{aligned} \tag{5.4}$$

where,
c^*_{roll} : transformed aerodynamic roll moment coefficient
c^*_{pitch} : transformed aerodynamic pitch moment coefficient
c^*_{yaw} : transformed aerodynamic yaw moment coefficient

5.4.4 Aerodynamic moment coefficients transformation

The aerodynamic force and moment coefficients are determined about the reference points (yellow stars) as shown in figure 4.8, while aerodynamic excitation are applied at the CoG of individual vehicle units (red stars) as illustrated in figure 5.30. Therefore the loads are transformed from the reference points to the point of application.

The aerodynamic forces coefficients can directly be used at the CoG point since they are independent of location of application. The moment coefficients, however, need to be geometrically transformed from the reference point to the CoG points, considering the effect of aerodynamic forces. The geometrical dimensions of the vehicle necessary for this transformation is as illustrated in the figure 5.33.

Figure 5.33 shows the longitudinal distances from the reference points (yellow stars) to the CoG (red stars) are denoted by T1 and ST1 for the tractor and semi-trailer unit respectively, under static conditions. The vertical distances of the CoG (red stars) from the roll axes of the respective vehicle units are noted by T2 and ST2. The roll axes for each vehicle unit is constructed by determining the static roll centers for each of the axles. The tractor unit is considered to roll about the axis connecting the static roll centers of axle 1 and axle 3. The semitrailer unit is considered to roll about the axis connecting the fifth wheel point and the static roll center of axle 4. The detailed dimensions can be found in the appendix section B.

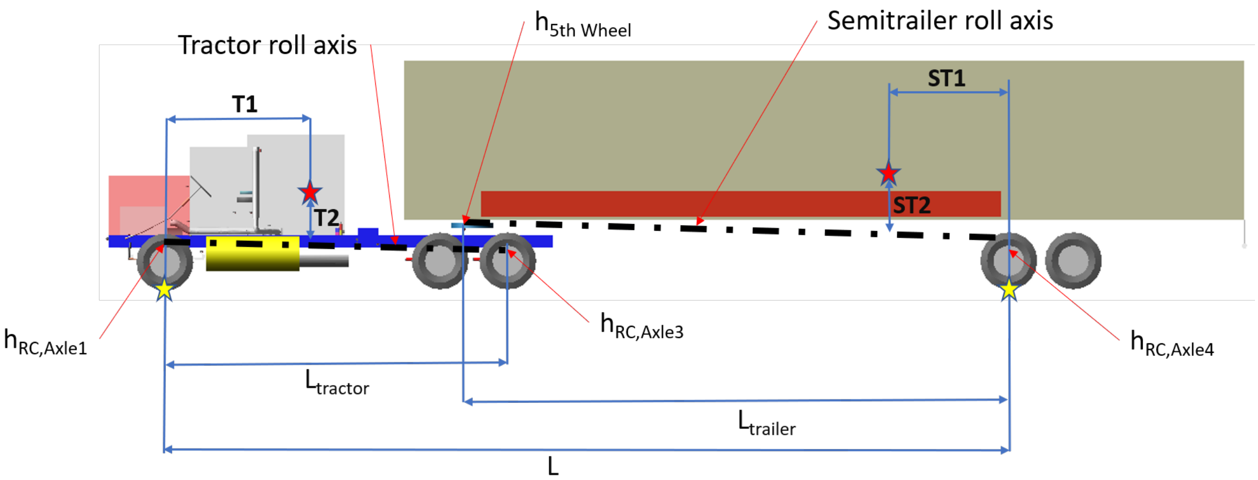

Figure 5.33: *Tractor semitrailer dimensions for moment coefficient transformation*

The roll moment coefficient is transformed from the reference point to the CoG while accounting for the effect of side force about the reference point. The pitch moment coefficient is similarly transformed by accounting for effect of lift and drag forces about the reference point. The yaw moment coefficient is similarly transformed by accounting for the effect of side force about the reference point. The equations for transformations for the tractor and semitrailer units are as described in equations 5.5 and 5.6, respectively.

$$
\begin{aligned}
c^*_{roll,T}(\beta_{w,T}) &= c_{roll,T}(\beta_{w.T}) + c_{s,T} * (\frac{h_{CoG,T} - h_{RRC,T}}{L}) \\
c^*_{pitch,T}(\beta_{w,T}) &= c_{pitch,T}(\beta_{w.T}) + c_{l,T} * (\frac{L_{CoG,T} - L_{ref,T}}{L}) - c_{d,T} * (\frac{h_{CoG,T}}{L}) \\
c^*_{yaw,T}(\beta_{w,T}) &= c_{yaw,T}(\beta_{w.T}) - c_{s,T} * (\frac{L_{CoG,T} - L_{ref,T}}{L})
\end{aligned} \tag{5.5}
$$

$$
\begin{aligned}
c^*_{roll,ST}(\beta_{w,ST}) &= c_{roll,ST}(\beta_{w.ST}) + c_{s,ST} * (\frac{h_{CoG,ST} - h_{RRC,ST}}{L}) \\
c^*_{pitch,ST}(\beta_{w,ST}) &= c_{pitch,ST}(\beta_{w.ST}) - c_{l,ST} * (\frac{L_{ref,ST} - L_{CoG,ST}}{L}) - c_{d,ST} * (\frac{h_{CoG,ST}}{L}) \\
c^*_{yaw,ST}(\beta_{w,ST}) &= c_{yaw,ST}(\beta_{w.ST}) + c_{s,ST} * (\frac{L_{ref,ST} - L_{CoG,ST}}{L})
\end{aligned} \tag{5.6}
$$

Figure 5.34 shows the differences between the moment coefficients determined from the CFD simulations and the transformed moment coefficients for all wind yaw angles between 0°and 90°.

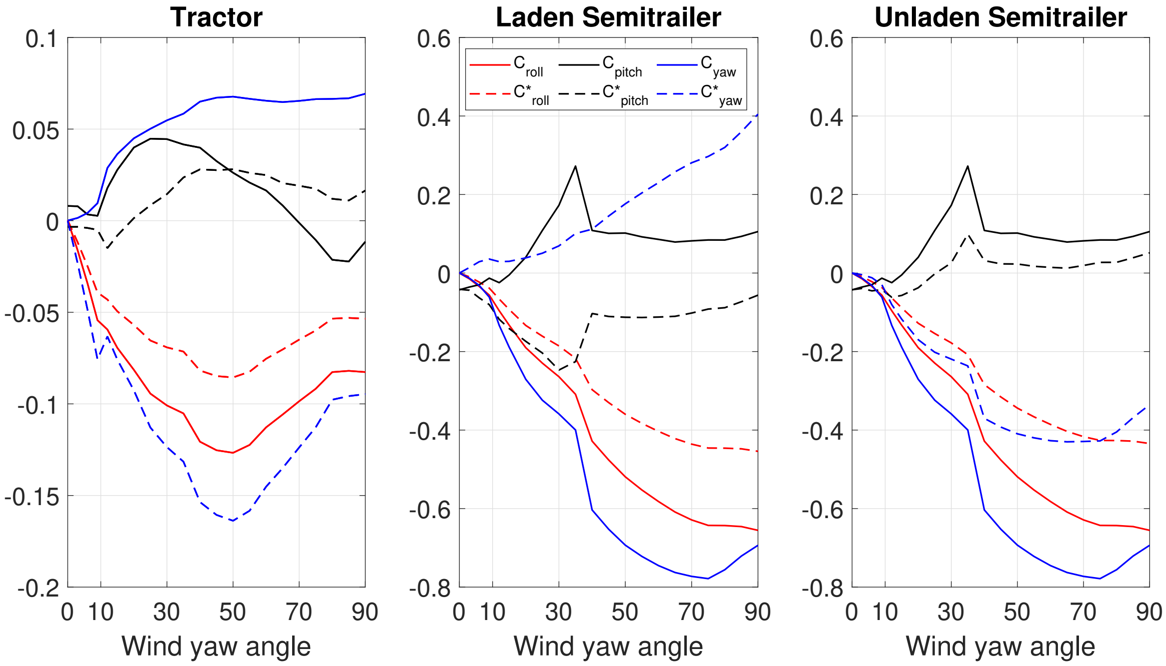

Figure 5.34: *Transformed moment coefficients*

5.4.5 Relative velocity

The aerodynamic forces and moments are calculated using the relative velocities between the wind and the individual vehicle units, as one of the components as shown in equations 3.1 and 5.4. The wind velocities are with respect to NPRA coordinate system and the vehicle velocities are with defined with respect to ADAMS coordinate system as illustrated in figure 5.35.

To calculate the relative velocity, the wind velocity components are to be transformed to from NPRA coordinate system to ADAMS vehicle coordinate system. This is achieved with a transformation matrix as depicted by equations 5.7 [9] and 5.8 [9]. The difference between transformed wind velocity and the vehicle velocity is then calculated as shown in equation 5.9 [9]. This results in X and Y components of relative velocity in ADAMS vehicle coordinate system.

$$T_{vehicle,i} = \begin{bmatrix} \cos(\psi_i) & \sin(\psi_i) \\ -\sin(\psi_i) & \cos(\psi_i) \end{bmatrix} \approx \begin{bmatrix} 1 & \psi_i \\ -\psi_i & 1 \end{bmatrix} \tag{5.7}$$

$$\begin{bmatrix} V_{x,wind} \\ V_{y,wind} \end{bmatrix}_{LCS,i} = T_{vehicle,i} * \begin{bmatrix} -V_{x,wind} \\ -V_{y,wind} \end{bmatrix}_{ECS,i} \tag{5.8}$$

$$\begin{bmatrix} V_x \\ V_y \end{bmatrix}_{rel,i} = \begin{bmatrix} V_{x,wind} \\ V_{y,wind} \end{bmatrix}_{LCS,i} - \begin{bmatrix} V_x \\ V_y \end{bmatrix}_{vehicle,i} \tag{5.9}$$

where,

i : tractor, semitrailer units

The magnitude of relative velocity is thereby determined using equation 5.10 [9].

$$V_{rel,wind,i} = \sqrt{V_{x,rel,i}^2 + V_{y,rel,i}^2} \tag{5.10}$$

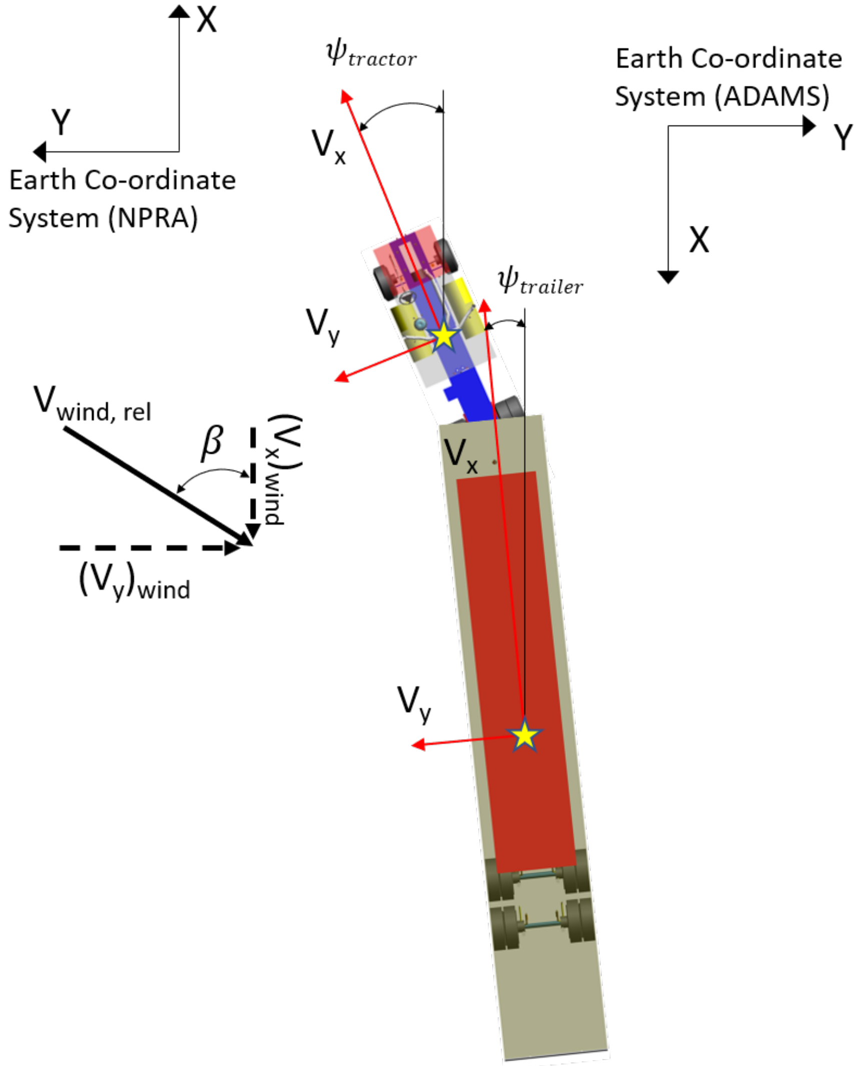

Figure 5.35: *Relative velocity and wind yaw angle*

5.4.6 Wind yaw angle

The aerodynamic force and moment coefficients are dependent on the angle of attack of the wind on the vehicle, which is referred in this thesis as wind yaw angle. It is calculated using the X and Y components of the relative velocity, as described in equation 5.11 [9]. The wind yaw angle is calculated for individual vehicle units and will be used to determine the instantaneous aerodynamic coefficients based on the wind and individual vehicle unit orientation. A graphical representation of the wind yaw angle can be perceived in figure 5.35.

$$\beta_{w,i} = \arctan\left(\frac{V_{y,rel,i}}{V_{x,rel,i}}\right) \tag{5.11}$$

5.5 Driver Model Construction

5.5.1 Pure Pursuit Method [42]

One of the driver models investigated in this work is an extension of the pure pursuit controller [42] that was previously employed to investigate the lateral stability of an intercity bus under similar environmental conditions [9]. A variant of the pure pursuit method, this driver model uses the center of gravity of the tractor as a reference point on the vehicle instead of the rear axle. This technique consists of geometrically determining the curvature of a circular arc which connects the center of gravity of the tractor unit to an aim-point or preview point on the path in front of the vehicle. The vehicle motion is assumed to observe "ideal-tracking" tyres implying no sideslip and independent of forces.

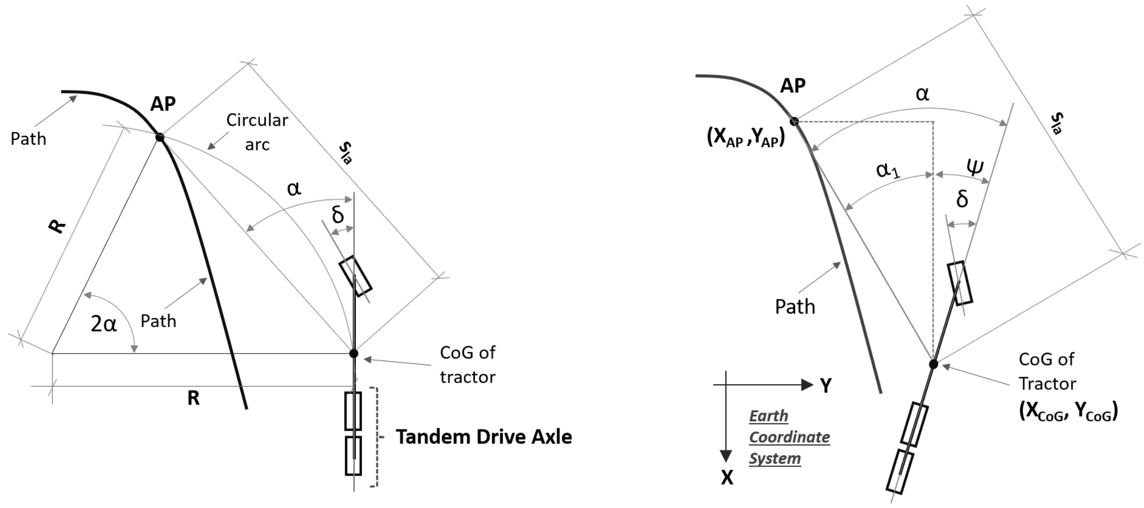

Figure 5.36: *Variant of the PPC [42]: (left) Pure Pursuit Geometry; (right) positions of the characteristic points and angles*

The tractor unit's center of gravity (X_{cog}, Y_{cog}) and the location of the aim point or preview point AP (X_{AP}, Y_{AP}) on the moving bridge are determined (Figure 5.36). When calculating the location of the aim point, a look-ahead distance or preview distance s_{la} has been considered from the tractor unit's center of gravity.

It should be noted that the current vehicle under investigation is a multi-unit vehicle.

The investigation also compared the solely geometric-oriented pure pursuit controller with the built-in machine control driver model existing within the MSC.ADAMS/Car Truck module; an advanced controller that is realistic and robustly stable.

Parameter tuning

To investigate driver behaviour and tracking ability of a vehicle (passenger car/bus) on the Bjornafjorden floating bridge, the Hexatech 1CTR driver-in-the-loop motion platform simulator (CASTER) was extensively used [26] [17]. HSA responses from the driving simulator tests [26] [17] and the numerical simulations [9] were compared to tune the pure pursuit controller. The results from numerical simulation [9] for the case of 0.6s of Look Ahead Time for the bus at a vehicle speed of 70 km/h has been reported to agree well with the results from the motion platform simulator [26] [17]. For the tractor semitrailer however, no such investigation exists. Since the LAT of 0.6s has worked for an intercity bus which is also a heavy vehicle albeit a single-unit, this value is used as the starting point for the tractor-semitrailer.

It is worth noting that the vehicle's intended path according to the lateral motion of the bridge is different to what the driver sees and manoeuvres the vehicle to. Figure 5.37 illustrates an example of the path that the vehicle is required to follow and the path that the driver would react to for a vehicle speed of 36 km/h.

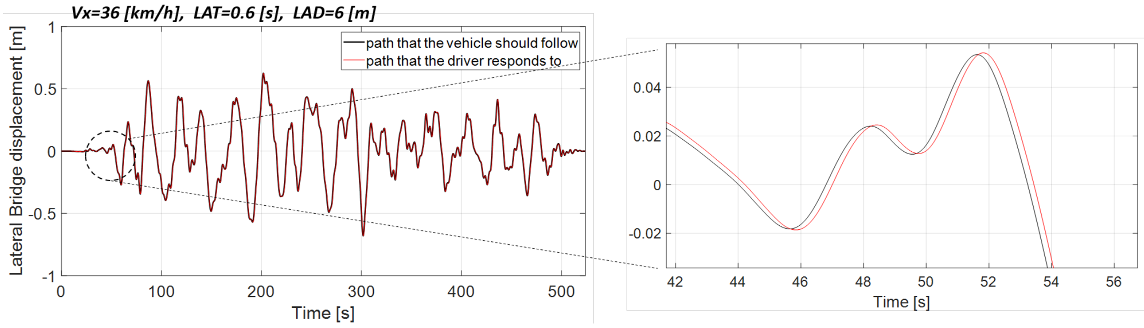

Figure 5.37: *Path that the vehicle is required follow and that the driver reacts to*

Lateral Offset

The pure pursuit technique disregards the influence of wind components when determining the vehicle's steering angle [42]. In the numerical simulation performed by Sekulic et al [9], lateral offset appears within the total lateral vehicle displacement. Zhou and Chen, 2015 [48] and Chen and Cai, 2004 [21] have also reported the presence of the lateral offset from numerical investigations on a vehicle with high side area subjected to cross-wind load.

However, in reality, the driver compensates for the lateral offset by steering the vehicle back to the desired path under the influence of crosswind forces acting on the vehicle. This approach performs well under slow dynamics since the side wind is largely constant or does not change direction.

The introduction of "steering compensation" to the driver model based on the pure pursuit technique is an enhancement that has been suggested [9]. Consequently, the built-in driver model in MSC.ADAMS/Car Truck [12] [13] module with its advanced properties is considered as a candidate. This driver model accounts for the lateral offset and is compensated for by the controller.

5.5.2 Machine Control - MSC Adams

The MSC.ADAMS steering controller is an advanced controller that determines the required steering angle through a feed-forward and feedback component, along with lateral displacement compensation embedded within a PID framework. The tunable parameters of this driver model are the controller gains P, I, and D, including the preview time or look ahead time.

A preview time or look ahead time of 0.6s was considered as a starting point following earlier investigations [9] [17]. Furthermore, the gains for the PID controller were set to the suggested values in Figure 5.38 that work well with any other built-in full-vehicle simulation manoeuvres for the tractor semitrailer model within MSC.ADAMS/Car-Truck [12] [13].

However, a preview time of 0.6s produced numerical instability to the simulation. After preliminary investigation, it was discovered that a preview time of 0.4s performed well for vehicle speeds up to 90km/h, while a preview time of 0.3s responded well for 108km/h. It is consciously decided to only work with the preview time as the tunable parameter and exclude the P, I, and D.

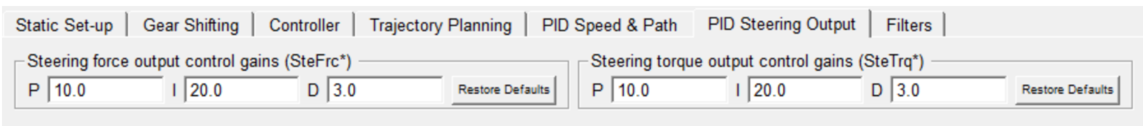

Figure 5.38: *PID Gains for the steering controller in MSC.ADAMS*

It is proposed that a detailed investigation in respect to the preview time and controller gains be performed as a future scope (section 8).

5.6 Co-simulation

The bridge motion is enabled in the MSC.ADAMS/Car-Truck via the X-post test rig template, as mentioned in section 5.3.2. The aerodynamic loads are dynamically determined in MATLAB/Simulink (section 5.4). The Snider driver model is constructed in the MATLAB/Simulink interface as described in section 5.5.1. Since multiple tools are being used, a co-simulation is employed in this master thesis. This section describes the details of the co-simulation model, with MATLAB/Simulink as master and MSC.ADAMS/Car-Truck as slave, as illustrated through the flowchart in figure 5.39. A detailed image of the Simulink blocks can be found in the appendix section A.

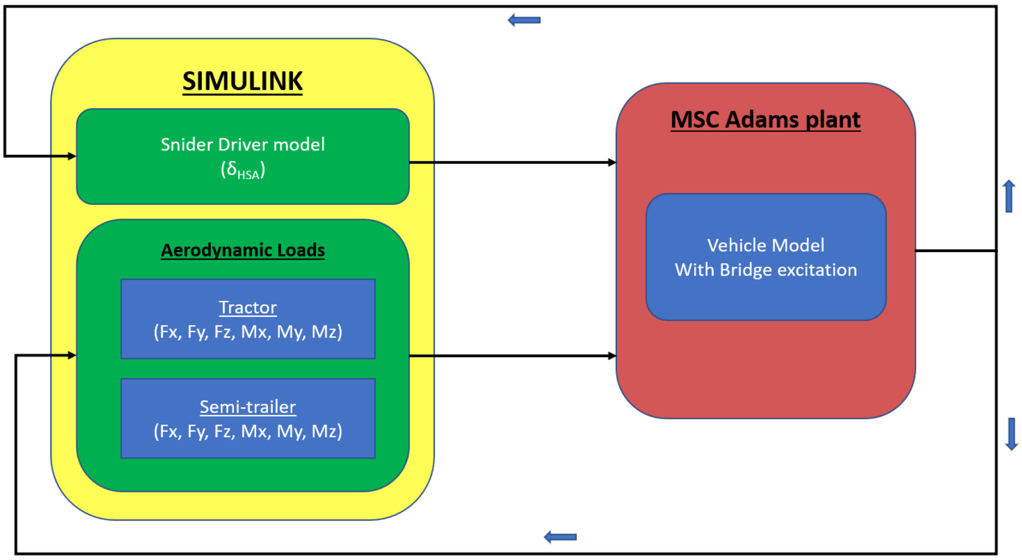

Figure 5.39: *Co-simulation flowchart*

5.6.1 Aerodynamic loads

To determine the aerodynamic loads, the wind excitation time history from the W6 weather data is chosen according to the test speed. The vehicle velocity (Vx and Vy) and instantaneous yaw angles of the tractor and semitrailer units are obtained as outputs from the ADAMS plant block. These parameters form the inputs to the MATLAB Simulink model. Relative velocity, wind yaw angle and thereby the appropriate aerodynamic co-efficients are determined. The aerodynamic forces (drag, side force and lift) and moments (roll, pitch and yaw) are computed as described in section 5.4. These forces and moments form the inputs to the ADAMS plant block. This process is represented as a flow chart in figure 5.40.

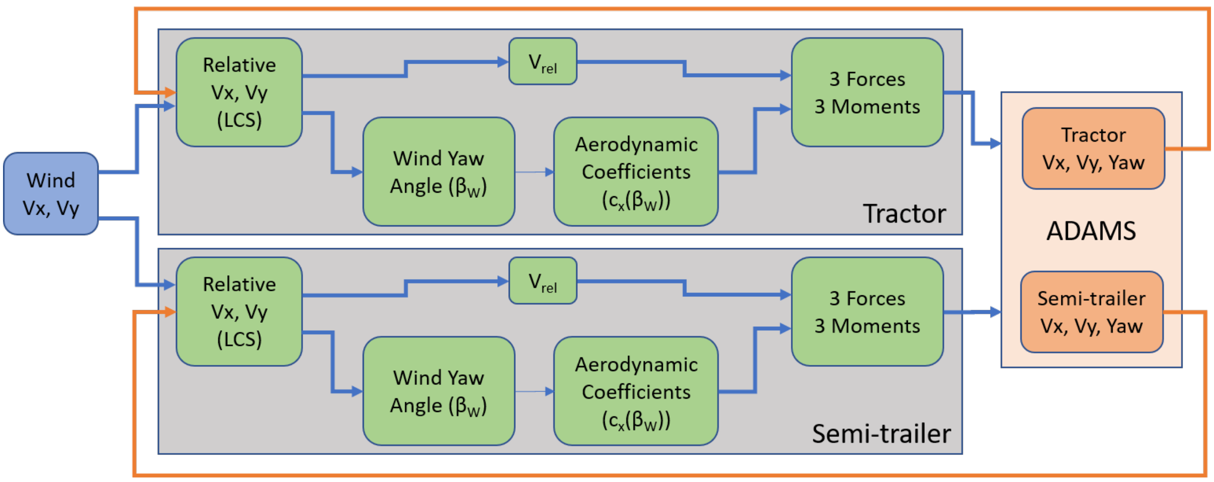

Figure 5.40: *Wind excitation Co-simulation flowchart*

5.6.2 Driver model

The Snider driver model, as described in section 5.5.1 is used to compute the steering input to the tractor semitrailer vehicle. The instantaneous lateral position and orientation (yaw) of the tractor is output from the ADAMS plant block. This, along with the desired lateral position from the predetermined path, form the inputs to the Snider driver model. The HSA is thereby computed, based on a look-ahead time (LAT). This forms the input to the ADAMS plant block. This procedure is depicted through a flowchart in figure 5.41

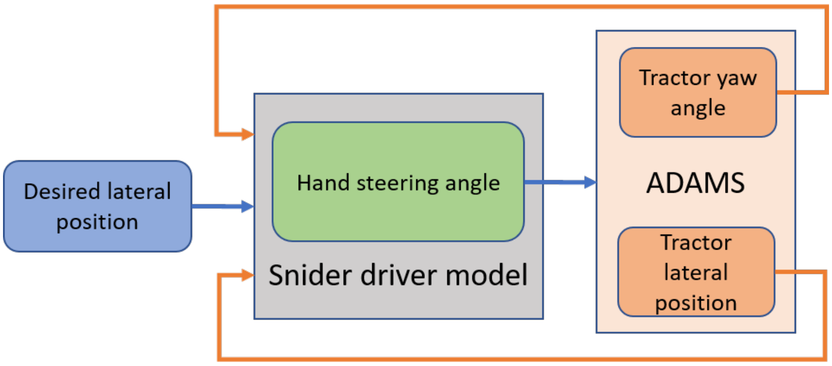

Figure 5.41: *Snider driver model flowchart*

5.6.3 Solver settings

Solver settings are important to obtain accurate results and a trade off with simulation time. In this work, the solver settings in MSC.ADAMS/Car-Truck were set to the GSTIFF-I3 formulation. The *Error* term was set to a value of 1.0E-02 and the H_{max} was set to 1.0E-03 (Fig. 5.42). Multi-threading was enabled to exploit the computational power up to the hardware's limit, while all the remaining fields within the solver settings were set to the default values.

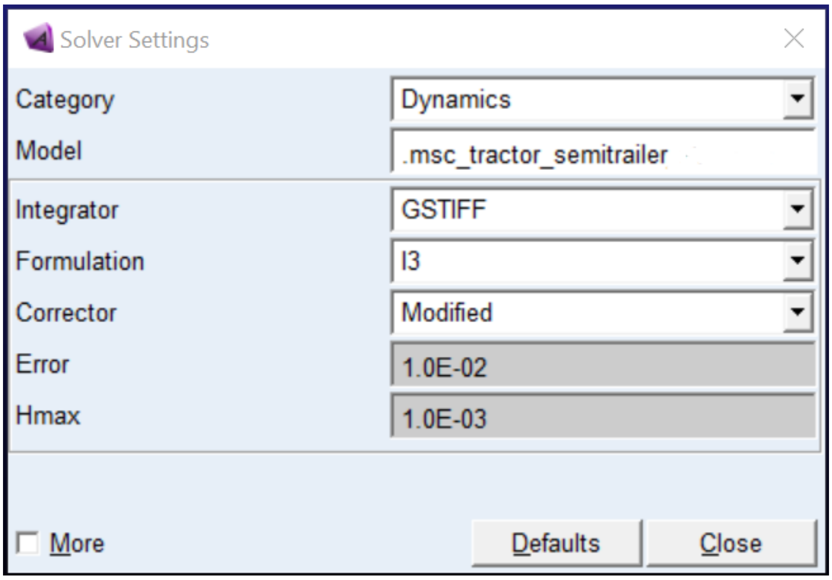

Figure 5.42: *Solver settings in MSC.ADAMS*

5.6.4 Simulation procedure

Pre-requisites for co-simulation:

1. Valid ADAMS Car/Truck license (models build on version 2019.2)
2. Valid MATLAB/Simulink license

3. ADAMS/Control plugin enabled via plugin manager as depicted in the figure 5.43

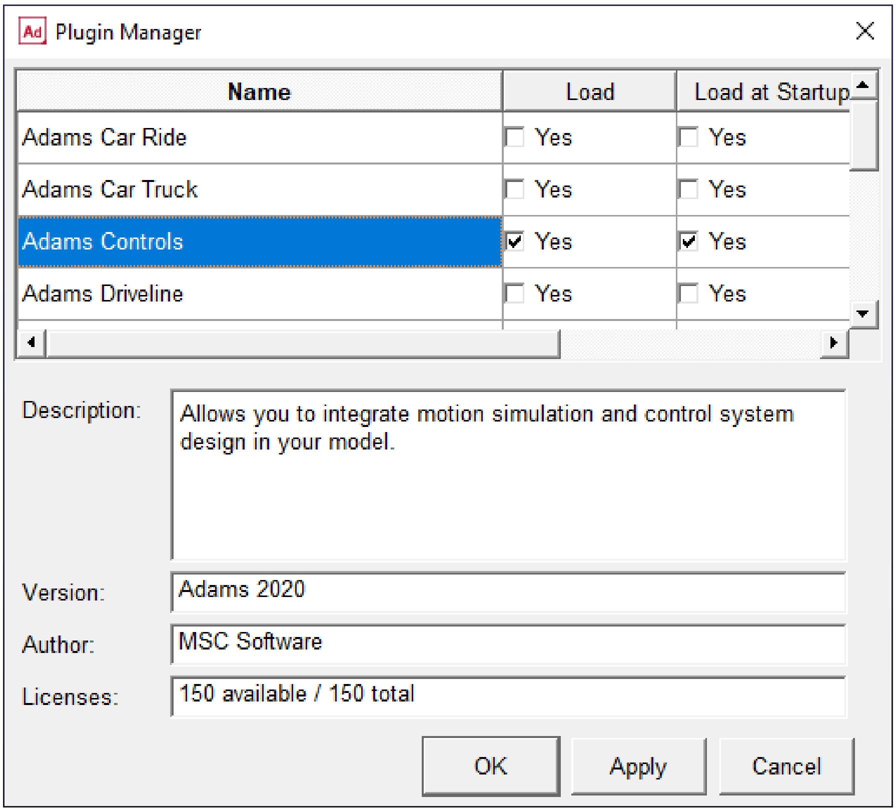

Figure 5.43: *ADAMS GUI: Plugin Manager*

4. The "x_post_rig.cmd" command file to couple the tire motion to the test rig

The following are the steps to execute a co-simulation for a chosen speed and road friction condition:

1. Run the MATLAB script for the chosen test speed, to generate the variable required for co-simulation
2. Launch ADAMS Car software in standard mode and choose the appropriate file directory (same as that of the MATLAB/Simulink files). ADAMS co-simulation and results file will be saved here
3. Open the tractor semitrailer assembly (.asy) file
4. Read the "x_post_rig.cmd" command file with a chosen macro name
5. Pick the .asy file in the macro dialogue and run the macro (Xpostrigmacro GUI shown in figure 5.44)

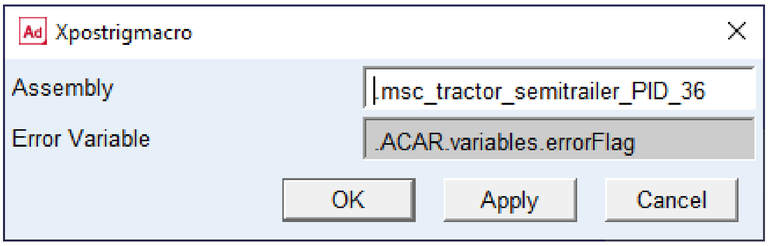

Figure 5.44: *ADAMS GUI: Macro*

6. Open "File driven events" in full vehicle analysis under Simulate menu. Choose the vehicle assembly. Set analysis mode to "files_only". Choose the appropriate road and driver control files. Provide an appropriate

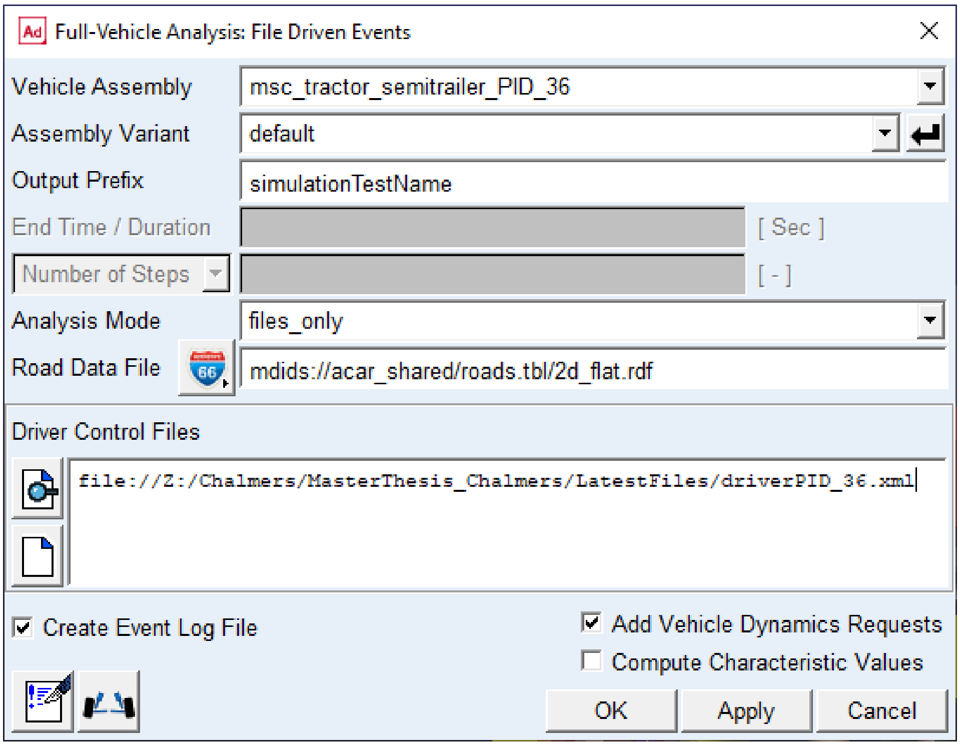

Figure 5.45: *ADAMS GUI: File driven events*

output prefix and click OK. An exmaple of the GUI is shown in figure 5.45. MSC.ADAMS/Car-Truck generates a set of files in the chosen directory

7. Create necessary Plant input and output variables

8. Open “Plant export” under control menu. Check the “initialization command” box to read the ”_control.acf” file. Select the plant input and output signals. Choose ”MATLAB” as the target software and click OK. An example of the ADAMS/Controls Plant Export GUI is illustrated in figure 5.46. This procedure also generates a set of files in the directory

9. Run the .m file generated in the directory, on MATLAB. This creates additional variables to necessitate co-simulation

10. Execute “adams_sys” in the command window. This generates an ADAMS plant block on Simulink interface, which can be combined with other Simulink blocks required for co-simulation

11. In the ADAMS plant block parameters, change the communication interval and number of communications per output step fields as shown in figure 5.47 and click OK

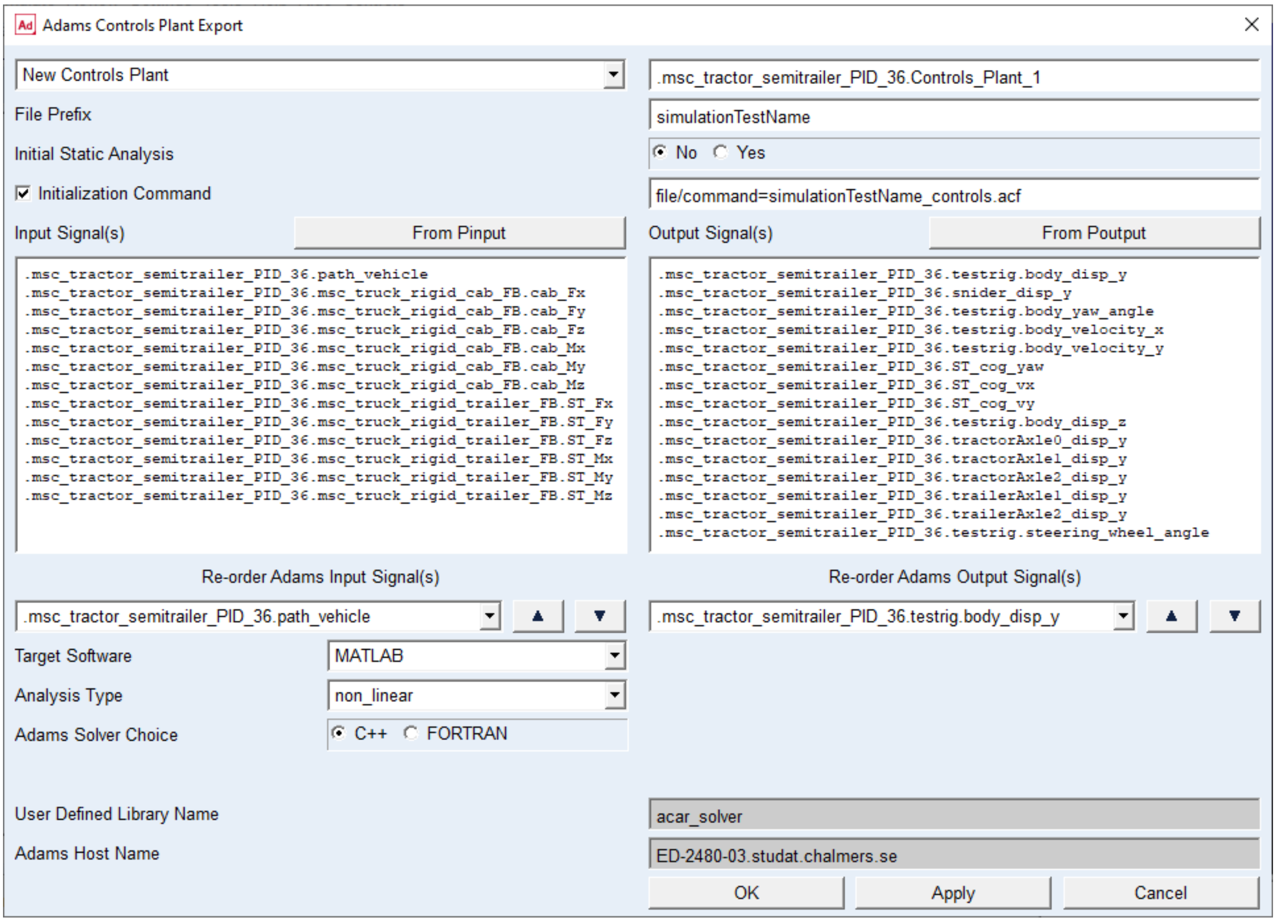

Figure 5.46: *ADAMS GUI: Plant export*

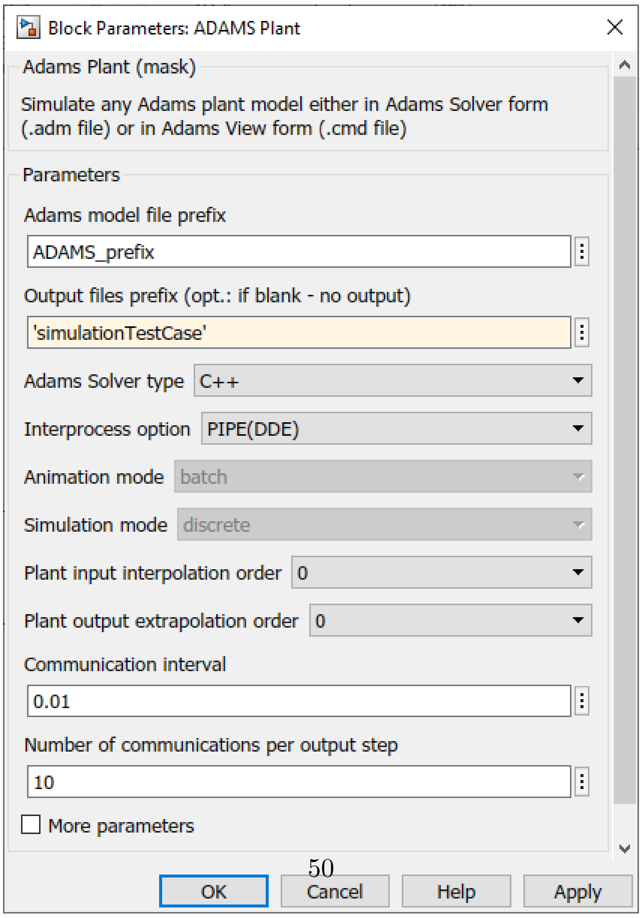

Figure 5.47: *ADAMS GUI: Plant block parameters*

12. Run the Simulink file. This generates a results file (.res) which can be imported into ADAMS postprocessor for analysis

5.7 Test matrix

The influence of trailer payload, road friction and vehicle speeds on the evaluation parameters mentioned in the research gap (section 2.3) is important. These are the conditions under which the vehicle will most likely operate. A set of test scenarios are chosen as described in the figure 5.48.

Road friction [-]	Laden mass [t]	Vehicle speed [km/h]				
0.7	17	36	54	72	90	108
0.7	0	36	54	72	90	108
0.3	17	36	54	72	90	108
0.3	0	36	54	72	90	108

Figure 5.48: *Test Matrix*

6 RESULTS AND DISCUSSION

6.1 Driver Model Comparison

A comparison between the the Pure Pursuit Controller (PPC) [42] and that of the advanced driver model from MSC.ADAMS is made for a laden vehicle under a road friction μ=0.7. Preliminary investigations concerning the Look Ahead Time (LAT) or Preview Time of 0.6s indicated unstable behaviour for higher speeds, while a LAT of 0.4s worked well with every speed except for the vehicle speed of 108 km/h. Thus, a LAT of 0.4s was set in both the driver model controllers.

Figure 6.1 shows the Hand Steering Wheel Angle (HSA) for the PPC and the advanced driver model from MSC.ADAMS. Volatile HSA values from the PPC model are observed compared to that of the MSC.ADAMS controller although both signals oscillate around similar mean values. In the frequency domain, the amplitude of the initial frequency are the same, while between 0.2Hz and 0.3Hz, the amplitudes are different (Figure 6.2). This can be attributed to the fact that the PPC controller only exploits geometric relationship to compute the steering angle, while the MSC.ADAMS driver model is a far advanced controller that takes in feedback along with lateral path offset compensation embedded within a PID control.

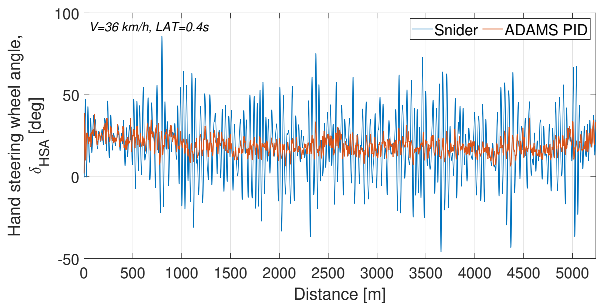

Figure 6.1: *Hand Steering Wheel angle signals for a laden vehicle on road with friction μ=0.7*

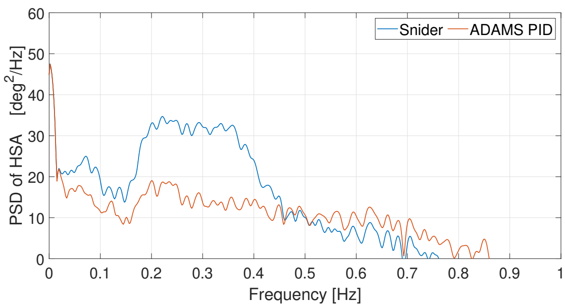

Figure 6.2: *Power Spectral Density of signals from Fig. 6.1 as a function of frequency*

In respect to the path tracking ability of the PPC, a lateral offset exists between the tractor CoG and desired bridge path (Figure 6.3), while the tractor CoG closely follows the desired path of the bridge with the MSC.ADAMS driver model (Figure 6.4). This is because the pure pursuit tracking method solely utilizes geometric relationships between the vehicle and the desired path to compute the steering wheel angle and does not account for cross-wind load's effect on the vehicle's lateral offset. However, in reality, the driver compensates for the lateral offset by steering the vehicle back to the intended path under the influence of crosswind forces acting on the vehicle.

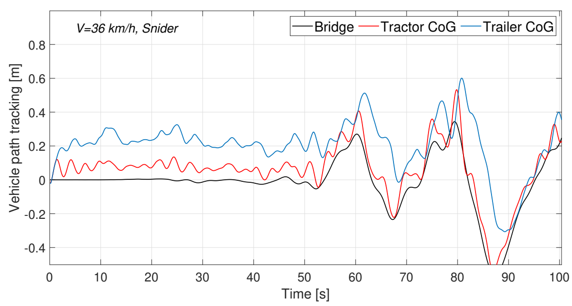

Figure 6.3: *Lateral path offset of a laden vehicle with Snider (2009) model under μ=0.7*

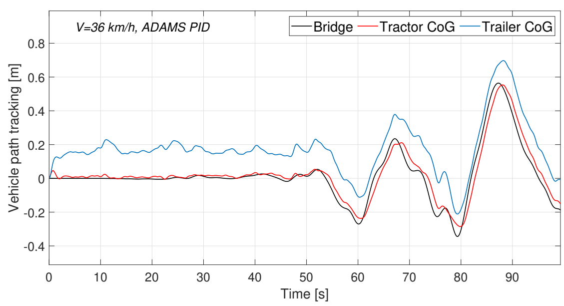

Figure 6.4: *Lateral path offset of a laden vehicle with ADAMS driver model under μ=0.7*

Since the steering angle amplitudes occurs around the same frequency but differ only in amplitude (Figure 6.2, and also the reference point in the tractor closely follows the intended path under this scenario, the MSC.ADAMS controller has been considered for all the investigations in this study.

6.2 Wind yaw angles

This section describes the wind yaw angles experienced by the vehicle units, for each test speed under the W6 weather condition. Figures 6.5 and 6.6 illustrate the time histories of wind yaw angles the experienced by the tractor and semitrailer units, respectively. A decreasing trend in wind yaw angles is observed with increasing vehicle speeds, for a laden trailer on 0.7 friction road.

Furthermore, figures 6.7 and 6.8 illustrate the maximum and minimum wind yaw angle the vehicle units experience for different trailer loads and road friction conditions. In $\mu = 0.7$ road conditions, the wind yaw angles are slightly larger in range for unladen vehicle as compared to that of the laden vehicle. This phenomenon is even more significant on $\mu = 0.3$ road. For a laden vehicle, lower wind yaw angles are experienced by the vehicle on a $\mu = 0.3$ road as opposed to a $\mu = 0.7$ road. For an unladen vehicle, higher wind yaw angles are experienced by the vehicle on a $\mu = 0.3$ road when compared to that of $\mu = 0.7$ road. The tractor and semitrailer units experience wind yaw angle within a similar range when compared with each other, as a result of vehicle articulation angles being small.

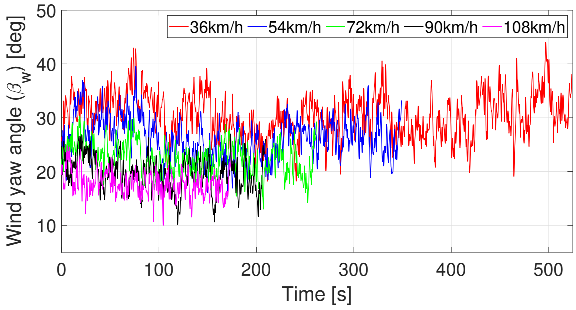

Figure 6.5: *Wind yaw angle - Tractor*

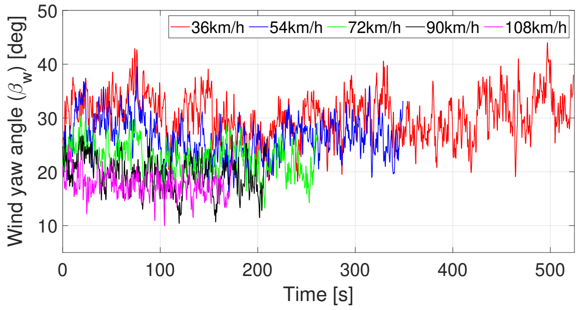

Figure 6.6: *Wind yaw angle - Semitrailer*

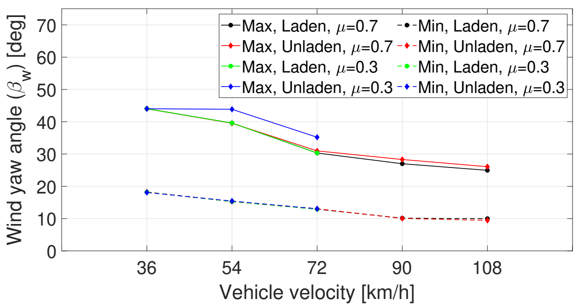

Figure 6.7: *Wind yaw angle summary - Tractor*

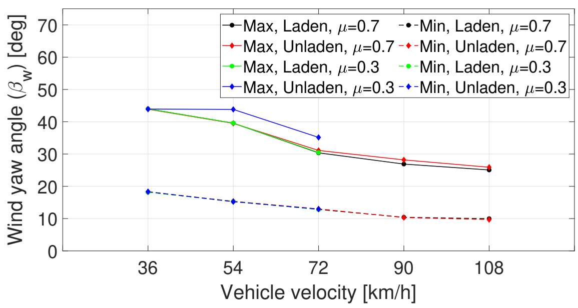

Figure 6.8: *Wind yaw angle summary - Semitrailer*

6.3 Vehicle articulation

The yaw motion experienced by the tractor and semitrailer units is illustrated as their time histories in figures 6.9 and 6.10. The yaw motion of the semitrailer is of a larger range, accounting for the larger aerodynamic loads experienced by the semitrailer when compared to the tractor unit. It is also observed that the range of yaw motion is higher for higher speeds in both the vehicle units.

Figures 6.11 and 6.12 summarize the maximum and minimum yaw angles the vehicle experiences, for different test cases, under varying semitrailer load and road friction conditions. The yaw motion range for both vehicle units are higher for the unladen vehicle as compared to the laden vehicle, under same road surface friction. For a vehicle operating at same load condition, the yaw motion ranges higher for a road surface of friction 0.3 as compared to that of friction 0.7.

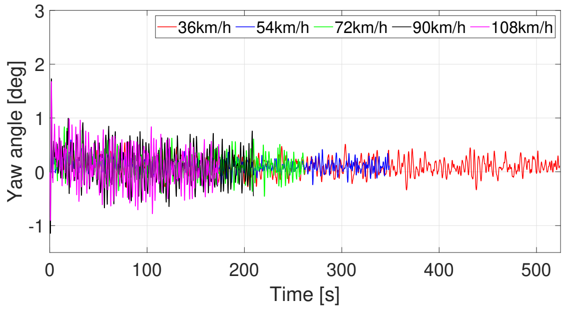

Figure 6.9: *Yaw angle - Tractor*

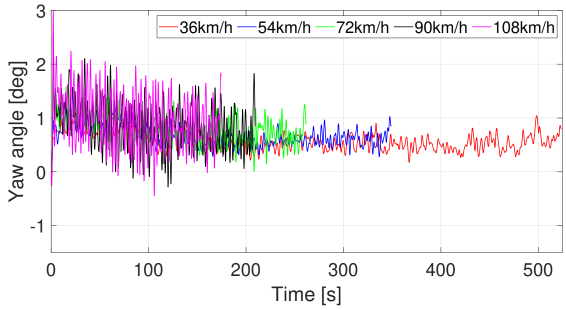

Figure 6.10: *Yaw angle - Semitrailer*

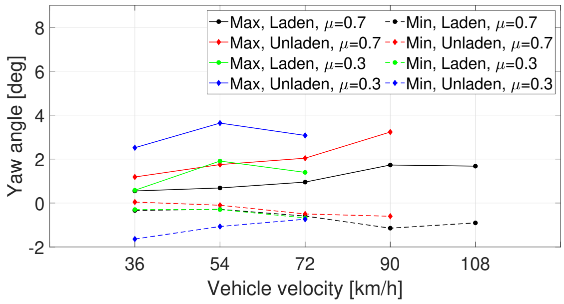

Figure 6.11: *Yaw angle summary - Tractor*

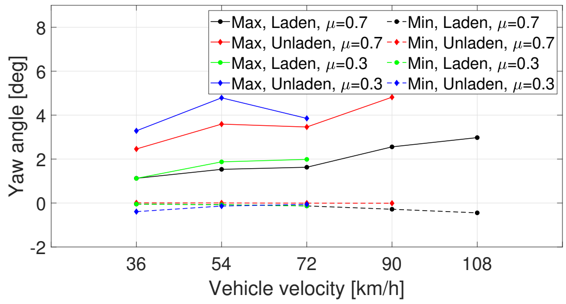

Figure 6.12: *Yaw angle summary - Semitrailer*

The time histories of articulation between the tractor and semitrailer units are shown in figure 6.13. It can be observed that the articulation is less than 5°across all test speeds for a laden vehicle on $\mu = 0.7$ road. The maximum vehicle articulations for all test speeds are depicted in figure 6.14. It is observed that the articulation is approximately 5°for most vehicle test speeds across all vehicle load and road friction conditions. Thus the observation from the vehicle yaw motion (figures 6.11 and 6.12) can be extended to vehicle articulation (6.14). The maximum articulation is approximately 5.5°for the unladen vehicle test speed of 90km/h. This difference in articulation between laden and unladen vehicles is magnified at higher vehicle test speeds.

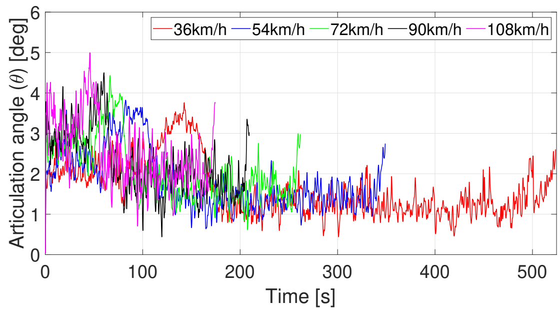

Figure 6.13: *Articulation angle - Laden;* $\mu = 0.7$

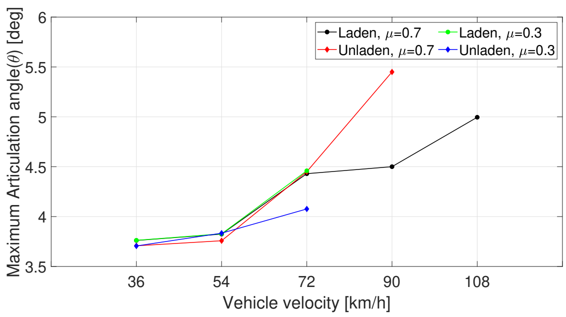

Figure 6.14: *Maximum articulation angle - Summary*

6.4 Path Tracking or Lateral Lane deviation

This section describes the path tracking, vehicle lateral offset and lane deviation across vehicle speeds under different scenarios described in the test matrix.

Figure (6.15) renders simulation results for the path tracking ability of a laden vehicle at 36 km/h under high road friction. As the reference point considered in the driver model is the first axle of the tandem drive axles, the tractor is observed to closely track and follow the desired path on the bridge. However, there exists a lateral offset from the trailer's CoG as it is consequential of the crosswind.

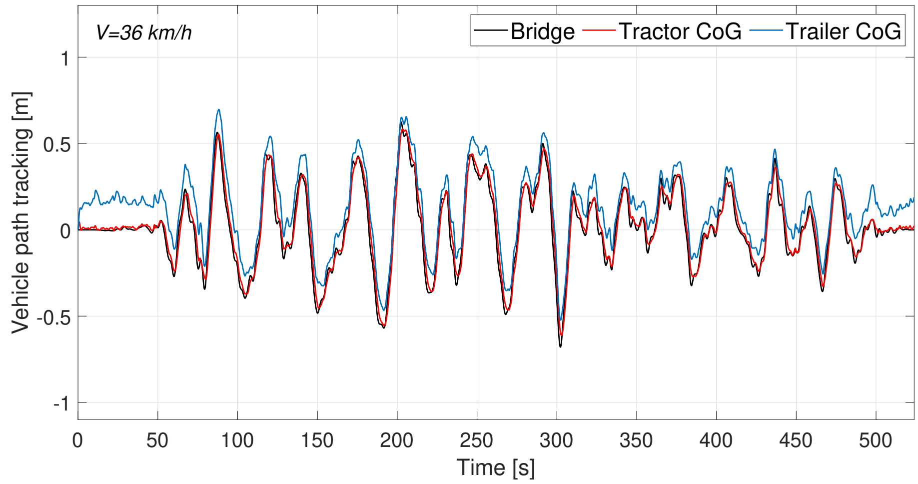

Figure 6.15: *Path tracking ability of a laden vehicle with ADAMS driver model under μ=0.7*

In respect to the lane violation, the rear corners on the trailer are analyzed. Figure (6.16) depicts the trace of the rear left and right corners for the base case for a vehicle speed of 36 km/h embedded on a lane with width 3.6m and the center line. Both the markers do not violate the lane width throughout the journey along the length of the bridge.

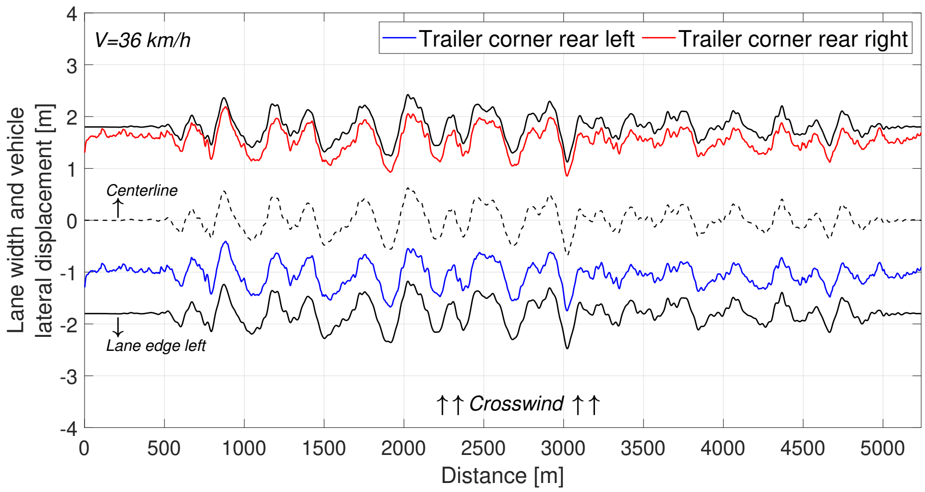

Figure 6.16: *Lane deviation and lateral displacement of a laden Tractor semitrailer at 36 km/h with μ=0.7*

Figure (6.17) depicts the trace of the rear left and right corners for the base case for a vehicle speed of 90 km/h as a function of the length of the bridge. The rear right corner of the trailer is observed to violate the lane on multiple occasions compared to that of the left rear corner.

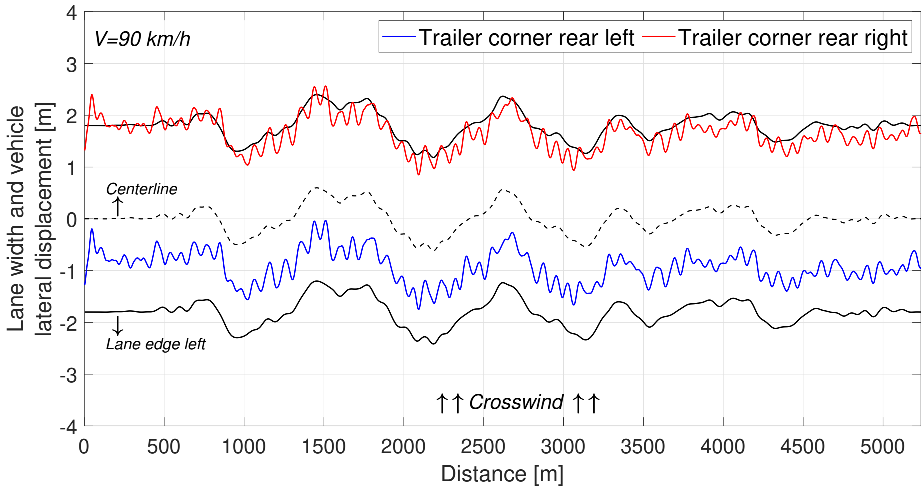

Figure 6.17: *Lane deviation and lateral displacement of a laden Tractor semitrailer at 90 km/h with μ=0.7*

For a laden vehicle under μ=0.7, the maximum lane deviation across different vehicle speeds has been summarized in Figure (6.18). The whole vehicle stays within the lane at 36 km/h, while the rear right corner of the trailer violates the lane in all other vehicle speeds. The maximal deviation increases with increasing vehicle speed and is as high as 0.7m for a speed of 108 km/h. Furthermore, the maximal deviations are significant at the beginning of the bridge (Figure 6.17).

The total lane violations as a function of percentage of the travel time of each speed has been illustrated in Figure (6.19). It is observed that the percentage of lane violation is greater with increase in vehicle speed. The vehicle violates the lane for a significant duration of the travel time (> 20%) for the case of 90km/h and 108km/h.

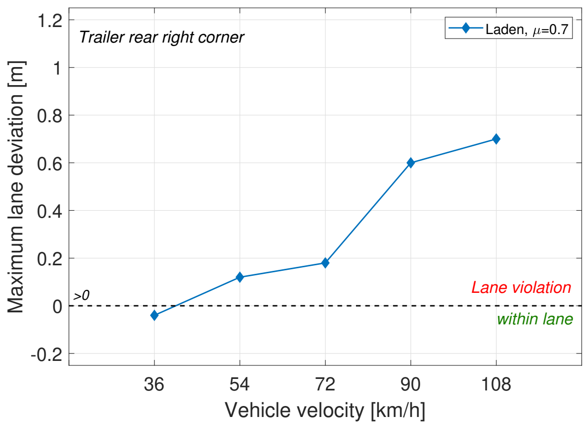

Figure 6.18: *Maximum lane deviation for different vehicle speeds*

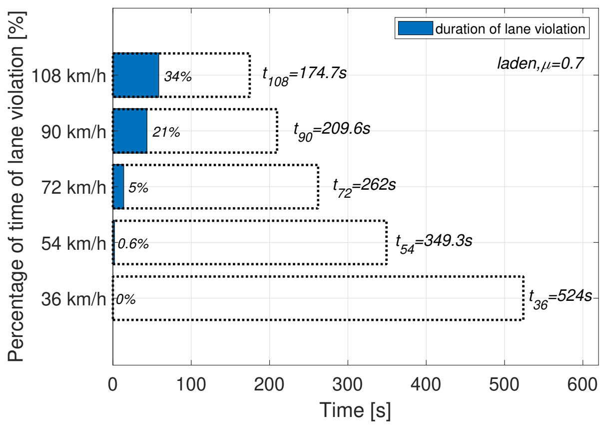

Figure 6.19: *Lane violation as percentage of travel time for different vehicle speeds*

Similar to the figures (6.18) and (6.19), figures (6.20) and (6.21) summarize the maximum lane deviation and the lane violation percentage for different scenarios. The maximum lane deviations are lowest for a vehicle speed of 36 km/h compared to higher vehicle speeds under all scenarios. Under a low road friction, the unladen vehicle deviates the lane even for a vehicle speed of 36 km/h. Another observation is that the lane deviations are greater for an unladen vehicle under high road friction compared to that of the laden vehicle at 54km/h and 72km/h. It was noticed during the simulations that the vehicle completely slides off under low friction at 90 km/h. The lane violation percentage are consistently greater for an unladen vehicle under low friction across all vehicle speeds. Furthermore, the unladen vehicle at μ=0.7 also show a greater percentage of lane violation for speeds of 54km/h and upwards.

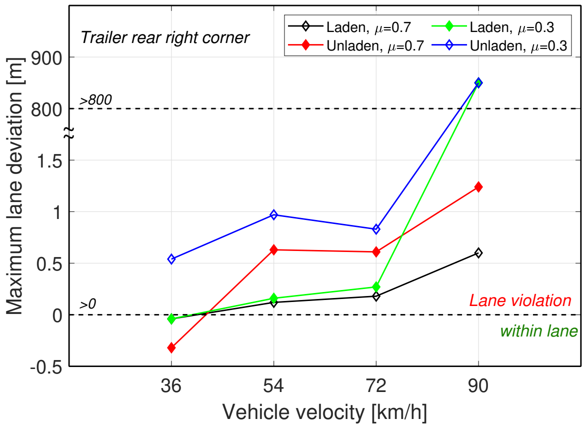

Figure 6.20: *Maximum lane deviation under different scenarios across vehicle speeds*

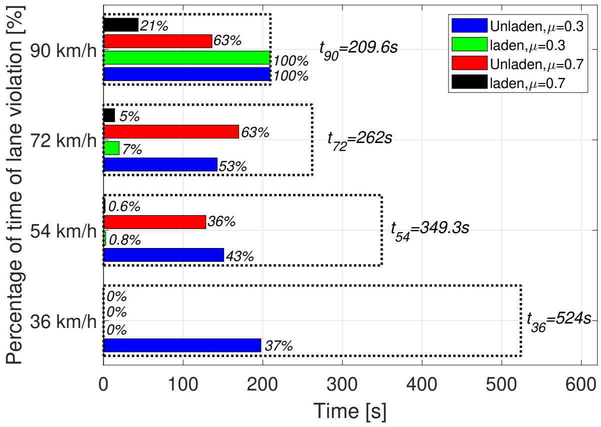

Figure 6.21: *Lane violation as percentage of travel time under different scenarios across different vehicle speeds*

6.5 Steering Effort

Figure 6.22 shows HSA inputs from the driver model to traverse the bridge, for different vehicle test speeds for a laden vehicle on $\mu = 0.7$ road. It can be inferred that higher steering inputs are needed with increasing vehicle speeds. Figure 6.23 denotes the PSD of the signals from figure 6.22. It is observed that the PSD plots have two characteristic peaks, around 0.01Hz and 0.3Hz. The peak at 0.01Hz corresponds to the crosswind disturbances as observed from figure 5.5. It can be noticed that this peak has a higher PSD magnitude, denoting that the driver model must provide relatively larger magnitude of steering inputs at lower frequency to compensate for the wind disturbances. The peak at 0.3Hz is a consequence of the steering inputs from the driver model to compensate for the lateral bridge motion and maintain the desired path. These steering inputs are of lower magnitude, however, applied at a higher frequency. Figure 6.24 illustrates the mean, RMS, and the steering effort (blue curve) required by the driver to maintain a certain steering wheel angle as a function of vehicle speed. It is seen that greater steering effort is required with increase in vehicle speed.

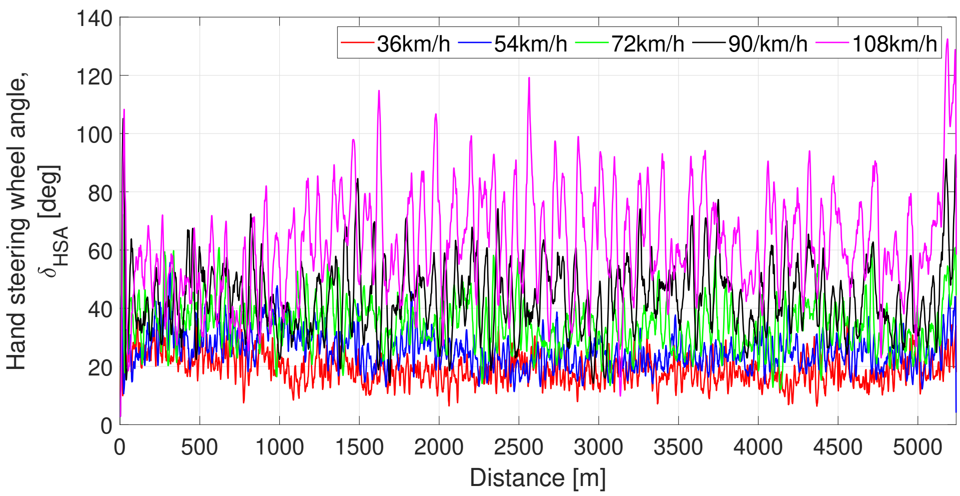

Figure 6.22: *Hand steering wheel angle as a function of distance for a laden vehicle under μ=0.7*

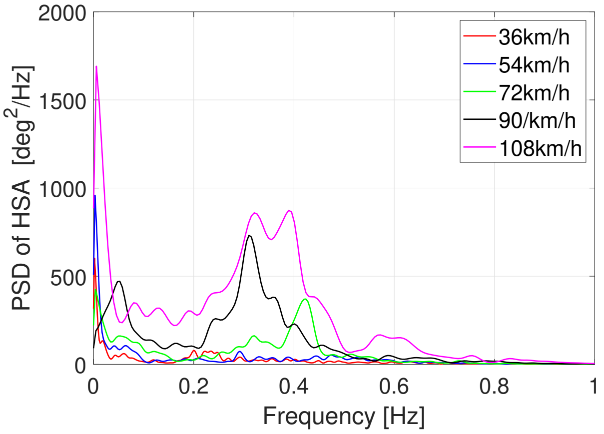

Figure 6.23: *PSD of HSA signals from Fig. 6.18 as function of frequency*

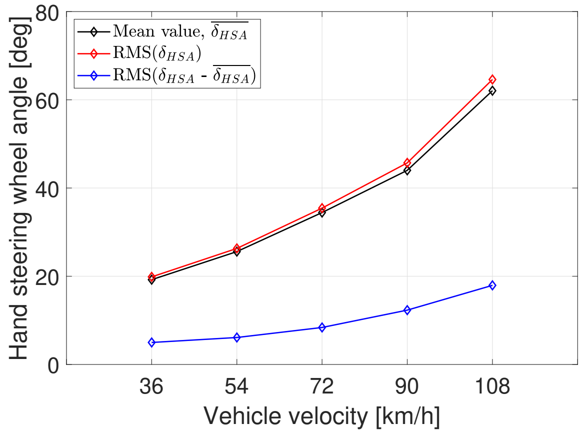

Figure 6.24: *Mean and RMS values of HSA signals from Fig. 6.18*

Figures 6.25 and 6.26 depict the mean and RMS of the steering inputs for the vehicle under different trailer loading and road friction conditions, for different vehicle test speeds. It is observed that the steering effort increases with increasing vehicle test speeds for all test conditions. For a vehicle with similar loading condition, higher effort is required to control the vehicle on a road with friction 0.3 as compared to when the road friction is 0.7. This effect is magnified at higher test speeds. For a vehicle on a road with similar road friction, it is observed that more effort is required to steer the laden vehicle as opposed to the unladen vehicle.

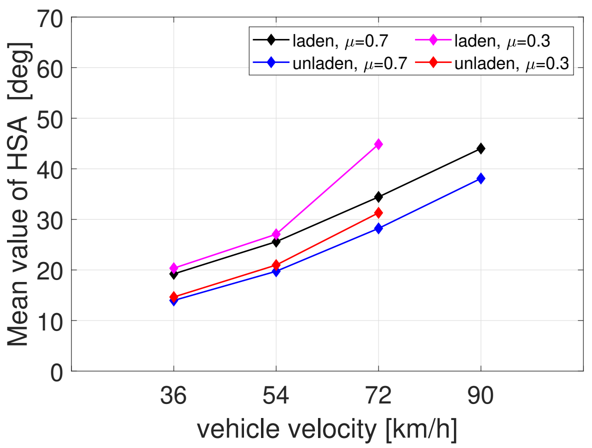

Figure 6.25: *Mean value of HSA signals under different scenarios across vehicle speed*

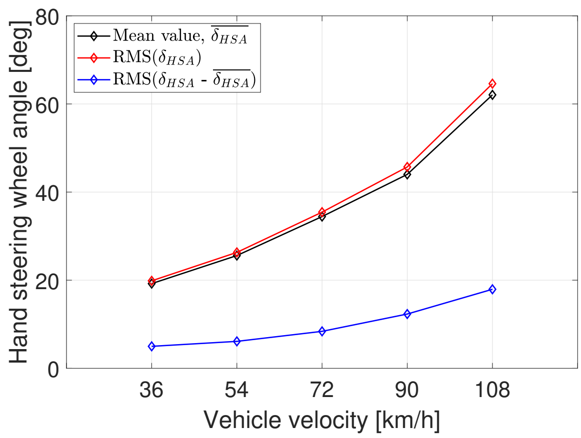

Figure 6.26: *RMS value of HSA signals under different scenarios across vehicle speed*

6.6 Roll-over Risk

The wind excites the vehicle from left side of the vehicle. Therefore, there is a load transfer between the left and right tracks on all the axles. Figures below illustrate the load transfer across the axle 1 (steering axle; figures 6.27 and 6.28), axle 2 (figures 6.29 and 6.30), axle 3 (figures 6.31 and 6.32), axle 4 (figures 6.33 and 6.34) and axle 5 (figures 6.35 and 6.36) for the vehicle speeds of 36km/h and 90km/h, respectively. The load transfer can be observed with higher vertical forces on the right track wheels when compared with the left track wheels. Load transfer is higher at 90km/h vehicle speed as compared to that of 36km/h. The vertical tire forces for all tires at 36km/h is greater than zero. However, for the vehicle speed of 90km/h, it is observed from figure 6.34 that the left outside wheel for axle 4 experiences lift-off.

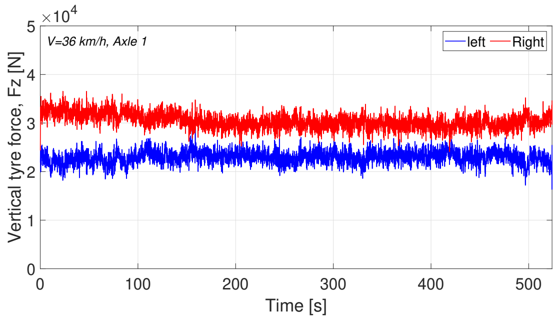

Figure 6.27: *Vertical tyre forces of axle 1 of vehicle at 36km/h under laden condition and* μ*=0.7*

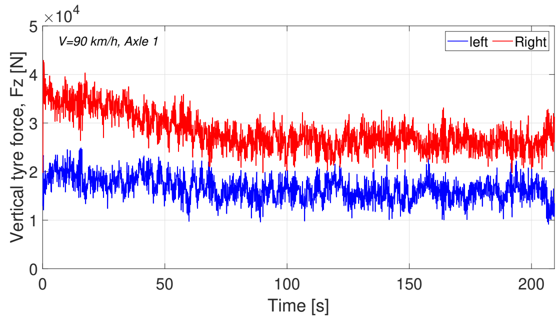

Figure 6.28: *Vertical tyre forces of axle 1 of vehicle at 90km/h under laden condition and* μ*=0.7*

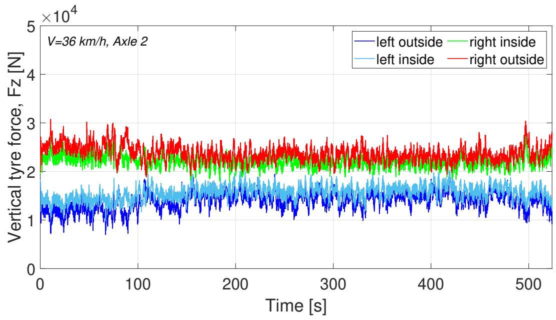

Figure 6.29: *Vertical tyre forces of axle 2 of vehicle at 36km/h under laden condition and* μ*=0.7*

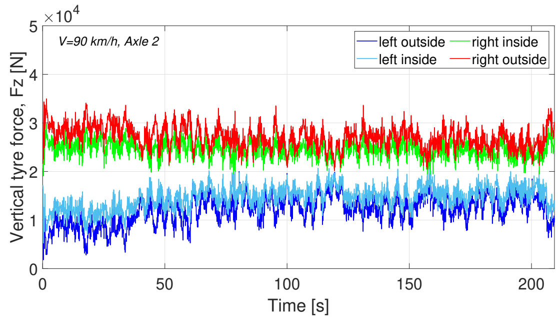

Figure 6.30: *Vertical tyre forces of axle 2 of vehicle at 90km/h under laden condition and* μ*=0.7*

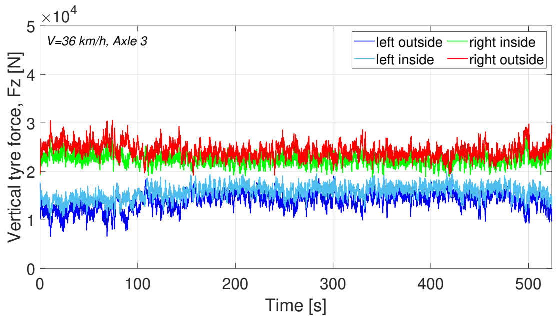

Figure 6.31: *Vertical tyre forces of axle 3 of vehicle at 36km/h under laden condition and* μ*=0.7*

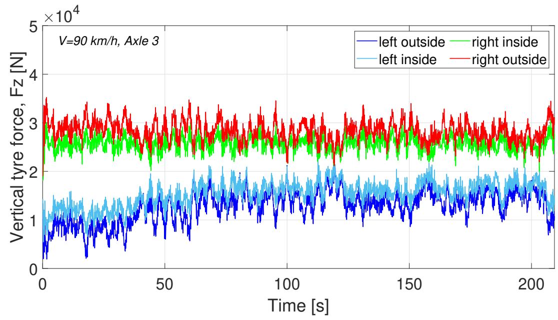

Figure 6.32: *Vertical tyre forces of axle 3 of vehicle at 90km/h under laden condition and* μ*=0.7*

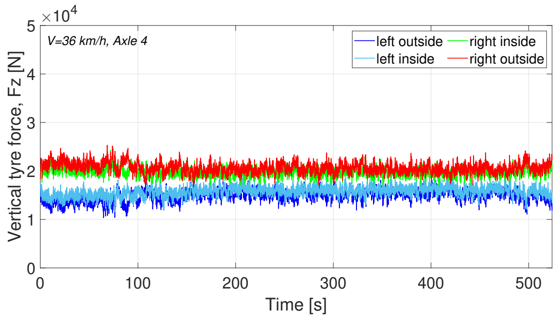

Figure 6.33: *Vertical tyre forces of axle 4 of vehicle at 36km/h under laden condition and* μ*=0.7*

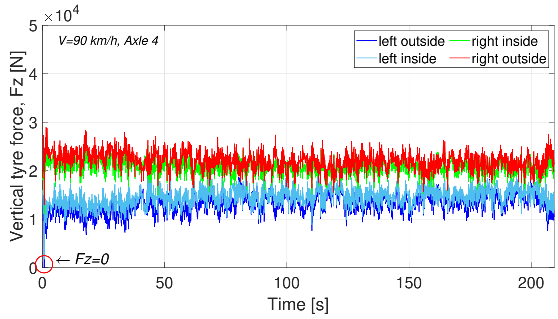

Figure 6.34: *Vertical tyre forces of axle 4 of vehicle at 90km/h under laden condition and* μ*=0.7*

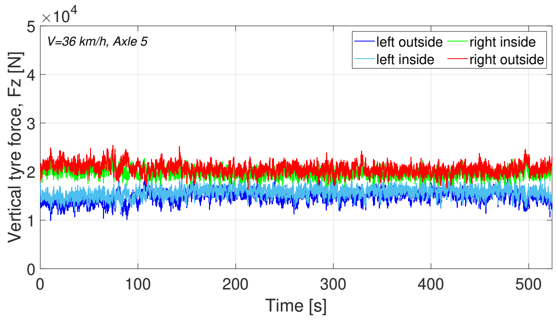

Figure 6.35: *Vertical tyre forces of axle 5 of vehicle at 36km/h under laden condition and μ=0.7*

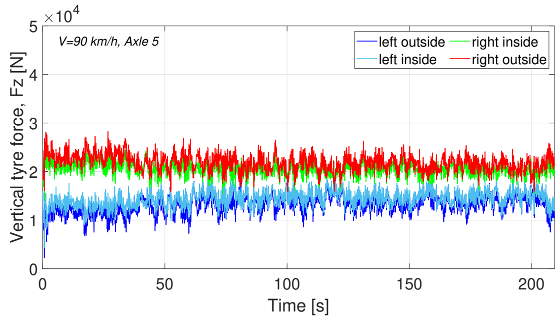

Figure 6.36: *Vertical tyre forces of axle 5 of vehicle at 90km/h under laden condition and μ=0.7*

Wheel lift-off is a close indication of the probability of roll-over. Therefore rollover risk can be determined by calculating the load transfer ratio (LTR) as described through equation 6.1. An LTR of magnitude 1 translates to wheel lift-off and a value greater than 0.9 is considered critical for wheel lift-off.

$$LTR_i = \frac{(F_{zl,i} - F_{zr,i})}{(F_{zl,i} + F_{zr,i})} \tag{6.1}$$

where,

F_{zl} : vertical tire forces on the left track of the axle $[N]$

F_{zr} : vertical tire forces on the right track of the axle $[N]$

i : vehicle axle number (1,2,3,4,5)

Figures 6.37 and 6.38 show the maximum absolute and RMS values of LTR across all axles for vehicle speeds of 36km/h and 90km/h. In correlation to the inference above, it is observed in figure 6.38 that the maximum LTR is approximately 0.9 for axle 4, depicting a very high chance of wheel lift-off. Figures 6.39 and 6.40 illustrate the maximum absolute and RMS of LTR for all axles across all vehicle test speeds for the laden vehicle on a $\mu = 0.7$ road. It can be seen from figure 6.39 that axles 2, 3, 4 and 5 have a high probability of wheel lift-off beyond the vehicle speed of 90km/h. Since the RMS values of LTR are relatively low, it translates to wheel lift-off only on few occasions along the length of the bridge.

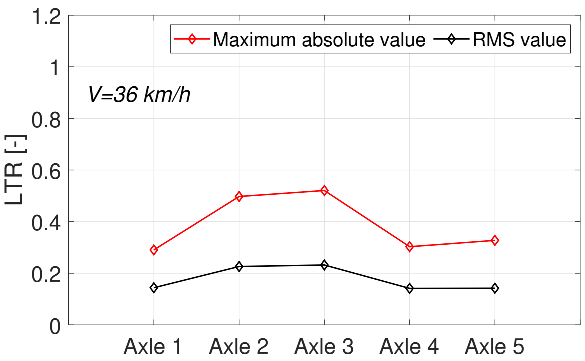

Figure 6.37: *Maximum absolute value and RMS value of LTR across axles for a laden vehicle for μ=0.7*

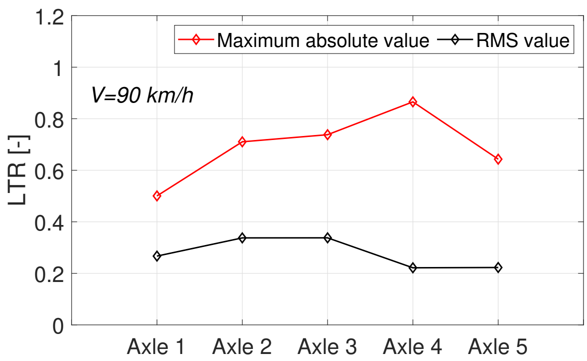

Figure 6.38: *Maximum absolute value and RMS value of LTR across axles for a laden vehicle for μ=0.7*

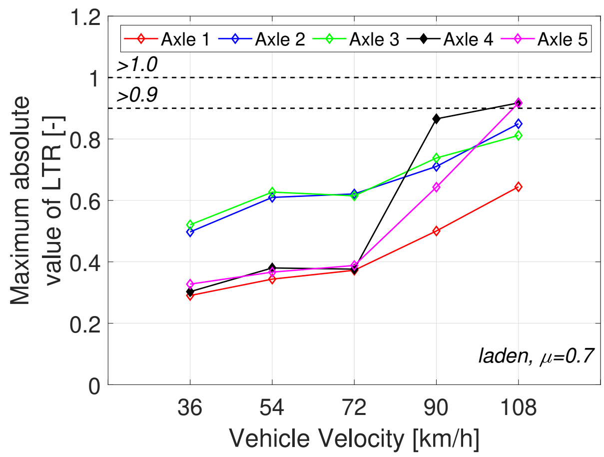

Figure 6.39: *Maximum absolute value of LTR across axles as function of vehicle velocity*

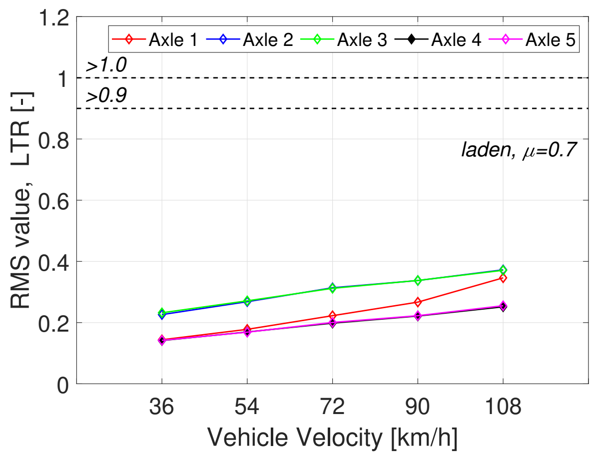

Figure 6.40: *RMS value of LTR across axles as function of vehicle velocity*

The maximum absolute and RMS values of LTR for axle 1 (figures 6.41 and 6.42), axle 2 (figures 6.43 and 6.44), axle 3 (figures 6.45 and 6.46), axle 4 (figures 6.47 and 6.48) and axle 5 (figures 6.49 and 6.50), for different trailer load and road friction test cases, across all vehicle test speeds are illustrated in the respective figures. Figures 6.41 and 6.42 depict low values of LTR implying that axle 1 (steering axle) does not experience wheel lift-off under any test condition. Figures 6.43, 6.44, 6.47 and 6.48, it is noted that the axle 2 and axle 4 of the unladen vehicle experiences wheel lift-off for all vehicle speeds greater than 36km/h. At vehicle speeds of 90km/h, axle 4 of the laden vehicle also experiences wheel lift-off. From figures 6.45, 6.46, 6.49 and 6.50, it is observed that the axle 3 and axle 5 of the unladen vehicle experiences wheel lift-off for all vehicle test speeds. Figures 6.42, 6.44, 6.46, 6.48 and 6.50 illustrate lower RMS values of LTR for $\mu = 0.3$ road at 90km/h, since the vehicle slides off completely under low road friction conditions.

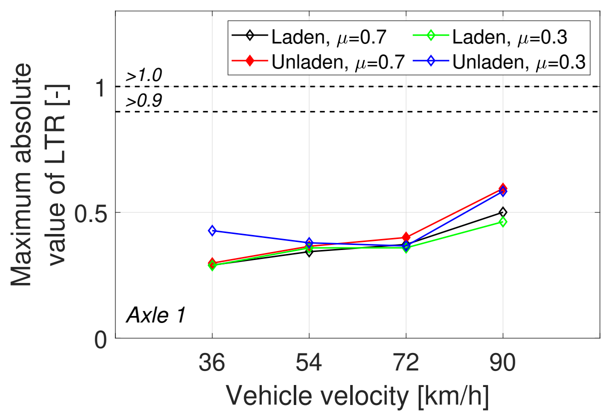

Figure 6.41: *Maximum absolute value of LTR as function of vehicle velocity under different scenarios*

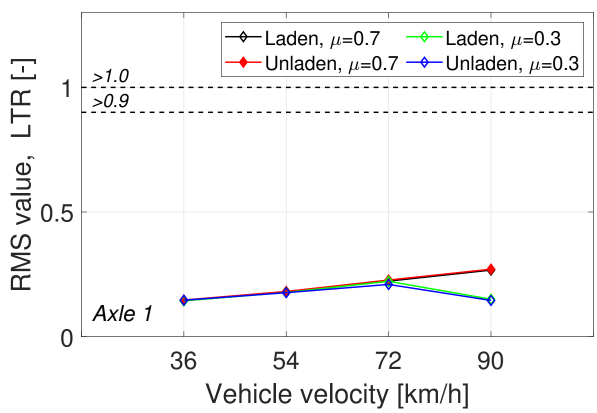

Figure 6.42: *RMS value of LTR function of vehicle velocity under different scenarios*

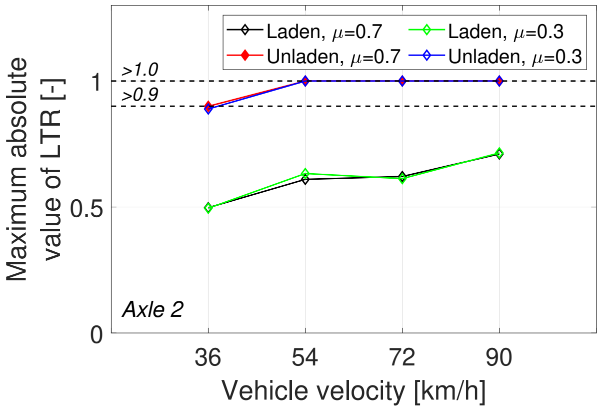

Figure 6.43: *Maximum absolute value of LTR as function of vehicle velocity under different scenarios*

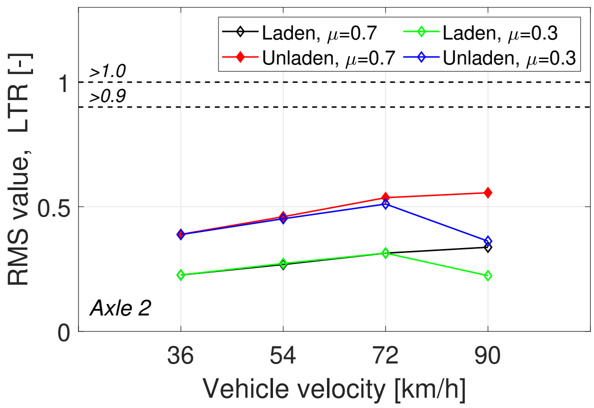

Figure 6.44: *RMS value of LTR as function of vehicle velocity under different scenarios*

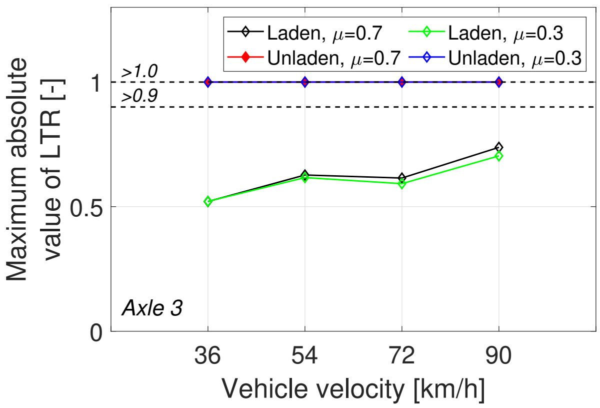

Figure 6.45: *Maximum absolute value of LTR as function of vehicle velocity under different scenarios*

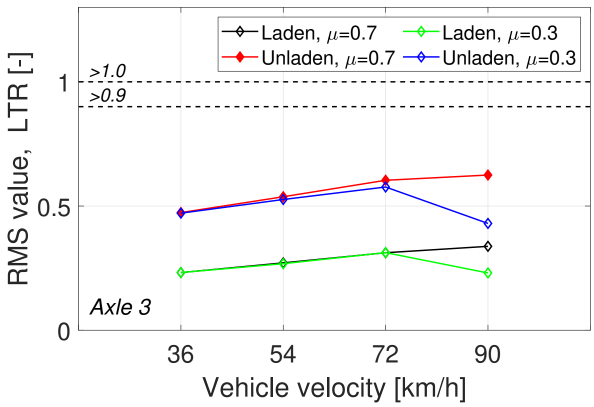

Figure 6.46: *RMS value of LTR as function of vehicle velocity under different scenarios*

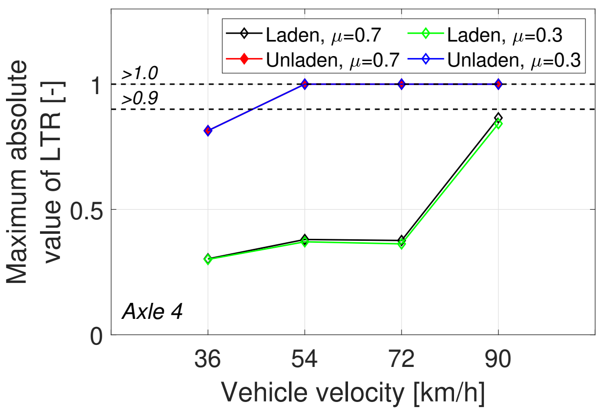

Figure 6.47: *Maximum absolute value of LTR as function of vehicle velocity under different scenarios*

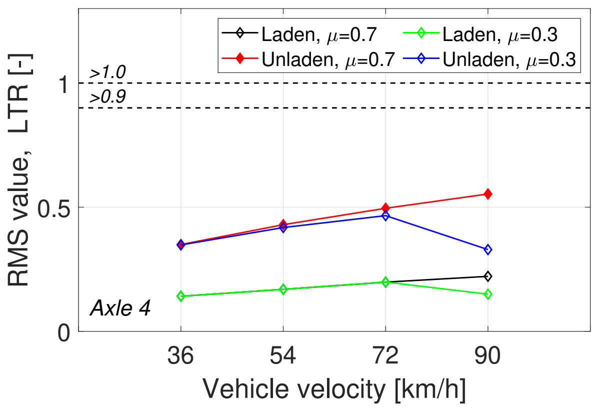

Figure 6.48: *RMS value of LTR as function of vehicle velocity under different scenarios*

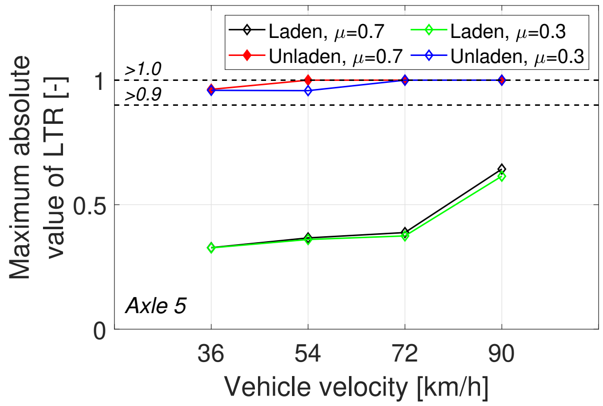

Figure 6.49: *Maximum absolute value of LTR as function of vehicle velocity under different scenarios*

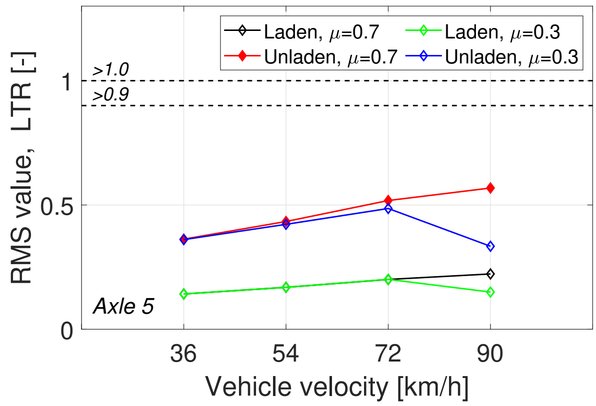

Figure 6.50: *RMS value of LTR as function of vehicle velocity under different scenarios*

6.7 Risk of losing lateral Grip

The Lateral Side-slip Limit (LSL) is based on the criterion that the minimum value of the difference between the maximum allowable lateral friction forces of all wheels and the actual lateral tyre forces should be equal to or greater than zero [20]. The LSL is defined for the every axle in the equation 6.2.

$$LSL_{axle,x} = min\left[\sqrt{\left(F_{xy}\right)^2 - \left((F_x)^2 + (F_y)^2\right)}\right] = min\left[\sqrt{\left(\mu \cdot F_z\right)^2 - \left((F_x)^2 + (F_y)^2\right)}\right] \tag{6.2}$$

where F_{xy} is the maximum available friction forces on the respective axle; F_z is the actual vertical force on the respective axle of the vehicle; F_x is the actual longitudinal tyre force on the respective axle; F_y is the actual lateral tyre force on the respective axle; μ is the road friction coefficient; and x is the axle number from 1 to 5. If the minimum LSL value is under zero for a given axle, that particular axle starts to sideslip and lose lateral grip.

Figure (6.51) illustrates the minimum LSL value for all the individual axles as a function of vehicle velocity. It is noticed that the minimum LSL value decreases with increase in vehicle speed (Figure (6.51)) for a laden vehicle under high road friction. Furthermore, the minimum LSL value is observed to be greater than zero for each case, implying that the LSL limit is not reached for the considered road surface.

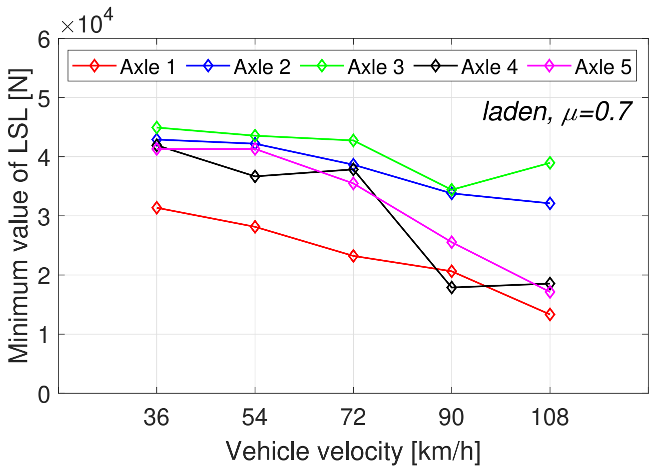

Figure 6.51: *Minimum LSL value as a function of vehicle velocity*

Figures (6.52) to (6.56) illustrate the minimum value of LSL for individual axles as a function of vehicle speeds under different scenarios. The LSL values follow the trend of decreased values with increase in vehicle velocity under all scenarios except for axles 1,2 and 3 at 90 km/h. The LSL values of an unladen vehicle at μ=0.7 for axles 4 and 5 are lower than that of laden vehicle at μ=0.3. Furthermore, the LSL values are lowest in all axles for an unladen vehicle under low friction. Some anomalies between the trend of the curves in some of the graphs could be a result of the complex interactions between the dual wheels on either tracks for all the axles other than the steer axle.

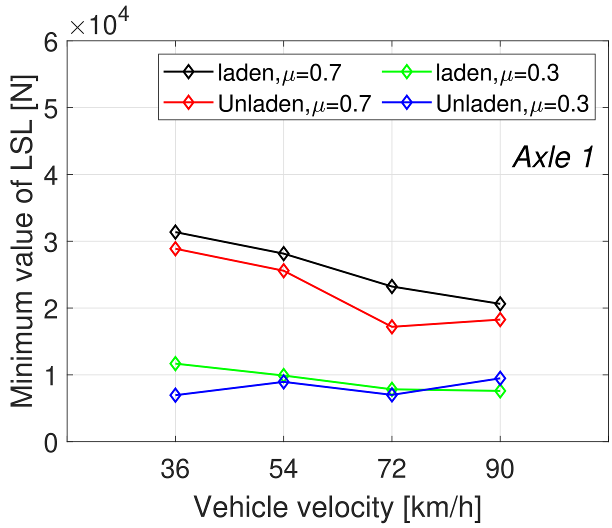

Figure 6.52: *Minimum LSL value as a function of vehicle velocity under different scenarios*

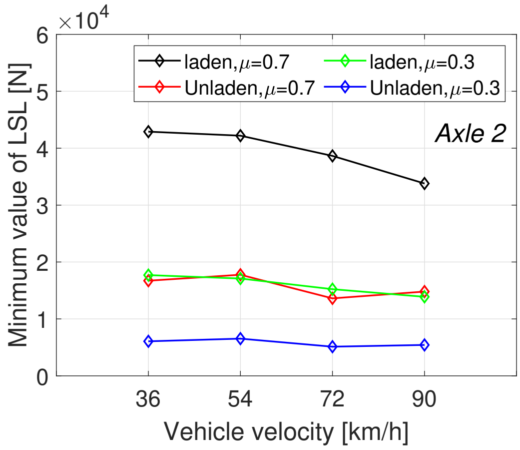

Figure 6.53: *Minimum LSL value as a function of vehicle velocity under different scenarios*

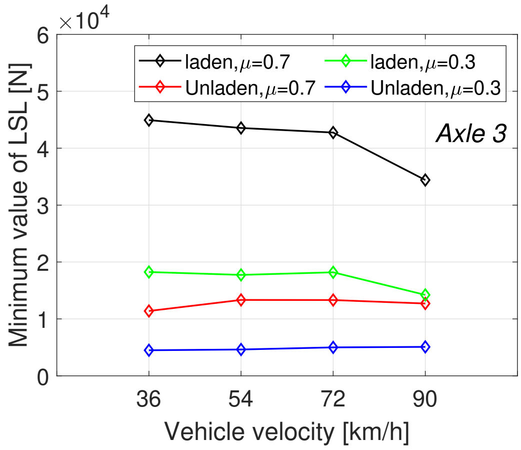

Figure 6.54: *Minimum LSL value as a function of vehicle velocity under different scenarios*

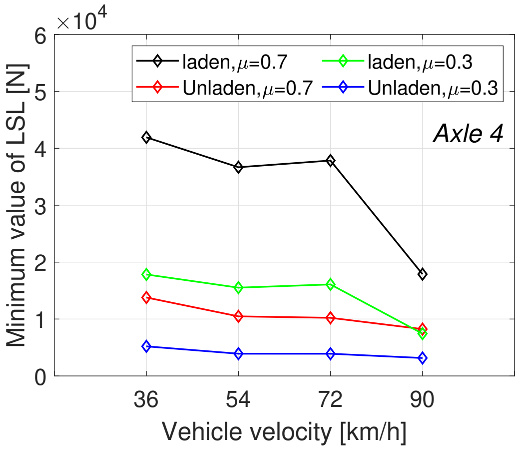

Figure 6.55: *Minimum LSL value as a function of vehicle velocity under different scenarios*

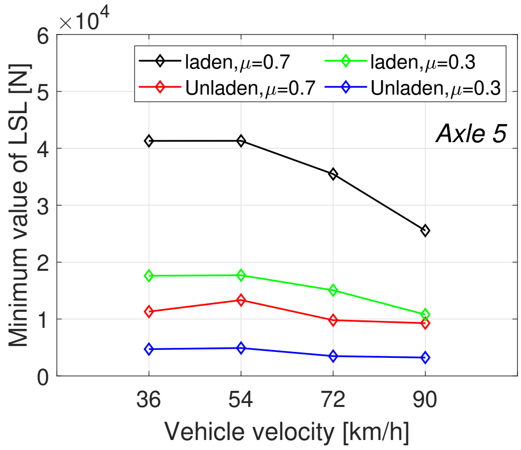

Figure 6.56: *Minimum LSL value as a function of vehicle velocity under different scenarios*

It has been observed in the lateral lane deviation section that the laden and unladen vehicle at 90km/h under low friction of μ=0.3 has completely slid away. The vehicle's lateral displacement trajectory is depicted in the figure 6.57. The rate of lateral displacement is rather high at about 1m/s.

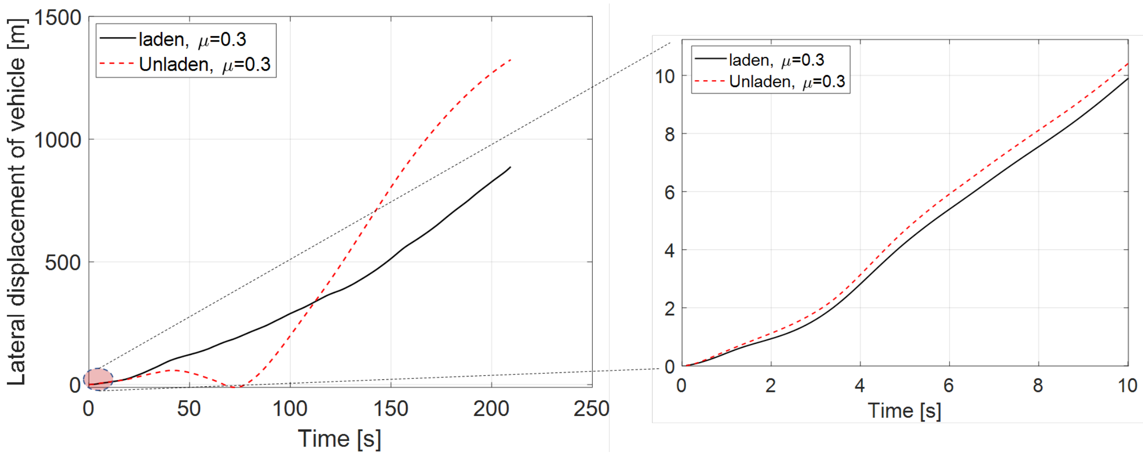

Figure 6.57: *Lateral displacement of vehicle at 90km/h under low friction*

Although the minimum LSL values are logically expected to be zero, this is not reflected in the figures 6.52 to 6.56. The reason is hypothesized as follows. If the tyre has isotropic adhesion properties in the lateral and longitudinal direction, one can assume that the maximum force magnitude F_{xy} is determined by the maximum resultant friction force, $\mu \cdot F_z$ [30].

$$F_{xy}^2 = (F_x)^2 + (F_y)^2 \leq (\mu \cdot F_z)^2 \quad \Rightarrow \quad \left(\frac{F_x}{F_z}\right)^2 + \left(\frac{F_y}{F_z}\right)^2 \leq \mu^2 \tag{6.3}$$

Equation 6.3 can be plotted as a circle, called the "Friction Circle" [30]. Since the lateral and longitudinal properties are not isotropic (due to carcass deflection, tread patterns, camber, etc) the shape may be better described as a "Friction Ellipse" or simply "Friction limit" [30] (Fig. 6.58).

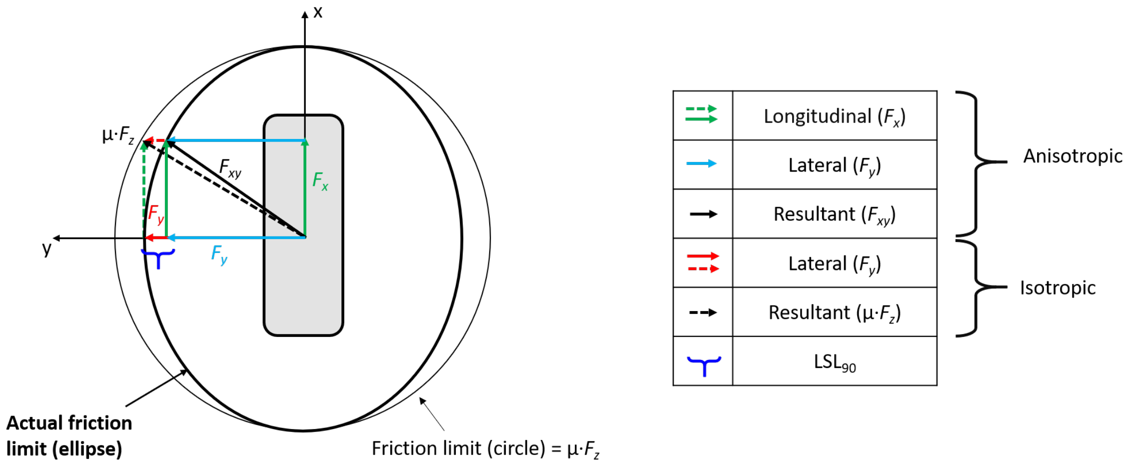

Figure 6.58: *Friction Circle. View from above, forces on tyre*

Whereas the determined friction limit ($\mu \cdot F_z$) in equation 6.3 overestimates the maximum available friction forces of a tyre assuming isotropic property, the actual friction limit is somewhat lower (Fig. 6.58). It is precisely this difference that results in a non-zero value of LSL for the vehicle at 90km/h under low road friction. Thus, while the LSL value is not observed to be zero, considering the anisotropic properties of the tyre to evaluate the lateral side grip should yield a value of zero that explains the axles losing lateral grip.

6.8 Ride comfort

Figure (6.59) depicts the unfiltered vertical acceleration of the tractor CoG for a laden vehicle on μ=0.7 road surface. The acceleration values are greater for higher vehicle speeds. Similar trends are observed in Figures (6.60) and (6.61) that have the lateral acceleration and roll acceleration of the tractor unit respectively.

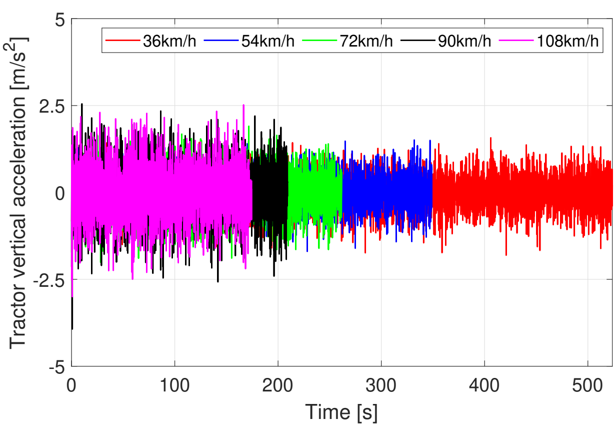

Figure 6.59: *Vertical accelerations of Tractor unit for a laden vehicle under $\mu = 0.7$ across vehicle velocities*

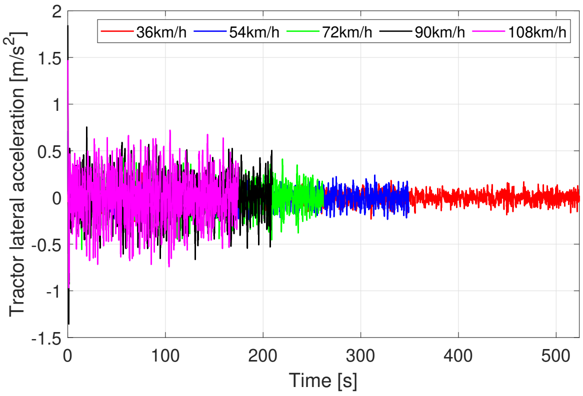

Figure 6.60: *Lateral accelerations of Tractor unit for a laden vehicle under* $\mu = 0.7$ *across vehicle velocities*

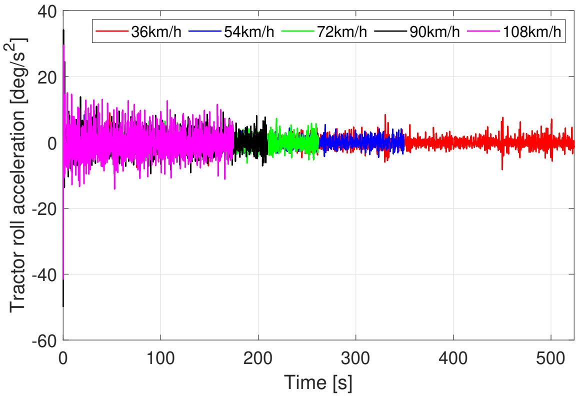

Figure 6.61: *Roll accelerations of Tractor unit for a laden vehicle under* $\mu = 0.7$ *across vehicle velocities*

The international standard ISO 2631/1997 Mechanical vibration and shock - Evaluation of human exposure to whole-body vibration [29] describes the methods to measure, quantify and evaluate the effect of random vibrations on human health, comfort, perception and motion sickness. Standard ISO 2631/1997 defines filters for acceleration signal weighting for human body in a seated position in all three principal axes including measurement of rotational vibration. The tractor acceleration signals indicate higher values with increasing vehicle speed. These results can be used to motivate a detailed study on the ride comfort and motion sickness of the driver in a tractor semitrailer driving on a floating bridge subjected to aerodynamic cross-winds under different scenarios.

7 CONCLUSIONS

In this master thesis, lateral dynamics of a tractor semitrailer traversing a floating bridge subject to environmental loads (1-year storm condition case) was investigated. A method to analyze lateral dynamics of a tractor semitrailer on a moving ground has been developed. The default tractor semi-trailer model available in MSC.ADAMS/Car-Truck with 627 DoF is used for the numerical simulation. This complex high fidelity model has been excited with vertical, lateral and roll motion of the floating bridge. Bridge excitation depend on the location and time of contact between the wheels and the bridge deck. Through the co-simulation, it has been made possible to dynamically compute aerodynamic forces and moments depending on state variables of the vehicle model. The co-simulation has also enabled the pure pursuit controller driver model to be integrated in this analysis. The MSC.ADAMS driver model with an advanced controller was compared with the PPC and used in all the simulation test cases. The main conclusions from this master thesis are as follows:

- The PPC controller and the ADAMS driver model exhibit similarities in the frequency domain for the vehicle speed of 36km/h under laden condition for a road friction of 0.7. The difference in amplitudes between 0.2Hz and 0.4Hz can be ascribed to the advanced controller properties from MSC.ADAMS. The preview time of 0.4s worked well for all the simulation cases other than the case of 108km/h for the laden vehicle at μ=0.7 where the preview time was set to 0.3s to ensure numerical stability.

- The lateral lane deviation of the vehicle varies along the length of the bridge depending on the vehicle speed, wind and bridge motion excitation. The lane deviation is greater with higher vehicle speed. Lane deviation is significant soon after the vehicle enters the bridge at a high speed when the high-velocity cross-wind load starts acting on the vehicle. The vehicle does not violate the lane only for the case of 36 km/h but violates the lane at all other higher speeds. The maximum lane deviation is around 0.7m at 108km/h for the laden vehicle under μ=0.7. The percentage of time lane violation occurs is also higher at higher vehicle speeds.

- Under different scenarios, an unladen vehicle at 36km/h for μ=0.3 is the only distinguished case of lane violation at low vehicle speeds. An unladen vehicle is observed to exhibit greater lane deviation compared to a laden vehicle for all speeds upwards of 54km/h. The unladen vehicle exhibits a greater degree of lane deviation compared to a laden vehicle indicating that it is the most sensitive to path deviation. A maximum lane deviation of around 1.3m is noticed under all scenarios except the case of the vehicle at 90km/h under low road friction. The vehicle under low road friction of 0.3 the vehicle is noted to completely slide off from the designated lane.

- The HSA signals oscillate around a positive mean value as a consequence of the cross-wind component. The mean HSA value is greater for higher vehicle speeds, which could make it difficult for the driver to maintain control of the vehicle. The intensity of the HSA signals are under 0.6 Hz. The highest steering intensities are at vehicle speeds of 108 km/h, with moderately lower frequencies at vehicle speeds of 72 km/h and 90 km/h. The mean HSA value are lower for unladen vehicle compared to that of a laden vehicle. Furthermore, the mean HSA values are greater for a vehicle driving under low friction road surface compared to a high friction road surface.

- Vertical tyre forces of the windward wheels have lower values than those for the leeward wheels that is indicative of lateral load transfer due to aerodynamic crosswind loads. At higher speeds, the variation in the vertical tire forces between the two tracks of the vehicle is noticeable when the tractor semitrailer enters the bridge. Within the first few seconds of the simulation, the windward rear outer wheel of the leading axle in the trailer axle group loses contact, indicating the potential risk of vehicle roll-over for a laden vehicle at 90km/h. This is also confirmed with LTR parameters.

- The RMS values of LTR are noticed to be greater for the tandem drive axle group on the tractor unit than the trailer axle group. The maximum absolute value of LTR however are greater for the trailer axle group indicating the wheel lift-off is initiated in this axle group. The LTR values are greater for higher vehicle velocities. An unladen vehicle under μ=0.7 has the most cases of wheel-lift off compared to its counterparts revealing that it the most sensitive to a potential risk of vehicle roll-over.

- Under different scenarios, the maximum absolute value of LTR illustrates a higher value for higher vehicle velocities on the steer axle. The maximum LTR value is consistently at 1 for the tractor's drive axle group and the trailer axle group of an unladen vehicle for speeds of 54km/h and upwards. The maximum LTR value for all cases of a laden vehicle are below the critical limit of 0.9. The RMS values of every axle under all scenarios demonstrate a consistently increasing value with higher vehicle speeds except the case of an unladen vehicle under low friction at 90km/h where the vehicle slides off the lane completely.

- The LSL values of every axle group display a decreasing value for higher vehicle speeds for a laden vehicle under high road friction. The LSL values for all the axles are greater than zero suggesting that there is no sideslip and thus no loss of lateral grip for the case of laden vehicle considered on the wet/dry road surface with a peak road friction coefficient μ=0.7.

- Under different scenarios, an unladen vehicle under low friction (μ=0.3) has the lowest LSL values on all the axles while the laden vehicle under high friction (μ=0.7) has the highest LSL values. The trailer axle group of an unladen vehicle under μ=0.7 has lower LSL values than a laden vehicle under μ=0.3.

- Tractor acceleration signals in the principal vertical and lateral directions along with the roll acceleration all show greater amplitude of signals for higher vehicle speeds for a laden case under a road friction of μ=0.7. Ride comfort and motion sickness of the driver have not been investigated in this master thesis but these signals serve as a motivation to perform a detailed investigation under all the different scenarios of the test matrix.

- The approach of dynamically computing aerodynamic loads, as a consequence of wind excitations, for individual vehicle units considers the inherent variation due to vehicle articulation. However, these aerodynamic loads are only a good approximation, since the aerodynamic force and moment coefficients considered for this study are only a function of wind yaw angles and not vehicle articulation angles.

- Examining all the results carefully, the safe operational vehicle speeds for a tractor semitrailer on the Bjornafjorden floating bridge subjected to a 1-year storm condition are suggested in the Figure 7.1. These speeds are mainly based on the roll-over risk and lane violation parameters. The concerning values of LTR and lane violation are observed to predominantly occur when the vehicle enters the bridge and exist until the vehicle traverses the descending section of the bridge. Therefore, all orange cells suggest a bridge entry speed of the vehicle limited to 36km/h until the vehicle reaches the lower section of the bridge (around 2km) before proceeding to maintain the vehicle speeds in the orange cell.

Road friction [-]	Laden mass [t]	Vehicle speed [km/h]				
0.7	17	36	54*	72*	90	108
0.7	0	36	54*	72	90	108
0.3	17	36	54*	72*	90	108
0.3	0	36	54	72	90	108

Safe, Caution, Not recommended

Figure 7.1: *Suggested tractor semitrailer speeds from this study*

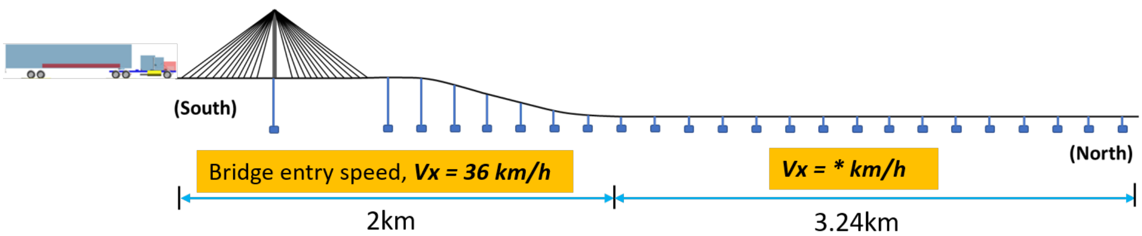

Figure 7.2: *Suggested vehicle velocity profile along the bridge*

8 FUTURE SCOPE

There exists a lot of scope for future work. These are important in discovering deeper insights within vehicle dynamics between the complex interaction of environmental loads and the vehicle itself. Some of the proposed future scope are listed below:

1. The 1-year storm condition (W6 weather) data has been considered in this master thesis. It will be quite interesting to study the lateral dynamics with other storm conditions that are deemed to be severe such as a 10-year storm condition and a 100-year storm condition.

2. The vehicle model considered is the standard tractor semi-trailer model that exists in MSC.ADAMS/Car Truck module. There also exists a higher fidelity tractor semitrailer model with a flexible frame that can capture vehicle dynamics more accurately. It is worth investigating the behaviour with this model.

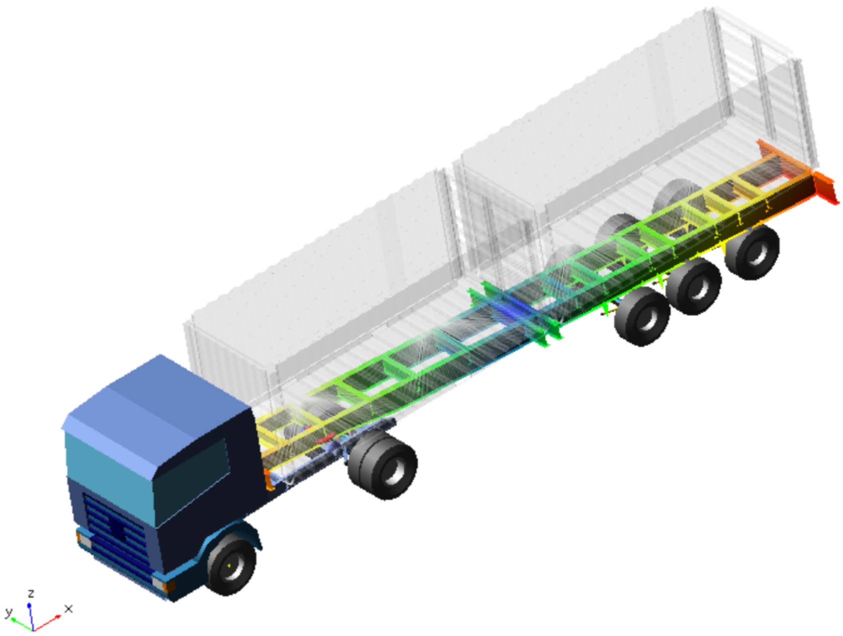

Figure 8.1: *Tractor semitrailer with flexible frame*

3. As the investigations surrounding this master thesis involved a tractor semitrailer as the vehicle of interest, the template builder in MSC.ADAMS is a powerful tool to exploit the construction of long combination vehicles such as an A-double, B-double or a Nordic combination. These long combination vehicles are popular within the Scandinavian region and is therefore naturally appealing to investigate the effect of aerodynamic loads on a moving ground that govern the complex interactions in these long combination vehicles.

4. Having developed a method of co-simulation between MSC.ADAMS and Matlab/Simulink to incorporate the driver model, a more advanced driver model that is intended for such cross-wind applications can be modelled within Simulink to investigate the driver-vehicle responses and behavior. As the road to autonomous driving is around the corner for commercial vehicles, this is an area for future research.

5. The development of the method to investigate complex interactions between the vehicle and environmental loads on a moving ground in MSC.ADAMS is useful for model simplification / complexity reduction. Results from simpler vehicle models designed and developed in MATLAB/Simulink or OpenModelica can be compared with that of the results from the more accurately existing vehicle model within MSC.ADAMS from the co-simulation that can aid the development of model fidelity reduction. It will benefit from shorter simulation time and reasonable accuracy that could be useful for *real-time bridge closing decision* tool, without looping in the MSC.ADAMS software.

6. A study to validate previously performed investigations for a passenger car and an intercity bus in MATLAB/Simulink can be compared with the method developed in this master thesis as MSC.ADAMS is equipped with vehicle models of a car and a bus. This will aid in closing gaps that resulted from model approximations and assumptions, and can support existing results from earlier investigations.

7. The results from numerical investigations in this master thesis can be further refined with a tractor semi-trailer vehicle model to be designed, integrated and driven in the motion platform simulator (CASTER). In particular, the driver model employed from MSC.ADAMS/Car-Truck could be verified for articulated vehicles from driving trials in CASTER. The results from the driving trials may reveal a preview time or look ahead time that could serve as a starting point to tune the P, I, and D gains in the MSC.ADAMS steering controller.

8. With the established methods to incorporate a moving ground, Advanced Driver Assist Systems (ADAS) can be tested and developed. Existing controllers and vehicle functions that aid in vehicle stability control, Roll-over warning, Anti-lock Braking (ABS) Lane departure warning (LDW) and related intervention systems and its function can be further enhanced with the new scenario of the moving ground.

9. Investigation was executed considering aerodynamic force and moment coefficients for tractor and semitrailer as two bespoke units. A comparative study with aerodynamic coefficients for the vehicle as one unit could simplify the process.

10. The effect of articulation angle (θ_c) between the tractor and semitrailer units could be considered while determining the aerodynamic force and moment coefficients. The aerodynamic coefficients then would be a function of both wind yaw angle and vehicle articulation angle ($c(\beta_w, \theta_c)$).

11. The vehicle articulation and roll angles are a direct consequence of the bushing stiffness defined in the ADAMS vehicle model. This needs to be validated with production vehicles to have an accurate roll and articulation behaviour.

Bibliography

[1] Arieh Iserles (2004). *A First Course in the Numerical Analysis of Differential Equations;*, 0-521-55655-4, Cambridge University Press

[2] Abdulwahab, A. , (2018). *Investigations on the Roll Stability of a Semitrailer Vehicle Subjected to Gusty Crosswind Aerodynamic Forces*, PhD Thesis, University of Huddersfield.

[3] Juhlin, M. , (2009). *Assessment of crosswind performance of buses*, PhD Thesis, KTH. (https://www.diva-portal.org/smash/get/diva2:216431/FULLTEXT01.pdf)

[4] Juhlin, M., (2004). *Directional stability of buses under influence of crosswind gusts*, Vehicle System Dynamics.

[5] Juhlin, M., Eriksson, P., (2004). *A Vehicle Parameter Study on Crosswind Sensitivity of Buses*, SAE International.

[6] Juhlin, M., (2009). *Aerodynamic loads on buses due to crosswind gusts – on-road measurements*, Vehicle System Dynamics.

[7] Qiu, J., (2012). *Study of driver models for side wind disturbances*, Master Thesis, KTH.

[8] Zhengqi, G., Guichun, H., (2005). *Research on the Transient State Steering Stability in Side Winds for a High-speed Vehicle Using ADAMS*, SAE International.

[9] Sekulic, Dragan et al, (2021). *Effects of floating bridge motion and wind on bus lateral stability*, Journal of Wind Engineering Industrial Aerodynamics 212 (2021) 104589.

[10] *Washington State Department of Transport.* (https://www.wsp.com/en-US/projects/sr520-evergreen-point-floating-bridge)

[11] *Automotive Handbook, 9th Edition, Robert Bosch GmbH, ISBN 978-1-119-03294-6*

[12] *MSC Software - ADAMS.* https://www.mscsoftware.com/

[13] MSC Software - ADAMS. *Adams Car Truck User's Guide 2021, Adams Car User's guide 2018.*

[14] MSC Software - ADAMS. *Getting Started Using ADAMS/Car.*

[15] MSC Software - ADAMS. *Adams/Solver help - MSC Adams 2010.* ($http://simcompanion.mscsoftware.com/infocenter/index?page = contentid = DOC$9391)

[16] HOU Yu-huai et al, (2009) Dynamic Simulation of Vehicle Floating Bridge System Based on ADAMS. (2009 IEEE DOI 10.1109/ICMTMA.2009.305)

[17] Bhat, A.B. et al. (2020). *Driver Influence on Vehicle Track-Ability on Floating Bridges.* TME180 Automotive Engineering Project, Chalmers University of Technology, Gothenburg, Sweden. (https://odr.chalmers.se/handle/20.500.12380/300748)

[18] Branlard, E. (2010). *Wind energy: Generation of time series from a spectrum.* Technical University of Denmark, Denmark.

[19] Cheli, F., Belforte, P., Melzi, S., Sabbioni, E., Tomasini, G. (2006). *Numerical–experimental approach for evaluating cross-wind aerodynamic effects on heavy vehicles.* Vehicle System Dynamics. 44 (sup1), 791-804.

[20] Chen, F. and Chen, S., (2011). *Reliability-based assessment of vehicle safety in adverse driving conditions.* Transportation research part C: emerging technologies, 19 (1), 156-168.

[21] Chen, S.R., Cai, C.S. (2004). *Accident assessment of vehicles on long-span bridges in windy environments.* J. Wind Eng. Ind. Aerodyn. 92 (12), 991-1024.

[22] Cole, D. J., Cebon, D., (1996). *Truck Suspension Design to Minimise Road Damage.* Proceedings of the Institution of Mechanical Engineers, Part D: Journal of Automobile Engineering. 210 (2), 95-107.

[23] Drugge, L., Juhlin, M. (2010). *Aerodynamic loads on buses due to crosswind gusts: extended analysis.* Vehicle System Dynamics. 48 (S1), 287-297.

[24] Gillespie, T. (1992). *Fundamentals of Vehicle Dynamics*, SAE, Warrendale PA, USA.

[25] Gillespie, T.D., Karamihas, S.M., Cebon, D., Sayers, M.W., Nasim, M.A., Hansen, W., Ehsan, N. (1992). *Effects of heavy vehicle characteristics on pavement response and performance.* Final report. No. UMTRI 92-2, The University of Michigan Transportation Research Institute, Ann Arbor, Michigan.

[26] Gustafsson, A. et al. (2019). *Driver Influence on Vehicle Track-Ability on Floating Bridges.* Bachelor's thesis in Mechanical Engineering, Department of Mechanics and Maritime Sciences, Chalmers University of Technology, Gothenburg, Sweden. (https://odr.chalmers.se/handle/20.500.12380/256914)

[27] Hellsten, O. et al. (2020). *Aerodynamic investigations of a bus under high side wind conditions.* TME180 Automotive Engineering Project, Chalmers University of Technology, Gothenburg, Sweden. (https://odr.chalmers.se/handle/20.500.12380/301635)

[28] ISO 8608, (1995). *Mechanical vibration-road surface profiles-reporting of measured data.* International Standards Organization, Switzerland.

[29] ISO 2631, (1997). *Mechanical vibration and shock - Evaluation of human exposure to whole body vibration.* International Standards Organization, Switzerland.

[30] Jacobson et al, (2020). *Vehicle Dynamics Compendium. Chalmers University of Technology*, ($https://research.chalmers.se/publication/513850/file/513850_Fulltext.pdf$)

[31] Kamnik, R., Boettiger, F., Hunt, K. (2003). *Roll dynamics and lateral load transfer estimation in articulated heavy freight vehicles.* Automobile Engineering Proceedings of the Institution of Mechanical Engineers, Part D: Journal of Automobile Engineering. 217 (11), 985-997.

[32] Liu, P.J., Rakheja, S., Ahmed, A.K.W. (2001). *Dynamic roll instability analysis of heavy vehicles using energy approach.* International Journal of Heavy Vehicle Systems. 8 (2), 177-195.

[33] MathWorks, Inc. (2019). *Signal Processing Toolbox User's Guide*, The MathWorks, U.S.A.

[34] Nguyen, V.M., Le, V.Q. (2019). *Ride comfort performance of heavy truck with three control cases of semi-active isolation systems.* Vibroengineering PROCEDIA. 22, 93–98.

[35] Salati, L., Schito, P., Rocchi, D., Sabbioni, E. (2018). *Aerodynamic Study on a Heavy Truck Passing by a Bridge Pylon under Crosswinds Using CFD.* J. Bridge Eng., 23 (9), 04018065.

[36] Schuetz, T. C. (2015). *Aerodynamics of Road Vehicles, SAE International.*

[37] Sekulic, D. (2018). *Effect of floating bridge vertical motion on vehicle ride comfort and road grip.* ($https://www.vegvesen.no/_attachment/2487039/binary/1294853?fast_title = Effect + of + floating + bridge + vertical + motion + on + vehicle + ride + comfort + and + road + grip.pdf$).

[38] Sekulic, D., et al. (2013). *Analysis of vibration effects on the comfort of intercity bus users by oscillatory model with ten degrees of freedom.* Applied Mathematical Modelling. 37 (18), 8629-8644.

[39] Sekulic, D., Jacobson, B., Moe, S.J., Svangstu, E. (2020).*Effect of Floating Bridge Motion on Vehicle Ride Comfort and Road Grip.* In the IAVSD International Symposium on Dynamics of Vehicles on Roads and Tracks, 1416-1424. Springer, Cham.

[40] Shinozuka, M. (1972). *Digital simulation of random processes and its applications.* J. Sound Vib. 25 (1), 111-128.

[41] Siringoringo, D.M., Fujino, Y. (2012). *Estimating bridge fundamental frequency from vibration response of instrumented passing vehicle: Analytical and experimental study.* Advances in Structural Engineering. 15 (3), 417-434.

[42] Snider, M.J., (2009). *Automatic Steering Methods for Autonomous Automobile Path Tracking.* CMU-RI-TR-09-08.

[43] Vegvesen, (2017). *SBJ-31-C3-MUL-22-RE-100 - Analysis and design (Base Case) Bjørnafjorden, straight floating bridge phase 3 Analysis and design (Base Case).*

[44] Wang, B., Xu, Y., Li, Y. (2016). *Nonlinear Safety Analysis of a Running Road Vehicle under a Sudden Crosswind.* J. Transp. Eng. 142 (2), 04015043.

[45] William, Y. et al. (2014). *Analysis of Vehicle Lateral Dynamics due to Variable Wind Gusts.* SAE Int. J. Commer. Veh. 7 (2), 666-674.

[46] Yu, N. (2007). *Yaw-control enhancement for buses by active front-wheel steering. PhD Thesis, The Pennsylvania State University, (https://www.mne.psu.edu/toboldlygo/Publications/Theses/2007$_Y u_P$hD.pdf).*

[47] Zhang, Q., Su, C., Zhou, Y., Zhang, C., Ding, J., Wang, Y. (2020). *Numerical Investigation on Handling Stability of a Heavy Tractor Semi-Trailer under Crosswind.* Appl. Sci. 10 (11), 3672.

[48] Zhou, Y., Chen, S. (2015). *Fully coupled driving safety analysis of moving traffic on long-span bridges subjected to crosswind.* J. Wind. Eng. Ind. Aerod. 143, 1-18.

[49] *http://promand.com.au/dynamometers.html*

[50] Dunham, K.K.(2016). *Coastal Highway Route E39 – extreme crossings*, Transportation Research Procedia 14 (2016) 494 – 498.

[51] Minoretti, Arianna Bakken, Anja. (2016). *Mega-bridge concepts for Bjørnafjord crossing in Norway*, Conference: Bridges, Coventry

[52] Vika, E.B.(2018) *Modelling and Analysis of a Floating Bridge*, Master's thesis, Norwegian University of Science and Technology

[53] Vegvesen, (https://www.vegvesen.no/siteassets/content/www.vegvesen.no/vegprosjekter/utbygging/ferjefrie39 /vedlegg/faktaark/lonnsomhet-for-godstransport.pdf)

[54] Vegvesen, (https://www.vegvesen.no/siteassets/content/www.vegvesen.no/vegprosjekter/utbygging/ferjefrie39 /vedlegg/faktaark/lonnsomhet-for-personbiler.pdf)

A Simulink model

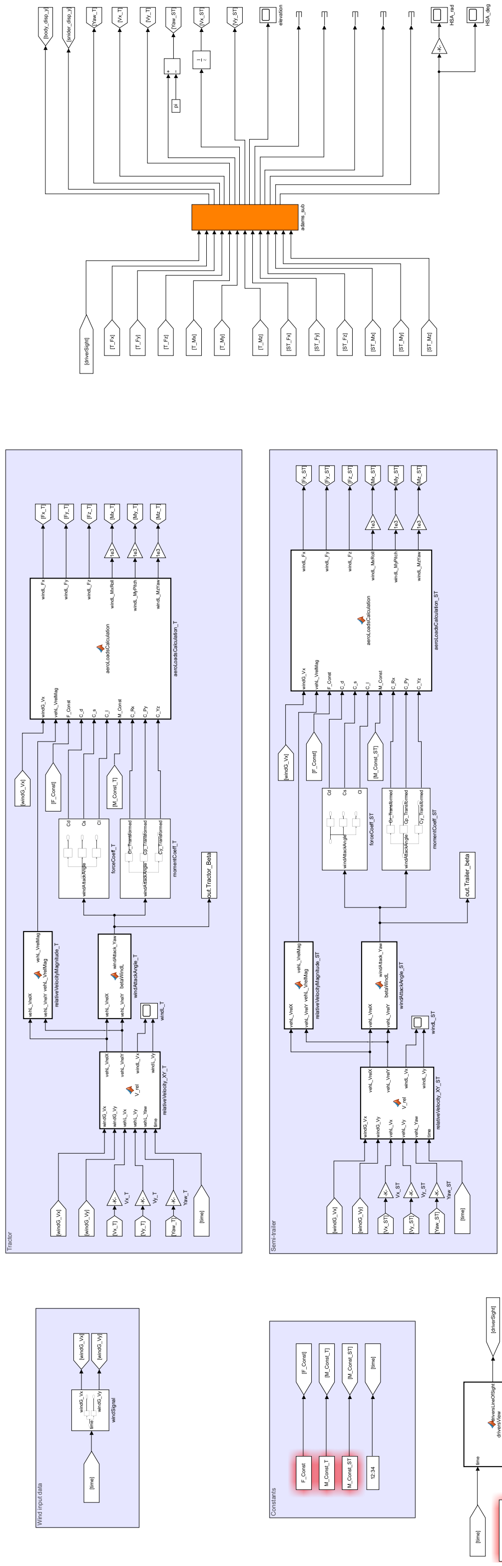

Figure A.1: *Simulink model - ADAMS driver co-simulation*

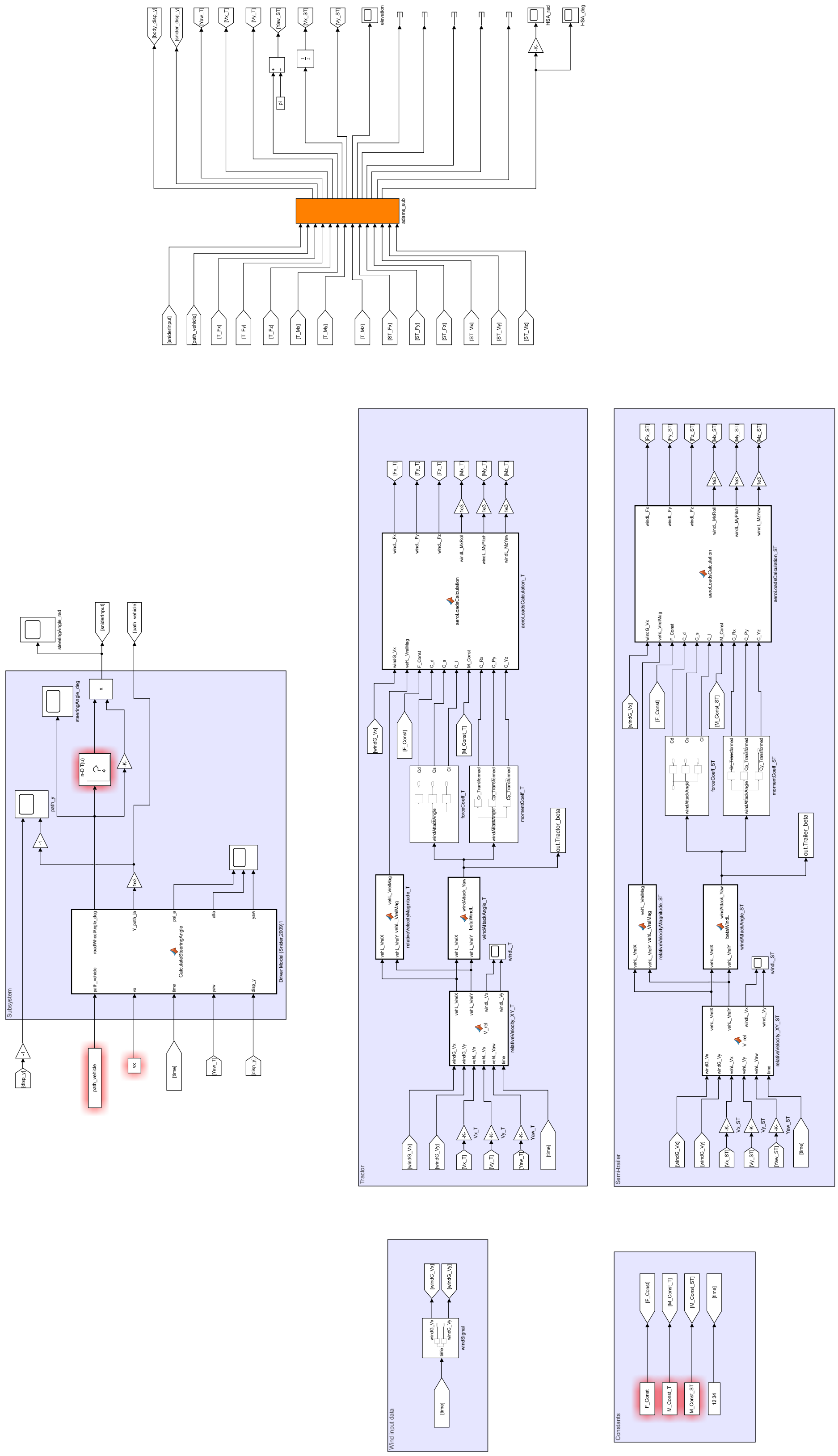

Figure A.2: *Simulink model - Snider driver co-simulation*

B MSC ADAMS: Tractor Semitrailer model parameters

Parameters	Description	Value
ρ	Density of air $[kg/m^3]$	1.29
A	Frontal are of the tractor semitrailer vehicle $[m^2]$	10
L	Wheelbase of the tractor semitrailer vehicle $[m]$	17.48
$L_{Tractor}$	Wheelbase of the tractor unit $[m]$	6.56
$L_{Semitrailer}$	Wheelbase of the semitrailer unit $[m]$	11.73
$CoG_{Tractor}$	CoG position in MSC.ADAMS co-ordinate system $[m]$	(5.11, 0, 1.16)
$CoG_{Semitrailer,Laden}$	CoG position in MSC.ADAMS co-ordinate system $[m]$	(14.34, 0, 1.81)
$CoG_{Semitrailer,Unladen}$	CoG position in MSC.ADAMS co-ordinate system $[m]$	(17.04, 0, 1.72)
$h_{RC,Axle1}$	Roll center height of axle 1 from ground $[m]$	0.676
$h_{RC,Axle3}$	Roll center height of axle 3 from ground $[m]$	0.576
$h_{RC,Axle4}$	Roll center height of axle 4 from ground $[m]$	0.775
$h_{5thWheel}$	Height of the 5th wheel bushing from the ground $[m]$	1.455
$T1$	Longitudinal distance between the tractor CoG and aerodynamic reference point $[m]$	3
$T2$	Height of the tractor CoG from the tractor roll axis $[m]$	0.533
$ST1$	Longitudinal distance between the semitrailer CoG and aerodynamic reference point $[m]$	4
$ST2$	Height of the semitrailer CoG from the semitrailer roll axis $[m]$	0.733

Table B.1: Vehicle Parameters